Silica Nanoboxes As New Nano-Structured Materials: Their Secondary Synthesis From Alumina-Rich Zeolites

Lin Lu

A Thesis
In
The Department
of
Chemistry and Biochemistry

Presented in Partial Fulfillment of the Requirements
for the Degree of Master of Science (Chemistry) at
Concordia University
Montreal, Québec, Canada

December 2005

Your file Votre référence
ISBN: 0-494-14228-6
Our file Notre référence
ISBN: 0-494-14228-6

Abstract

Silica Nanoboxes As New Nano-Structured Materials: Their Secondary Synthesis From Alumina-Rich Zeolites

Lin Lu

Nanomaterials have been widely used in catalysis, separation technology and chemical sensing. In particular, materials with strong surface acidity and high thermal stability are essential in many catalytic applications. However, mesoporous materials reported such as Mobil crystalline (alumino-) silicate MCM-41 and alumino-phosphate based materials lacked such basic properties: this thus limited their applications in petroleum industry. In this work, novel silica nanoboxes H-dealX and deal-CaA with high thermal and chemical stability were developed by secondary synthesis from alumina-rich zeolites. The whole procedure consisted of controlled dealumination of alumina-rich zeolites, ion exchange (optional) and temperature-programmed calcination (TPC) treatments. The optimum conditions for controlled dealumination of alumina-rich zeolites [type 13X (NaX) and 5A (CaA)] using ammonium hexafluorosilicate (AHFS) were determined. It has been found that the richer the silica content in the parent zeolite, the smaller the average pore size produced and the narrower the pore size distribution obtained. The absence of micropores in the dealuminated solids is also a key point for having high thermal stability.

The materials were characterized with regard to their elemental compositions and textural, structural properties, using a variety of methods such as atomic absorption

spectrometry (AAS), X-ray diffraction (XRD), Brunauer Emmet and Teller (BET), and ^{29}Si and ^{27}Al Magic Angle Spinning - Nuclear Magnetic Resonance (MAS NMR). The new silica nanoboxes (m)H-dealX exhibited an inkbottle pore shaped, and the nanometric cavities, being interconnected with each other (BET technique) and showing a periodic arrangement (X-ray powder diffraction at small angles). Their pore opening diameters were determined using nitrogen sorption isotherms (BET technique) and related pore volume data.

In addition, interesting solid superacidic materials were obtained by the deposition of strongly acidic trifluoromethanesulfonic acid (triflic acid, $H_0 = - 14.1$) up to 20wt% onto the silica nanoboxes. Temperature-programmed desorption using a combined system of differential thermal analysis and thermogravimetric analysis (DTA/TGA) allowed the distinction between the bound phases and the liquid phase of the loaded triflic acid.

Acknowledgement

I would like to express my gratitude to my supervisor, Dr. Raymond Le Van Mao for his continual inspiration, encouragement and guidance that lead me to a fulfilling graduate study experience. I am also grateful to Dr. Yves Gélinas and Dr. George Dénès for helpful advice and the time working as my research committee members.

Sincere thanks are also extended to Dr. Ngoc Thanh Vu, Nabil Al-Yassir and Qun Zhao for useful discussion and all unselfish help and assistances throughout my master's research. I would give my special thanks to Dr. Ngoc Thanh Vu for her time in reading this manuscript. I would like to thank all the former and current members in Dr. Le Van Mao's lab for their scientific contributions and friendship.

I would like to thank Rita Umbrassas for supplying me the rotovap equipment so that my project went smoothly without any delay, and Franco Nudo for assistance with the atomic adsorption spectroscopy (AAS).

I also acknowledge the assistance from my fellow graduates, and Carole Coutts, Donna Gordon and Lisa Montesano, Karen Barth in the Department of Chemistry and Biochemistry. Whenever I needed, they were all there to support and help.

I am extremely grateful to my parents for their unconditional loves and supports. They always are there whenever I need help. I would also like to thank my husband and my son for their encouragement and understanding.

Dedicated to my family

Table of contents

List of Figures

List of Tables

List of abbreviations

AAS	Atomic Absorption Spectrometry
AHFS	Ammonium hexafluorosilicate
(b)	bimodal
BET	Brunauer, Emmett and Teller
BJH	Barrer, Joyner and Halenda
CaA	0.80 CaO : 0.20 Na_2O : 1 Al_2O_3 : 2.0 ± 0.1 SiO_2 : x H_2O
D_{av}	Average diameter measured during adsorption
Deal-CaA	Dealuminated zeolite CaA
D^{op}	Pore opening diameter
DRS	Desilication Reinsertion Stabilization
DSS	Sodium salt of 2,2-dimethyl-2-silapentane-5-sulphonic acid
DTA	Differential Thermal Analysis
FCC	Fluid Catalytic Cracking
H_0	Hammet acidity function
ΔH	Enthalpy changes
H-deal X	Hydrogen form of dealuminated zeolite X
(m)	monomodal
MAS	Magic Angle Spinning
MCM-41	Mobile Crystalline Material-41
MTMB	Myristyltrimethyl-ammonium bromide $C_{17}H_{38}BrN$

Na-deal X	Dealuminated zeolite NaX
NaX	1 Na_2O : 1 Al_2O_3 : 2.8 ± 0.2 SiO_2 : x H_2O
NH_4-deal X	Ammonium form of dealuminated zeolite X
NMR	Nuclear Magnetic Resonance
S	Sulfuric acid
S_{BET}	Specific surface area
Scum	Cumulative surface area
TFA(T)	Trifluoromethanesulfonic acid (Triflic Acid)
TGA	Thermogravimetric Analysis
TEOS	Tetraethyl orthosilicate
TPA	Temperature Programmed Calcination
TPAOH	Tetrapropylammonium hydroxide
V_{mac}	Volume of macropores ($cm^3\ g^{-1}$)
V_{mes}	Volume of mesopores ($cm^3\ g^{-1}$)
V_{mic}	Volume of micropores ($cm^3\ g^{-1}$)
V_t	Total pore volume ($cm^3\ g^{-1}$)
XRD	X-Ray Diffraction
ZSM	Zeolite Socony Mobile

List of Appendices

Chapter 1

Introduction

1.1 Literature review on porous solids

Microporous materials with accessible pore openings smaller than 2nm and mesoporous materials with accessible pore openings between 2nm and 50nm (IUPAC nomenclature [1]) are used extensively as heterogeneous catalysts and adsorbents. These materials may have crystalline structure and uniform pore size. When the pores in these materials are of molecular dimensions and allow molecules access to internal surfaces and cavities, these materials can tailor the products of some catalytic reactions based on their size and geometry. This is called shape-selective catalysis.

Typical microporous materials are zeolites, crystalline aluminosilicates, which have been described as small-, medium- or large- (sometimes wide-) pore sized materials, depending on the number of oxygen atoms circumscribing the pores expressed in n-membered ring. Most of the zeolites have pore size below 1nm because 12 or fewer oxygen atoms *i.e.* $n \leq 12$ constitute the pore opening ring. The common zeolites utilized in petroleum industry are ZSM-5 and zeolite Y with pore size of 0.56nm (8-membered ring) and 0.74nm (10-membered ring), respectively. Owing to their different pore sizes, they can be used in catalytic cracking of gasoline (C5-C12) and gas oil (C12-C22), respectively. Ultra-wide pore molecular sieves starts with the discovery of VPI-5, an 18-membered ring alumino-phosphate, by Davis and coworkers in 1988 [2]. However, VPI-5

is unstable towards moist air and steam in the temperature range around 70-100°C; hence it is converted to $AlPO_4$-8. Later, $AlPO_4$-8 was reported to also be an ultra-wide pore material with a one-dimensional 14-membered ring pore system by Dessau et al. [3]. The pores of $AlPO_4$-8 are about 0.7-0.9nm wide, but there is not significantly great accessible pore volume for $AlPO_4$-8. This is because the conversion of VPI-5 to $AlPO_4$-8 leads to faulting in the $AlPO_4$-8 crystals and effective blockage of the one-dimensional pore at pore mouth. Some other ultra-wide pore materials based on alumino-phosphate structure included the following: The iron-aluminophosphate Cacoxenite (a naturally occurring molecular sieve, with a one-dimensional irregular 24-membered ring system) was reported by Szostak et al. [4] in 1990. In addition, Estermann et al. [5] synthesized Cloverite from a fluoride-containing medium. The material is a galliumphosphate containing a three-dimensional pore system consisting of cloverleaf shaped 30-membered ring pores, giving access to 3nm wide cages. JDF-20, an aluminophosphate with a one-dimensional 20-membered ring system was first reported in 1992 by Huo et al. [6]. However, like VPI-5, Cloverite and JDF-20 are also extremely unstable towards moisture. Another type of ultra-wide pore materials is silicate-based structure: the UTD-1 discovered by the group of Balkus [7], another one-dimensional molecular sieve containing 14-membered ring pores. It is the first completely crystalline aluminosilicate with pores larger than 12-membered rings to date. Recently, Wagner and coworkers have reported the discovery of another 14-membered silica based zeolite, CIT-5. This material is also composed of one-dimensional channels and appears to have good thermal stability, retaining crystallinity up to temperature more than 900°C [8].

A major breakthrough to the field of ultra-wide pore molecular sieve research was made by the discovery of a family of materials prepared from surfactant-containing synthesis gels published in 1991 by Mobil researchers [9]. MCM-41 is one of the members of this mesoporous sieves. It is reported that MCM-41 has a regular one-dimensional pore system with pores of originally around 3nm in diameter and its pore size can be tailored from 2nm up to greater than 10nm [10,11]. Some new mesoporous materials that structurally resemble the MCM-41 have been synthesized via different reaction pathways. As the Mobil work started from a cationic surfactant S^+ (Cetyltrimethylammonium, CTMA) and an anionic inorganic species I^- (silicate) through the S^+I^- route, Tanev and coworkers [12] found another important route using S^0I^0 combinations (S^0 and I^0 are primary amines with long alkyl tails and tetraethyl orthosilicate (TEOS), respectively) by virtue of the hydrogen bond interaction between the template and the inorganic species.

These discoveries made it possible to extend the range of zeolite applications towards bulkier molecules in shape-selective catalysis. It opened promising prospects for the refining industry to process heavier crude oil into desired products. For example, Vacuum Gas Oil, a major feed for Fluid Catalytic Cracking (FCC) and Hydrocracking processes, has an average molecule size of about 3.5nm with molecular size distribution shown in Figure 1.1. It can be seen that the heavy resid molecular sizes are within the range of MCM-41 pore diameters and thus easily fit in the pores of the MCM-41. The porous materials with different pore diameters are capable to process different oil products as shown in Figure 1.2.

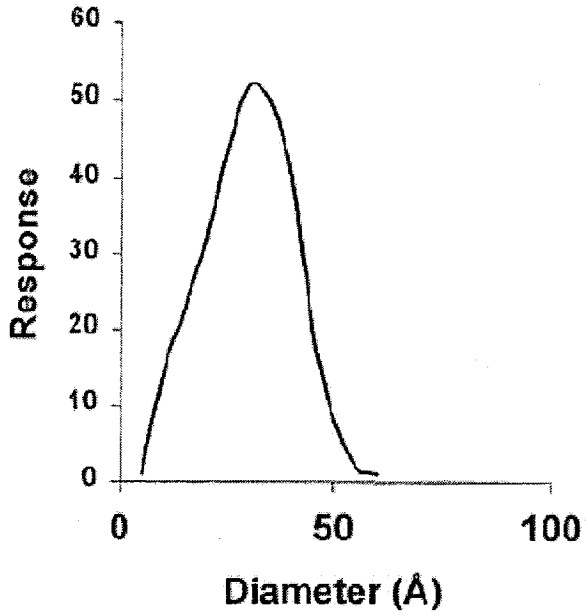

Figure 1.1 Molecular size distributions in typical Vacuum Gas Oil [29d]

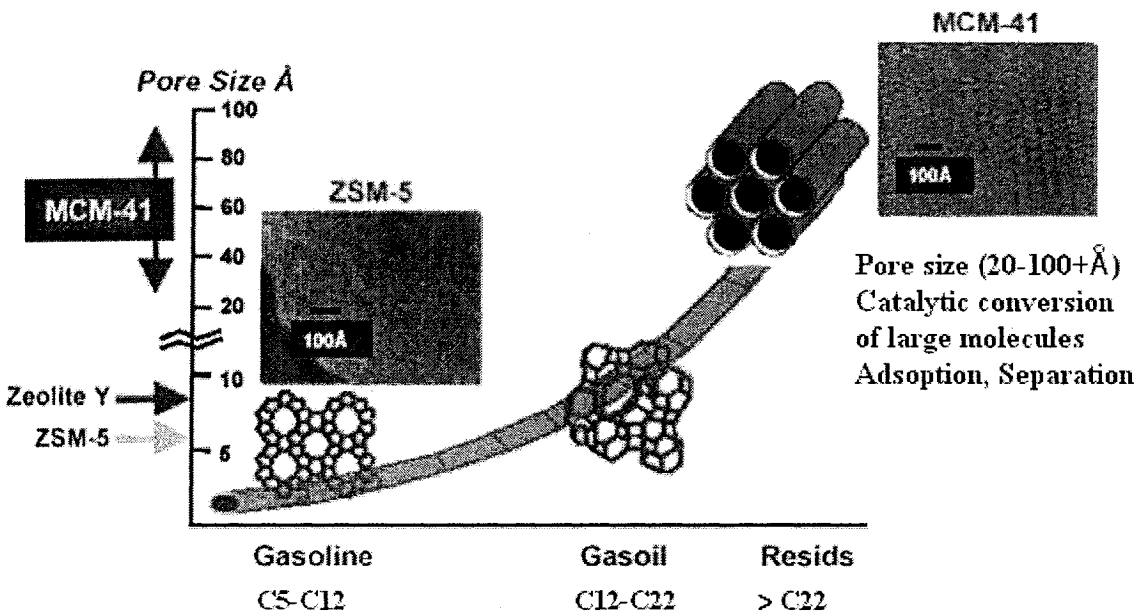

Figure1.2 Profile of pore size of catalyst and associated molecular size processed in the petroleum industry

However, compared to zeolites, several problems were recognized when using MCM-41: low catalytic activity due to low intrinsic acidity, insufficient hydrothermal stability, and slow diffusion and short lifetime due to a one-dimensional system. Among these, low acidity and low hydrothermal stability seriously limit its applications in the field of petrochemical processing [13].

Amorphous porous solids with the pore size larger than MCM-41 such as silica gel and activated charcoal cannot be applied in shape-selective catalysis because of their broader pore size distributions. Figure 1.3 shows the pore size distributions of zeolites, MCM-41, VPI-5, silica gel and activated charcoal. It can be seen that a single pore size exists in the zeolites because of its crystalline structure, and a rather narrow pore size distribution is found in mesoporous MCM-41. On the contrary, amorphous porous solids like silica gel and activated charcoal have relatively broader pore size distributions and pore sizes approximately one to two orders of magnitude larger than those of zeolites. The pores in these materials are generally irregularly spaced and broadly distributed in size. Therefore, shape-selective catalysis cannot be expected to occur in these amorphous solids.

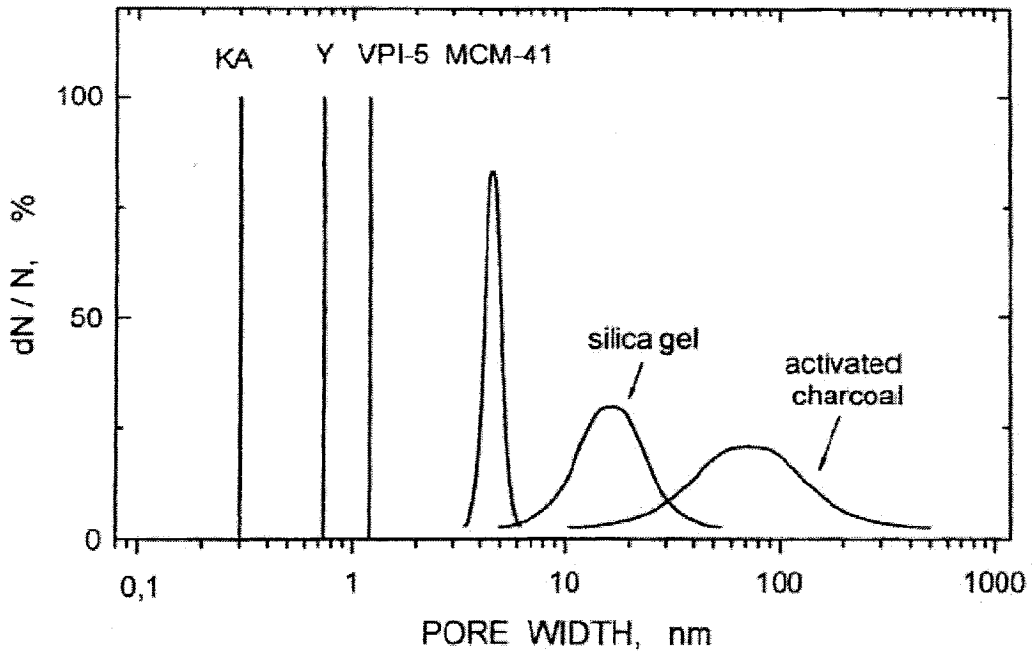

Figure 1.3 Pore width distributions for selected porous solids [14a]

1.2 The objective of this project

Because of the previously mentioned problems encountered in petrochemical industry, it is advantageous to develop new nanostructured materials with the following characteristics:

(a) Large average pore size (pore diameter > 3.5nm) and narrow pore size distribution;

(b) High thermal and chemical stability;

(c) Ordered three-dimensional structure to provide rapid intracrystalline diffusion in the adsorption of reactants / desorption of reaction products, allowing high on-stream stability in some catalytic applications. From Figure 1.4, we can see that these materials will deactivate, - at a given amount of coke (a very complex mixture of various carbonaceous species containing polycyclic aromatics and long-chain, wax-like paraffines) - less rapidly than those having only one - dimensional framework such as MCM-41. Even though a channel in (b) is blocked at one point, the material can still be utilized for a catalytic reaction via the interconnections.

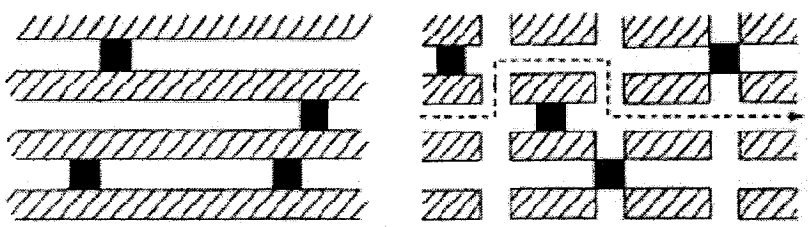

(a) (b)

Figure 1.4 Coke-formation in one-dimensional channel systems (a) and in three-dimensional systems (b) [29a].

In the past, our group has shown that mesoporous materials can be obtained from Al-rich framework zeolites (NaX and CaA zeolites) by a controlled dealumination using ammonium hexafluorosilicate (AHFS) as Al removing agent [15,16,17,18]. This is in contrast with more aggressive Al removing media such as mineral acids that usually lead to severe structural collapses; and thus not very useful mesoporous materials because the latter are subject to numerous pore occlusions [19] or a lack of direct connection with the external surface of the treated zeolite particle [20].

The previous results in our lab [17, 18] indicated however that the pore enlargement using the AHFS method could occur without significant pore occlusion. In addition, A and X type zeolites led to different mesoporous materials: in particular, larger mesopores were obtained with Al-richer zeolites [17, 18]. Based on these, we prepared thermally and chemically resistant nanostructured materials H-dealX and deal-CaA. Characterization and studies on the structure and properties of these mesoporous materials have been performed, which include:

a) Characterizing the nanostructured materials using XRD, AAS, ^{29}Si MAS NMR and ^{27}Al MAS NMR techniques;
b) Identifying the shape of the nanosized cavities in the obtained mesoporous materials and their textural properties;
c) Studying their thermal and hydrothermal stability;
d) Evaluating the possibility of modifying their pore size by using the technique of pore size engineering, which was successfully applied to the ZSM-5 zeolite [21];
e) Investigating their chemical stability by loading strong liquid acids (sulfuric acid) and superacidic species (triflic acid or trifluoromethanesulfonic acid (TFA)).

The thesis presentation includes:

A general review of the literature and patents related to the development of the porous materials is given in Chapter 1. The purpose and the significance of the work are also presented in this chapter. Then in Chapter 2, introduction to some background related to this work is given. Detailed experimental methods/procedures are described in Chapter 3. Chapter 4 reports the results and discussion about the nanostructured materials synthesis and their properties. And finally, the conclusion of this work is presented in Chapter 5.

Chapter 2

Background

2.1 Heterogeneous catalysts

Heterogeneous catalysts are widely used in petroleum or petrochemical industry. Most heterogeneous catalysts are porous solids, which have a total surface area much larger than that corresponding to the external one because of the pore wall. The catalytic activity in heterogeneous catalysts depends upon the structure of a catalyst (the nature and the distribution of atoms or ions in the material, particularly on its surface) and the texture (the geometry of the void space in the catalyst particles). The structure of a heterogeneous catalyst is difficult to elucidate, yet textural properties can be parameterized in terms of measurable quantities by nitrogen adsorption and desorption at 77K. Knowing the nature of the catalysts is helpful to understand the catalytic mechanism in the reaction, as well as to give clues to improve the catalyst in order to obtain the desired results.

2.1.1 Parameters describing the catalyst texture

The specific area is the measurement of the accessible surface area per unit mass of solid (adsorbent); this surface S is the sum of the internal pore surface area and of the external boundary surface area,

$$S = A_m \frac{Na * V_m}{\bar{V}_m} \qquad (1)$$

where S is the specific surface area, Na is the Avogadro constant, $\overline{V}_m$ is the molar volume of the adsorbate, A_m is the part of surface occupied by one molecule of adsorbate in a close layer (in the case of nitrogen, $A_m=16.2*10^{-20}$ m^2), V_m is the monolayer capacity of the unit mass of adsorbent (the volume of adsorbate just sufficient to cover the surface developed by the unit mass of adsorbent) and can be determined by BET method.

Brunauer, Emmett and Teller (BET) proposed a famous model for physical adsorption of gas molecules on a solid surface in 1938 [22] and V_m can be estimated by the BET equation (2), developed assuming that: (a) a multilayer adsorption even at very low pressure; (b) the adsorption on well defined sites; all the sites have the same energy and each of them can only accommodate one adsorbate molecule; (c) adsorption-desorption equilibrium is supposed to be effective between molecules reaching and leaving the solid surface.

$$\frac{x}{V_a(1-x)} = \frac{1}{V_m C} + \frac{C-1}{V_m C}x \qquad (2)$$

where V_a is the adsorbed volume of the adsorbate per unit mass of adsorbent, V_m is the monolayer capacity of the unit mass of solid, x is the relative pressure p/p_o, C is a constant changing with the adsorbent-adsorbate interaction.

It behaves as a straight-line in the form of y = ax + b for x varying from 0.05 to 0.35. Subsequently, V_m and C can be derived from the slope and intercept of the line on the graph.

The specific pore volume refers to the accessible pore void space in the particles per unit mass of solid.

The cumulative specific surface area or pore volume (S_{cum} and V_{cum}) are defined by the sum on k of

$$S_{cum} = \sum S_k \qquad V_{cum} = \sum V_k$$

Where S_k and V_k are the specific surface area and the volume of the pores of radius r_k for the k^{th} interval: $S_k = 2V_k/r_k$. (In order to calculate the distribution of pore area and pore volume as a function of pore size, the isotherm is divided into a suitable number of intervals, each of them corresponding to a small relative pressure range defined by its mean value).

The pore size distribution is the distribution of the pore volume versus the pore size.

The average pore size is obtained by the equation: $r_{average} = 2V_p/S$, where V_p is the pore volume, and S is the total surface area. According to the average size, the pore can be classified into macropores (size > 50nm), or mesopores (2nm < size < 50nm) or micropores (size < 2nm).

According to G. Leofanti et al. [23], the most common **pore shapes** are slits (size is the distance between walls) and cylinders (size is equal to diameter). In addition, pore shapes may be uniform in size, or inkbottle shaped, or funnel shaped. Pore can be closed, blind or through. Each pore can be isolated or connected to other pores to form a porous network as shown in Figure 2.1.

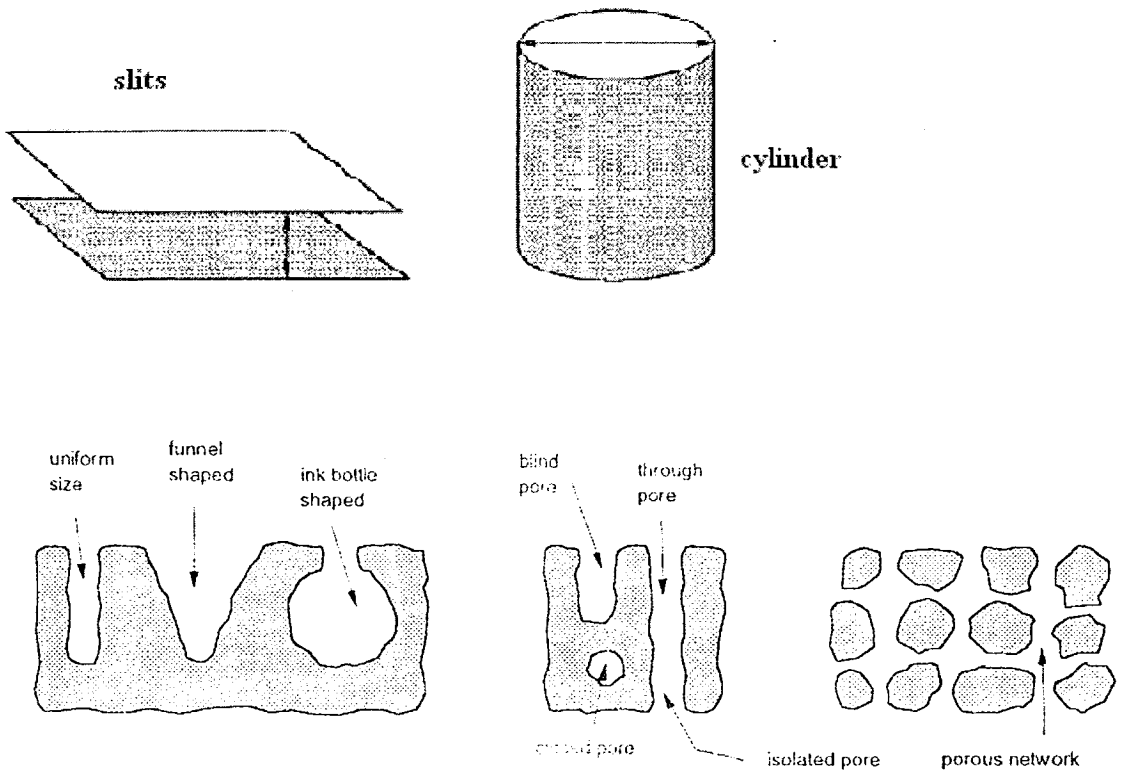

Figure 2.1 Types of pores [23]

2.1.2 Determination of the porous texture of solids

2.1.2.1 Adsorption isotherms

The adsorption isotherm is recorded by nitrogen-adsorbed volume against its relative pressure and its shape depends on the solid porous texture.

In 1940, Brunauer et al. [24] proposed to classify the physical adsorption isotherms into five different groups. Only, four types are often encountered, and are schematically represented in Figure 2.2. Isotherms of type II, IV, I and VI are obtained for macropore (D_{av}>50nm), mesoporous (2nm<D_{av}<50nm), micropore (0.7nm<D_{av}<2nm) and ultramicropore (D_{av}< 0.7nm) adsorbents, respectively.

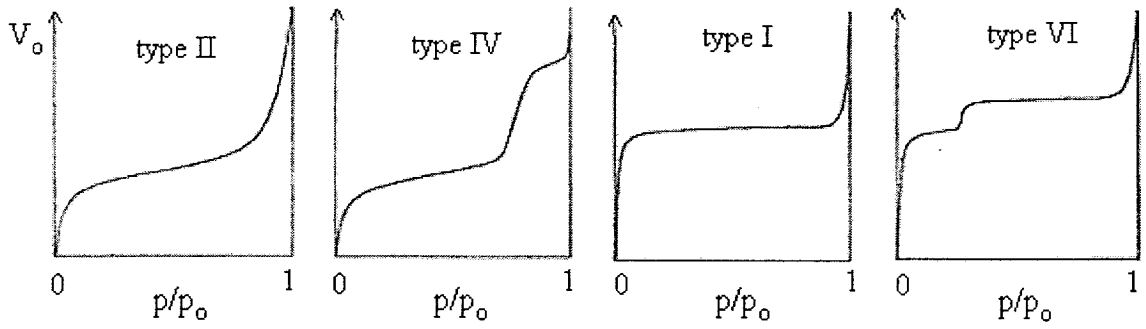

Figure 2.2 Adsorption isotherm found by nitrogen adsorption [24]

Isotherms of type IV are obtained for mesoporous adsorbents. The adsorption isotherm consists of a monolayer of adsorbed molecules at low relative pressure and a multilayer adsorption at high relative pressure, the adsorbate thickness gradually increases until capillary condensation pressure has been reached and the amount of adsorbate rapidly increases. Capillary condensation in pores has a core (*i.e.* the empty space of pores) size r defined by Kelvin equation [25, 26]

$$\ln(p/p_o)=-(2\gamma w_m \cos\theta)/(RTr)$$

where p/p_o is the relative pressure, r represents the radius for cylindrical pores or the distance between walls for slit shaped pores, γ is the surface tension , w_m is molecular volume, θ is contact angle, R is Boltzmann's constant and T is the temperature. As mesopores are filled adsorption continues on the low external surface.

Macroporous solids are of isotherms of type II. It is very similar with mesoporous adsorbents except that capillary condensation takes place at quite high pressure because of large pore diameter in macroporous solids according to Kelvin equation.

Isotherms of type I are characteristic of microporous adsorbents. The adsorption takes place at very low relative pressures because of strong interaction between pore walls and adsorbates. The completion of filling requires a bit higher pressure favored by interaction between adsorbed molecules. In this case pore filling takes place without capillary condensation. Once micropores are filled, the adsorption continues on the external surface.

Isotherms of type VI are characteristic of ultramicroporous adsorbents; hence, it is excluded from the discussion because this project only focuses on mesoporous and microporous materials.

2.1.2.2 Hysteresis loops

A hysteresis loop results from the fact that evaporation (desorption) usually takes place at a lower pressure than that of capillary condensation (adsorption) from mesoporous. This is usually attributed to different size of pore mouth and pore body in the case of inkbottle shaped pores or to a different behavior in adsorption and desorption in near cylindrical through pores. In inkbottle pores the condensation takes place in each section at the relative pressure provided by Kelvin law (the liquid formed at low pressure in the pore mouth supplies the vapor for adsorption and condensation in the large pore body), but the evaporation from the pore body cannot occur until the pore mouth remains filled. In the case of cylindrical pores the meniscus is cylindrical during condensation and hemispherical during evaporation. De Boer has proposed five types of the hysteresis loop in Figure 2.3 and associated pore shape [27a].

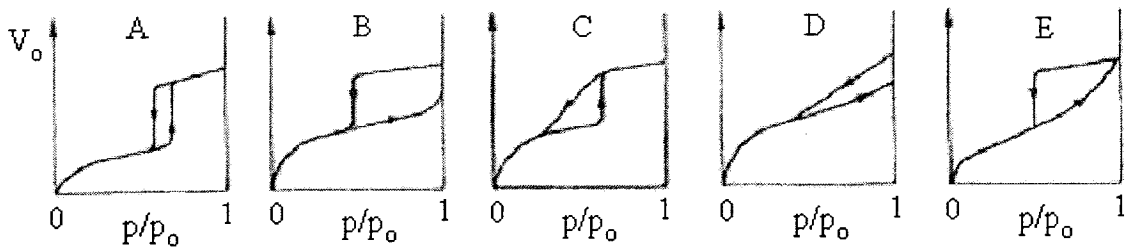

Figure 2.3 The five types of mesoporous hysteresis loops [27a]

In Figure 2.3, hysteresis loop type A and B are associated with "cylinder shaped" pores with rather constant cross section and with slit-shaped pores, respectively. Hysteresis type C and D derive from type A and B respectively and they indicate the cone-shaped pores (type C) and pores formed by non-parallel plate (type D). These two types of hysteresis loops are rather usual. Type E hysteresis very frequently occurs. It corresponds to "ink-bottle" pores, spheroidal cavities or voids between closed-packed spherical-like particles.

The absence of hysteresis loop may indicate either that the solid is microporous or that the pores are nearly perfect cylinders closed at one end, or that the solid is non porous.

On the basis of the isotherm shape and the analysis of the shape and the width of the hysteresis loop (in general, the broader the pore size distribution, the wider the hysteresis loop), we can indeed get the main outlines of the textural characteristics of a solid. For example, if the pores have type IV adsorption isotherm and a hysteresis loop of type E in nitrogen adsorption and desorption, the pore shape can be considered as 'ink bottle' or spheroidal cavities [25, 27a].

2.1.2.3 S_{cum} and S_{BET}

Comparing cumulative surface area, S_{cum}, and specific surface area, S_{BET}, one can obtain more information of the pore texture. If S_{cum} is equal to S_{BET}, the pores will be perfectly cylindrical shape. If S_{cum} is roughly equal to S_{BET} (Scum $\approx S_{BET}$), the pores will have a polygonal cross section. However, a larger S_{cum} ($S_{cum} > S_{BET}$) indicates that there is a certain amount of capillary space without a corresponding surface area, that is to say the assembly of pores intersects each other, *i.e.,* the pores are interconnected [27a].

2.2 Introduction to zeolite science

The term zeolite is derived from the Greek words "zeo" meaning "to boil" and "lithos" meaning "stone". Zeolites are porous crystalline aluminosilicates having a uniform pore structure and exhibiting ion-exchange behavior. Chemically, they are represented by the empirical formula: $M_{2/n}O \bullet Al_2O_3 \bullet ySiO_2 \bullet wH_2O$. Where y is 2 to 10, M is group 1 and group 2 elements, n is the cation valence, and w represents the water contained in the voids of the zeolite. Structurally, zeolites are composed of AlO_4 and SiO_4 tetrahedra linked to each other by the sharing of oxygen ions. Each AlO_4 tetrahedron in the framework bears a net negative charge, which is balanced by an extra-framework cation. The framework structure contains channels or interconnected voids that are occupied by the cations and water molecules. The cations are mobile and ordinarily undergo ion exchange. The water may be removed reversibly by the application of heat. There are two types of structure: one provides an internal pore system comprised of interconnected cage-like voids; the second provides a system of uniform channels, which, in some cases, are one-dimensional channel systems. The usually preferred type is the one that has two- or three-dimensional channels to provide rapid intracrystalline diffusion in the adsorption and applications. In addition, as mentioned previously, such structural differences influence the effective lifetime of zeolitic catalysts.

2.2.1 The pore size and dimensionality

It has been reported that there are approximately 133 different microporous structures registered in the International Zeolite Commission (IZC) for structure codes

[28]. Each microporous material is assigned a three-letter code by the IZC. These microporous materials are distinguished by their size and dimensionality of the pores.

The pore size is determined by the number of oxygen atoms (the number of tetrahedral atom) required to circumscribing the channels or cavities, *e.g.* a pore surrounded by n-oxygen-atoms is referred to as n member-ring pore, n-MR. In the case of cages, n-MR means the pore opening (windows diameter) through which other molecules can access the large cavities of zeolites. The diameter of the channels and cavities varies according to the structure from 0.3 to 1.2nm depending on the number of the oxygen atoms as depicted in Figure 2.4.

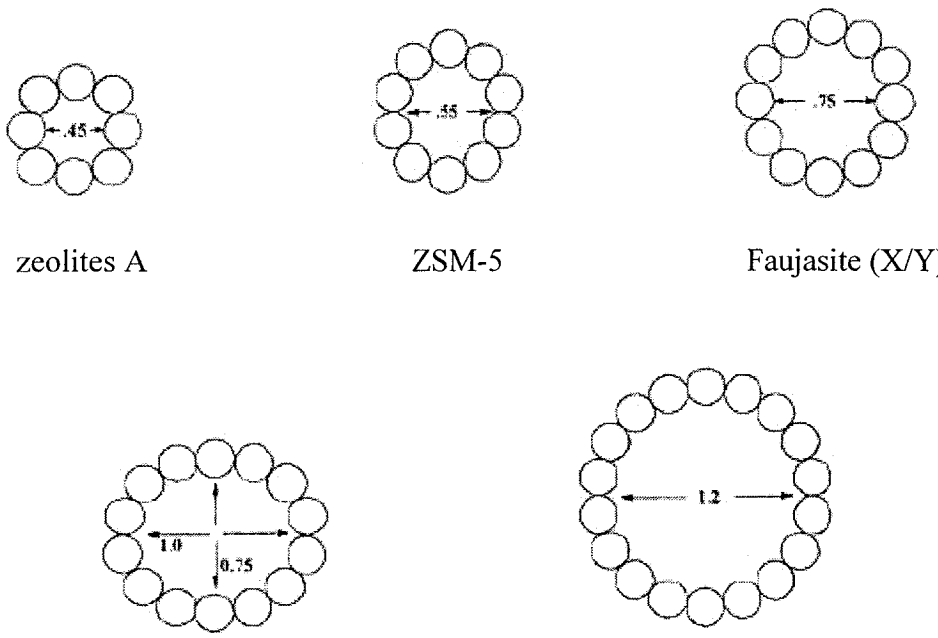

Figure 2.4 Rings of oxygen atoms as present in zeolites A, ZSM-5, Faujasite (X/Y), UTD-1 and the super large pore aluminophosphate VPI-5; diameters in nm [29a].

The dimensionality of the pore system is considered as the zeolite network, *i.e.* it can be regarded as the degree of interconnections between the pores within the structure.

For example, a 1-dimensional (1D) pore system contains pores that do not interconnect with each other, a 2-dimensional (2D) pore system involves interconnection of pores in two directions and allows the molecular diffusion in two ways, and a three-dimensionally connected (3D) pore system contains interconnections of the pores in three dimensions and thus allow molecules to travel through the material in three ways. The pore size and dimensionality in some common zeolites are described in Figure 2.5.

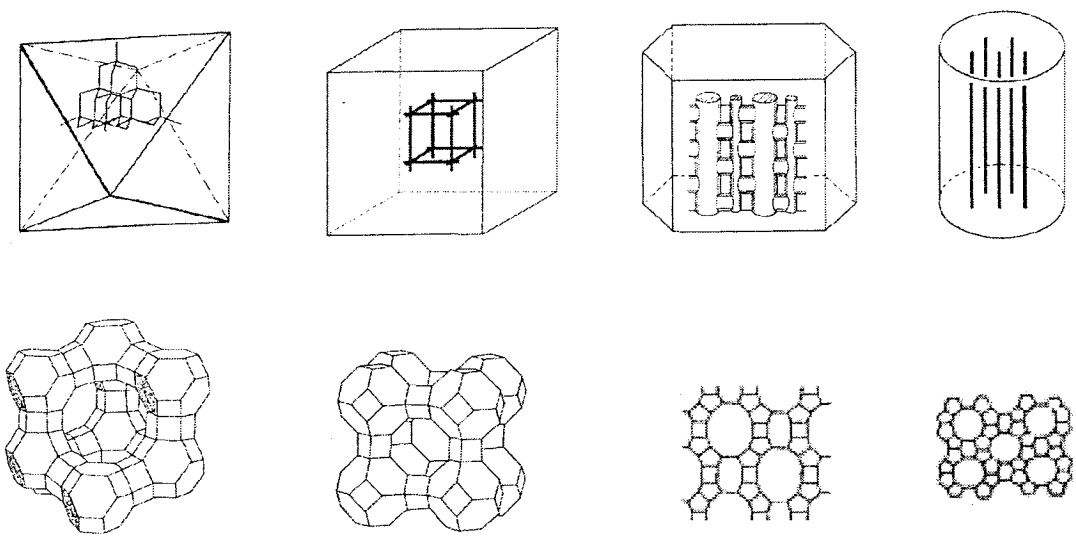

Figure 2.5 Pore size and dimensionality in zeolites [29b]

(a) A three-dimensional pore system (type X or Y zeolites)
(b) A three-dimensional pore system (type A zeolite)
(c) A two-dimensional pore system (Mordenite)
(d) A one-dimensional pore system in which the pores do not interconnect with each other (Type L zeolite)

2.2.2 Ion exchange

It is well known that each AlO_4 in the zeolitic structure requires an extra-framework charge-balancing cation to maintain electroneutrality. The positive cations in some cases can be ion-exchanged to industrial useful cations such as protons, transition metals and lanthanides. In principle, any type of homogeneously cation-catalyzed reaction can be catalyzed by a zeolite carrying this cation.

Ion exchange from aqueous solution allows the introduction of many types of cations into the zeolites. However, unlike most cations, the Brönsted acidic form of the zeolites cannot be directly ion exchanged with acid. Instead, it can be ion exchanged with NH_4-salts and subsequently calcined to produce the acid site as shown in Figure 2.5b. This is because the alumina-rich zeolite such as zeolite A (LTA) will lose significant crystal structure and lead to a structural collapse in acidic solution. The structural framework of silica-rich zeolite will also significantly change in acidic solution, although it is not as severe as in the case of zeolite A, according to Barrer and Makki [30]. They proposed that the structural change occurred in two steps; first step was the replacement of the metal cation with H_3O^+ followed by $[Al^{+3} + H_3O^+]$ removal leaving what they referred to as a hydroxyl nest.

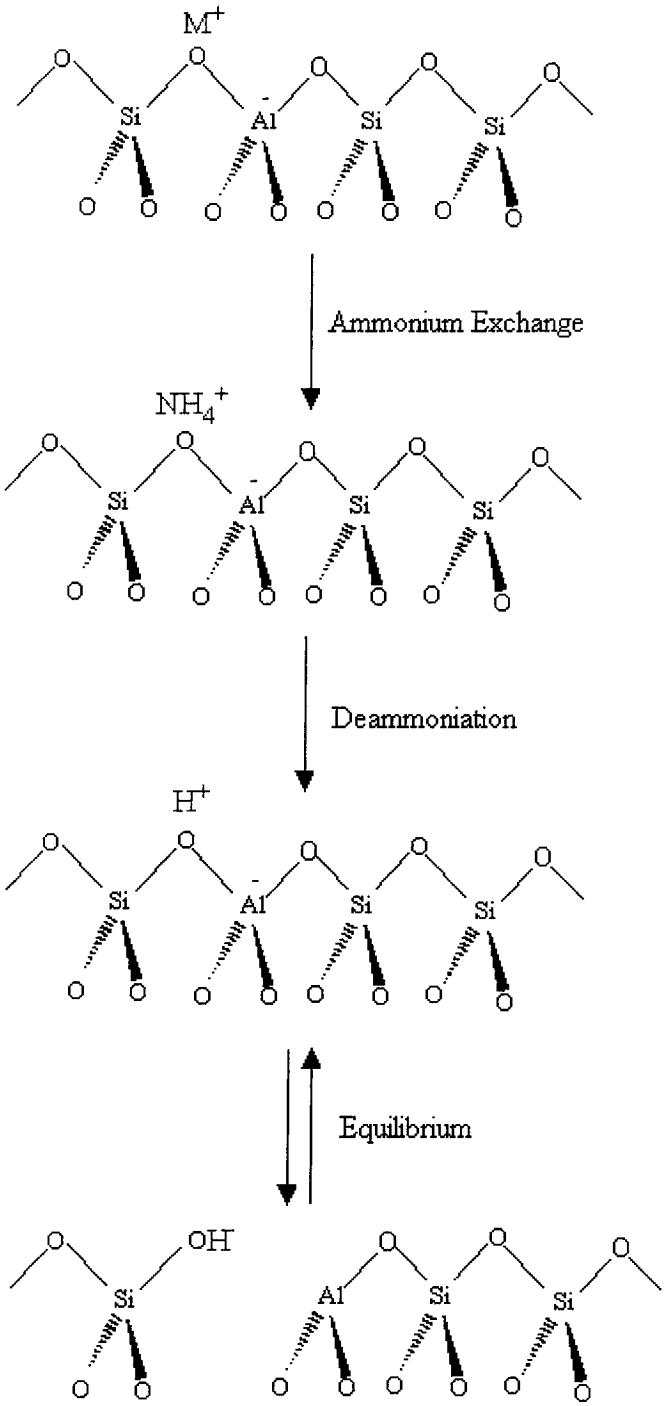

Figure 2.5b Ion exchange and acid site formation in zeolite-like materials

Ion-exchange capacity is mostly dependent on the ratio of Si/Al. The higher aluminum content in zeolites, the larger ion-exchange capacity is. In fact, the Si/Al ratio of 1 is the lowest observed in zeolites because Al-O-Al connection is not favored in tetrahedrally connected frameworks due to unfavorable electrostatic interactions (Löwenstein's rule). In addition, other factors such as ionic size and/or pore volume also affect the ion-exchange capacity. If ionic size is larger than the pore opening of the zeolite, the ions are unable to enter or leave the pore system and ion exchange cannot take place. In the case of hydrated cations, their size can be decreased by losing some water molecules at elevated temperature. This ion sieving effect may lead to the complete exclusion of one sort of cation from a particular zeolite [31], or only partial exchange occurs [32]. Alternatively, pore volume of the zeolite may be large enough for the individual cation to diffuse through, however, not enough for the sum of the volumes of all the cations required to neutralize the anionic framework which results in partial exchange, called a volume exclusion effect [33].

2.2.3 Industrial application

The important applications of the zeolites are: molecular sieves, ion exchange, catalysts/fixed acids and inert supporting structures. As catalysts in the petrochemical and refining industries, zeolites are probably the most important present-day applications because of their shape selectivity. Zeolites can display different types of shape selectivity [34] in organic reactions as shown in Figure 2.6. Reactant selectivity allows only part of the reacting molecules to enter the catalyst pores. In product selectivity, only compounds

with the correct dimensions can diffuse out of the pores. A transition-state that is too large for the pore system is prevented from forming leading to transition state selectivity.

Reactant Shape Selectivity

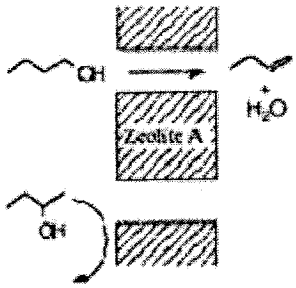

Product Shape Selectivity

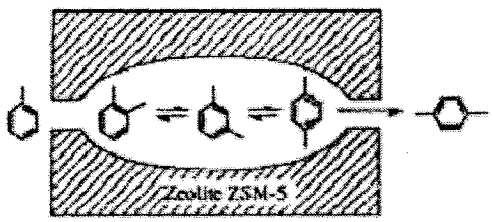

Transition-State Shape Selectivity

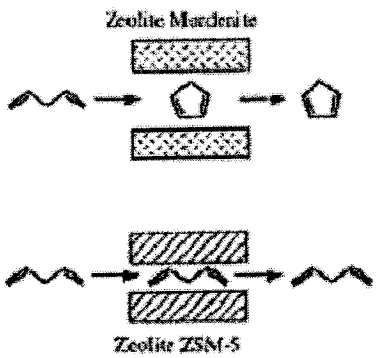

Figure 2.6 Different types of shape selectivity [35]

2.2.4 Advantages of zeolites

Several advantages of the heterogeneous zeolites can be considered as follows: (a) as an acidic catalyst used in reactions, compared to the homogeneous one, easily reproducible production catalyzed by well-defined zeolite surface, easy separation and disposal of the catalyst, avoidance of corrosion, etc; (b) as carriers for active components, bifunctional zeolitic systems can be easily designed and prepared by doping with suitable metals. In these cases, their shape selectivity often has an advantageous effect on the composition of the product; (c) in addition, the thermal stability of the zeolites permits them to be used at relatively high temperatures; (d) finally, zeolite catalysts can be regenerated readily by burning off the coke using air at 550°C.

However, most of zeolites have the pore size less than 1nm. The larger pore systems found in zeolites mostly are aluminophosphate (<1.5 nm); however, they are all unstable towards moisture and high temperature. Therefore, it is significant to design mesoporous materials with high thermal stability in order to process any bulkier/larger molecules.

2.3 Mesoporous materials-MCM-41

Researchers at Mobil discovered MCM-41 (Mobil Crystalline Material-41) in 1992. Hydrothermal synthesis of MCM-41 mesoporous solids is obtained from the calcination of aluminosilicate gels in the presence of surfactants. The MCM-41 material possesses a hexagonal array of uniform channels, high BET surface area ($\geq 1000 m^2 g^{-1}$) and large pore volume (0.7-1.2 $cm^3 g^{-1}$) [10]. The dimensions can be tailored from approximately 2nm to greater than 10nm in size through the choice of surfactant with different chain lengths [36], the use of expanders [37] and reaction conditions at high temperature [38].

J.S. Beck et al. [11] proposed a liquid crystal templating mechanism for the formation of these mesoporous materials, in which there are two possibilities. Pathway (1) was that the surfactant molecules self-assembly into hexagonal array of cylindrical micelles followed by inorganic silicate crystallization around these preformed surfactant aggregates. In fact, it stared from first self-aggregation of the surfactant into spherical micelle as shown in Figure 2.6b, in which hydrocarbon chains were gathered in the center and the hydrophilic groups were arrayed on the surface in contact with water surrounding the micelles. These micelles then elongated to rodlike micelles, and six of these rodlike micelles formed a hexagonal array of cylindrical micelles. Finally, the negatively charged silicate species in water occupied the space between the cylinders duo to electrostatic interaction with ammonia anions in surfactant. Pathway (2) was that silicate anions in solution were attracted by the cationic surfactants to balance the charge, which influenced in directing the formation of the supramolecular surfactant arrays. The final

calcination step was burning off the original organic surfactant, leaving hollow cylinders of inorganic material.

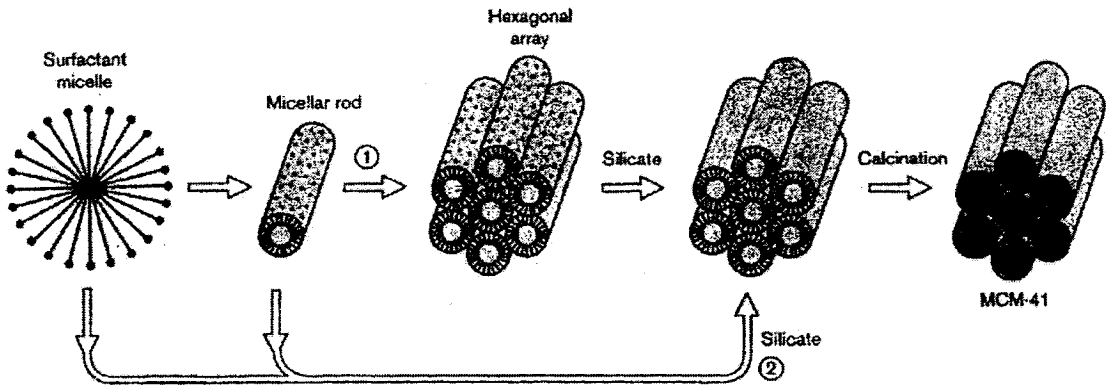

Figure 2.6b Possible mechanistic pathways for the formation of MCM-41
(1) Liquid crystal initiated (2) silicate anion initiated [11]

However, several problems of MCM-41 have been recognized compared to the zeolites: low catalytic activity because of low intrinsic acidity, insufficient thermal stability, and slow diffusion and short effective lifetime due to a one-dimensional system.

The self-assembly of surfactants in solutions has been widely investigated. The shape and size of the resulting aggregate such as spherical, globular or rodlike micelles, or spherical bilayer vesicles (Figure 2.7) are controlled by the molecular structure of the surfactant. Israelachvili, Mitchell, and Ninham proposed the concept of molecular packing parameter, which is defined as v/al, where v and l are the volume and the length of the surfactant tail and a is the area per molecule and derived the following well-known connection between the molecular packing parameter and the aggregate shape: $0 < v/al < 1/3$ for sphere, $1/3 < v/al < 1/2$ for cylinder, and $1/2 < v/al < 1$ for bilayer [39]. Therefore, to select molecules with the corresponding molecular packing parameter would yield desired structures such as spherical, globular or rodlike micelles, or spherical bilayer

vesicles. Myristyltrimethyl-ammonium bromide (MTMB) surfactant used as a template for MCM-41 self-assembled into rodlike micelles because its molecular packing parameter is between 1/3 and1/2.

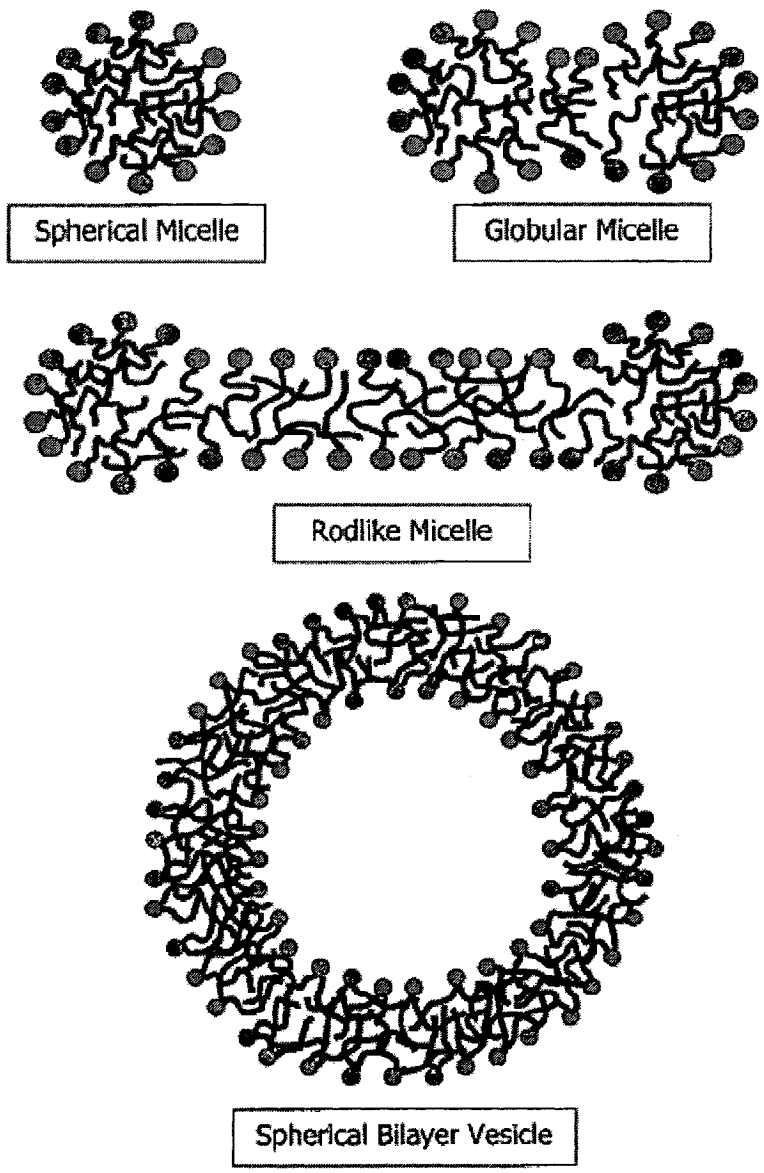

Figure 2.7 Schematic representation of surfactant aggregates in dilute aqueous solutions [40].

2.4 Secondary Synthesis Methods

Secondary or post-synthesis treatments have been utilized to produce many materials with desired catalytic properties that could not be achieved by direct synthesis of zeolites. These include increasing catalytic acid activity, improving thermal and hydrothermal stability, and enlarging pore size. The extent to which the properties are changed depends on the zeolites type as well as the method of treatment. In general, the techniques for post-synthesis modification of zeolites include: acid leaching, high temperature steam, and chemical treatments with chelates or fluoride compounds as well as combinations of these treatments. Each post-synthesis treatment method modifies the properties of the zeolite in slightly different ways. For example, acid leaching can selectively dealuminate a zeolite structure and wash the aluminum (Al^{3+}) out of the crystal. Hydrothermal dealumination removes the aluminum from the framework but does not remove it from the crystal; and amorphous aluminum ($Al(OH)_3$) can be collected on the crystal surface. Fluorosilicate treatment can delete the aluminum centered acid sites from the surface to form soluble AlF_6^{3-}.

In conclusion, dealumination results in enhanced thermal/chemical stability (higher Si/Al ratio), increased pore size (a secondary pore system -mesopores can be generated), increased hydrophobicity (generation of Lewis acidity and elimination Brönsted acidity). Moreover, hydroxyl nests can be generated and silicon, aluminum and other metal ions can be introduced into the framework at these nest sites to improve stability as well as to alter the catalytic properties.

In previous work in our lab, it was shown that mesoporous materials could be obtained from Al-rich zeolites by controlled dealumination using AHFS as Al removing

agent [15, 16, 17, 18] and the pore enlargement could occur without significant pore occlusion [17, 18]. They started with an initial diameter of 0.8nm in type X and 0.5nm in type A and got larger mesorpores after the treatment, which were in the region of 4nm and 12nm, respectively. This is due to different Si/Al ratio in the type X and the type A parent zeolites. Generally, the lower Si/Al ratio in the parent zeolite, the larger pore sized mesoporous material produced, the broader pore size distribution and the higher void volumes obtained. As the result, the dealuminated material from parent type X zeolite with 1.2 of Si/Al ratio has smaller pore of approximate 4 nm in size and sharper pore size distribution than that from A-type zeolite with equal ratio of Si/Al [17, 18]. Narrow pore size distribution means that homogenous pore sized system has been obtained.

It has been reported that the reactions of treatment with AHFS are shown in Figure 2.7b, illustrating that Si atoms from AHFS can substitute the zeolites Al sites [14b].

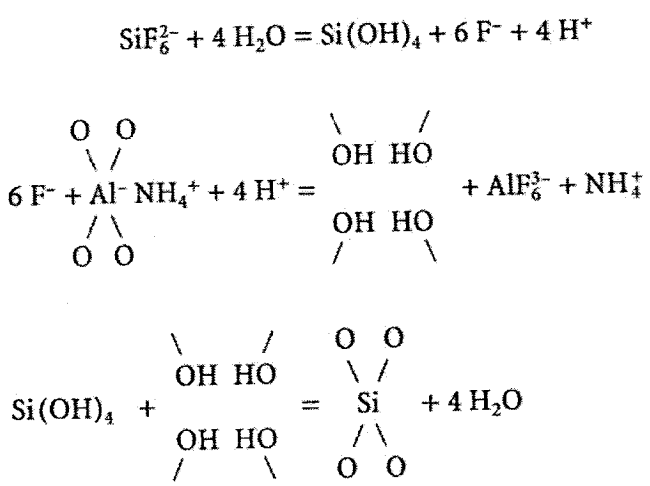

Figure 2.7b The process of AHFS dealumination [14b]
(Substitution of Al sites in zeolites with Si atoms from AHFS)

This is in contrast with more aggressive Al removing media such as mineral acids, as shown in Figure 2.7c (the formation of highly soluble $AlCl_3$), that usually lead to severe structural collapses; and thus not very useful mesoporous materials because the latter are subject to numerous pore occlusions [19] or a lack of direct connection with the external surface of the treated zeolite particle [20]. Several other advantages are associated with AHFS treatment such as the production of mesoporous materials that have high thermal stability and higher void volumes. It also has a highest cation exchange capacity [16, 18].

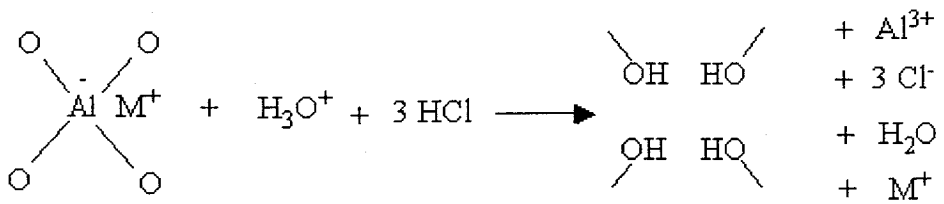

Figure 2.7c The process of acid mediated dealumination is proposed to take place through the extraction of aluminum from the framework

2.5 Methods for pore size engineering in ZSM-5 zeolite

ZSM-5 is short for Zeolite Socony Mobil and the number 5 standing for the average pore size of 0.56nm.

The ZSM-5 zeolite exhibits a three dimensional network of channels having a structure as illustrated in Figure 2.8. There exist two types of pore channels intersecting each other. One straight pore channel has circular opening of 0.54 x 0.56 nm, the other zigzag channel has an ellipsoidal pore opening of 0.51x 0.55 nm. It possesses a mean average pore diameter of 0.56nm circumscribed by 10 oxygen-atoms. It is the special structure of ZSM-5 that exhibits a high degree of shape selective catalysis and high thermal stability owing to high silica content. It has many useful applications in petroleum refining such as processing gas oils to obtain high quality gasoline by FCC process.

DRS (Desilication Reinsertion Stabilization) method [21] allows narrowing the pore size of the ZSM-5 micropores from the average value of 0.53nm down to 0.46nm. The optimal steps for pore size reduction by the DRS process involves (a) desilication with sodium carbonate; (b) ion-exchange of desilicated material from step (a) with ammonium chloride; (c) reinsertion of orthasilicic acid into the sample from step (b); (d) and final activation stepwise of the sample from step (c) to 700 °C overnight.

In this project, the above pore size narrowing technique was used to modify the mesoporous size created from dealumination rather than desilication.

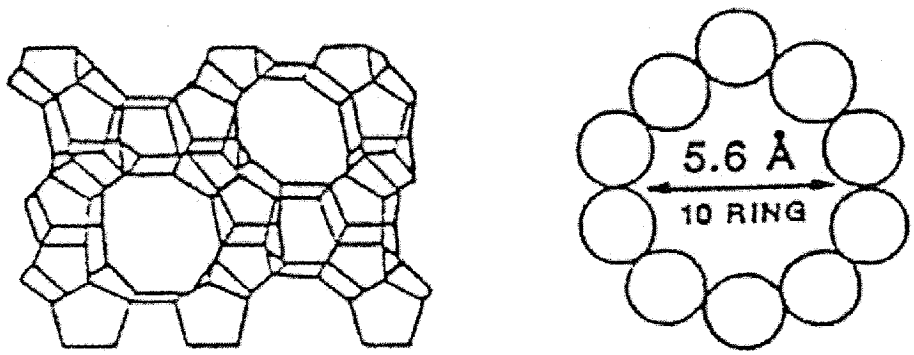

ZSM-5

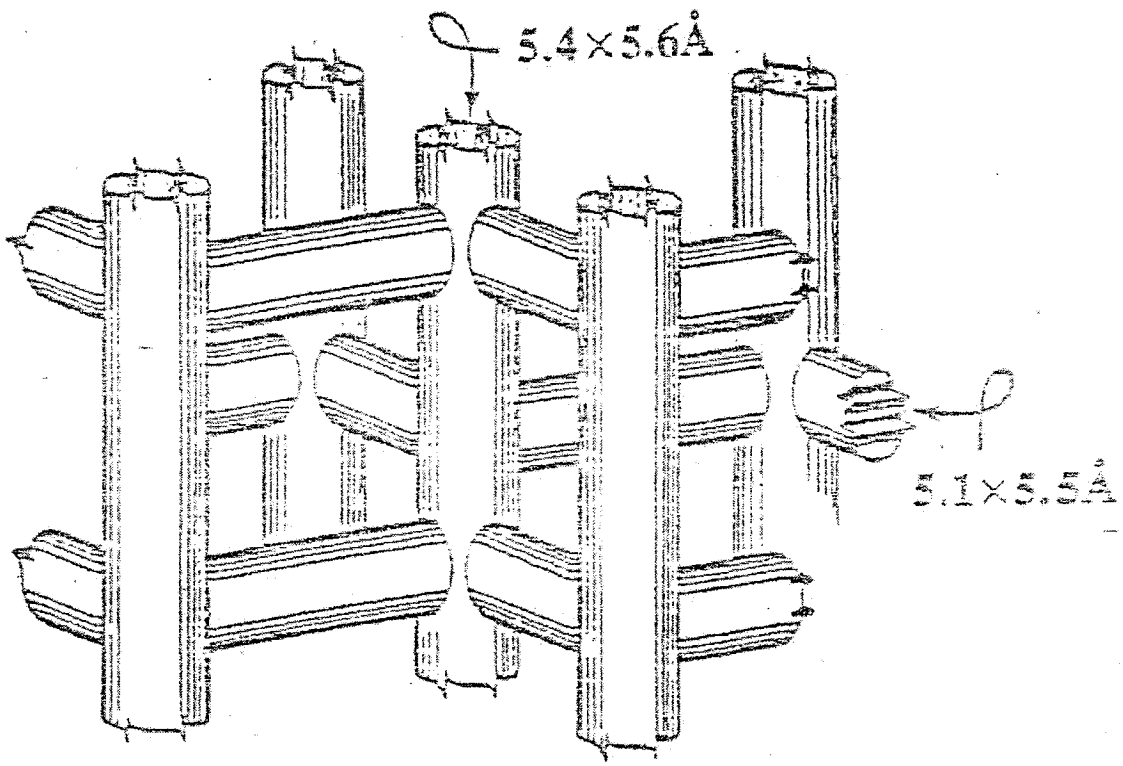

Figure 2.8 Framework structure and projections of ZSM-5

2.5 Introduction to solid superacids

The main advantage of solid superacids compared to liquid acid catalysts is the ease of separation from the reactor mixture, which allows continuous operation, as well as regeneration and reutilization of the catalyst. Furthermore, the heterogeneous solid catalysts can lead to higher selectivity or specificity.

Solid superacids can be divided into two groups, depending on the origin of the acid sites. One is called fixed catalyst whose acidity may be a property of the solid as part of its chemical structure (which possessing Lewis or Brönsted acid sites) such as ZSM-5 and type Y zeolite. Another important solid superacid is a combination of Lewis or Brönsted acids within an inert or low-acidity support. Incorporation of acidic species onto the surface of mesoporous materials may provide interesting acid catalysts with sufficiently large cavities to convert bulky molecules. Recently, several techniques have been reported for the production of hydrothermally stable and strongly acidic mesoporous aluminosilicates. These techniques include assemblies using protozeolitic seeds [41, 42], coating of protozeolitic nanoclusters onto the surface of preformed mesostructured aluminosilicates [43, 44], and deposition of an organic superacid, trifluoromethanesulfonic acid (TFA) into the surface of mesoporous material MCM-41 [45]. Kletnieks [45] recently found that the new catalyst has a much more improved catalytic activity compared to the traditional solid acid zeolite even though partially structural collapse (upon loading of the TFA) has been reported.

Trifluoromethanesulfonic acid (TFA) is one of the strongest acids known with the Hammett acidity function of $H_0 = -14.1$ (which in concentrated sulfuric acid, H_0 is only -12), yet it is nonoxidizing. It does not provide fluoride ions, even in the presence of

strong nucleophiles, and it possesses superior thermal stability and resistance to both oxidation and reduction [46]. Most importantly, the high acidity of TFA is capable of protonating certain weak bases such as saturated hydrocarbons to produce stable carbocations, which are essential intermediates in petrochemical reactions. The use of a heterogeneous TFA system, which can be achieved via incorporation of liquid TFA into an inert support by wet impregnation or dry impregnation techniques [47], would minimize the production of waste during TFA recovery. The inert support developed in this project is acidic silica nanoboxes called (m)H-dealX. Its chemical stability is derived from the maximum amount of loading TFA.

It is worth noting that, over the temperature range between 290°C and 320°C, L. Fabes and coworkers found that the decomposition of TFA in water occurred simultaneously by [a] and [b] pathways, as shown below; and the rate of decomposition was first order with respect to each of H^+ and $CF_3SO_3^-$ [48].

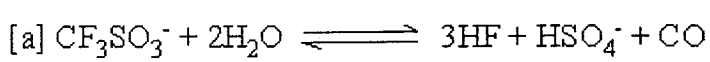

[a] $CF_3SO_3^- + 2H_2O \rightleftharpoons 3HF + HSO_4^- + CO$

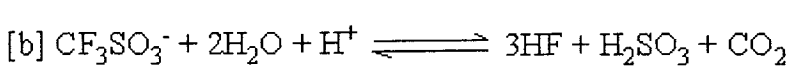

[b] $CF_3SO_3^- + 2H_2O + H^+ \rightleftharpoons 3HF + H_2SO_3 + CO_2$

The proposed mechanism for the reaction was nucleophilic attack of water on the S atom of TFA, generating S (VI) and CO, whereas attack of the water molecule on the C atom yields CO_2 and S (IV).

Chapter 3

Experimental Procedure

3.1 Source of Materials

The chemicals used in this work and their suppliers are shown below:

Chemicals	Supplier
Aluminum Reference Solution (1000ppm+/-1%)	Fisher Scientific
Amberlyst 15 ion exchange resin	Aldrich Chemicals Company Inc.
Ammonium chloride	ACP Chemicals Inc.
Ammonium Acetate (97+%)	Aldrich Chemicals Company Inc.
Ammonium hexafluorosilicate (99%)	STREM CHEMICALS
CaA (Type 5A)	Union Carbide Corporation
Hydrogen peroxide (30%) solution	ACP Chemicals Inc.
Hydrochloric acid (36.5-38.0%)	Fisher Scientific
Myristyltrimethyl-ammonium bromide	ACROS
NaX (Type 13X)	Union Carbide Corporation
Potassium bromide (FT-IR grade)	Aldrich Chemicals Company Inc.
Silica gel (60-200 mesh)	MALLINCKRODT Baker
Sodium hydroxide	ACP chemicals Inc.
Silicon Reference Solution (1000ppm+/-1%)	Fisher Scientific
Sodium orthsilicate	STREM CHEMICALS

Sodium Reference Solution (1000ppm+/-1%)	Fisher Scientific
Tetrapropylammonia hydroxide (TPAOH) 1.0 M solution in water	Aldrich Chemicals Company Inc.
Trifluoromethanesulfonic acid	STREM CHEMICALS

3.2 Dealumination of alumina-rich zeolites

The controlled dealumination of the NaX and CaA was carried out on the dealumination set-up as shown in Figure 3.1, with a solution of ammonium hexafluorosilicate (AHFS) in a manner similar to that reported in references 15,16,17,18 except reaction temperature at 80°C, the amount of AHFS and the injection rate of AHFS, etc. The basic procedure was as follows: 2.7g of NaX or 5.0g of CaA zeolite (powder form) were placed into a Teflon beaker containing 200cm^3 of 0.8mol dm^{-3} ammonium acetate solution (pH of 7.2). Then 20cm^3 of a freshly prepared 0.5mol dm^{-3} ammonium hexafluorosilicate (Aldrich) were added, under vigorous stirring, to the suspension using an injection syringe on an infusion pump. The rate of AHFS addition was kept at 0.81 and 1.7cm^3 min^{-1} for NaX and CaA, respectively. Then the medium was heated at 80°C in the water bath after the AHFS addition was completed. The mild stirring was continued for 1 hour for NaX and 1.5 hours for CaA. The solid was then separated by filtration and washed on the filter five times, each time with ca. 300cm^3 of distilled water. The product was dried in an oven at 110°C overnight in air and then activated at 250°C for 4 hrs. The resulting solids were named (m)Na-deal X and deal-CaA, respectively, m standing for monomodal materials. That is to say that this dealumination method produced totally mesoporous Na-dealX without the micropores.

However, bimodal materials which contained a large portion of mesopores and some micropores (remnants of the parent zeolite structure), were obtained using milder dealumination conditions as follows. A mass of 10.0g of NaX zeolite (in powder form) was placed into a Teflon beaker containing 200cm^3 of 0.8mol dm^{-3} ammonium acetate solution (pH of ca. 7.0). Then 25cm^3 of a freshly prepared 0.5 mol dm^{-3} AHFS aqueous

solution were added at room temperature and under vigorous stirring to the suspension using an injection syringe on an infusion pump. The rate of AHFS addition was kept at 0.9cm^3 min^{-1}. The slurry was then left at room temperature, always under vigorous stirring, for 2 hours. The solid was then separated by filtration and washed on the filter three times, each time with ca. 200cm^3 of hot distilled water. The product was dried in the oven at 110°C overnight in air and then activated at 250°C for 4 hours. The resulting material was noted (b)Na-dealX.

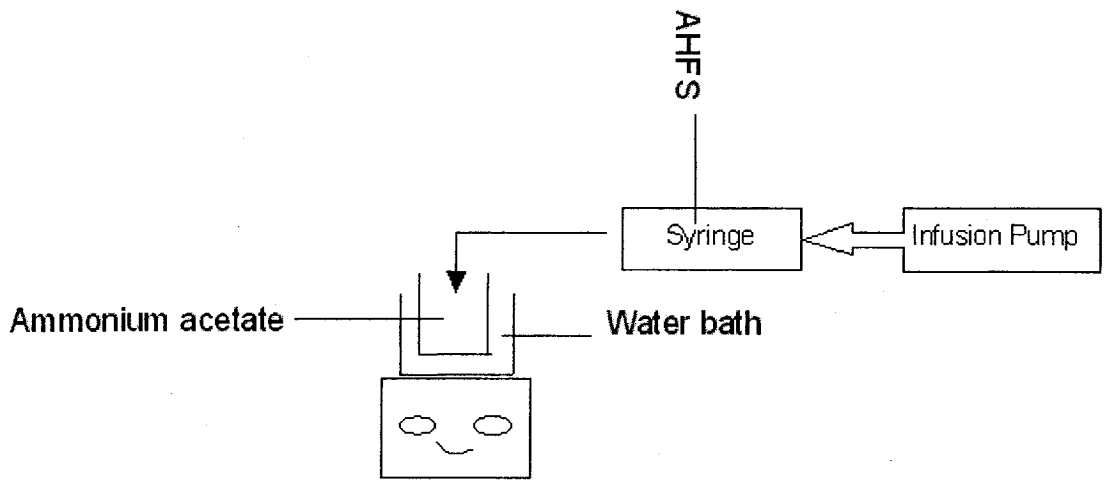

Figure 3.1 Dealumination apparatus systems

3.3 Preparation of the "acidic" silica nanoboxes

The "acidic" silica nanoboxes were prepared by ion exchange of Na-dealX with NH_4Cl solution, herein called NH_4-dealX followed by activation of the NH_4-dealX. The

resulting H-dealX materials can also be classified into two groups depending on the extent of dealumination. One is (m)H-dealX (m stands for monomodal), where only mesopores present in the materials and the other is (b)H-dealX (b stands for bimodal), where both micropores and mesopores present in the materials.

3.3.2 Ion exchange

In order to ion-exchange Na^+ with NH_4^+, the (m) or (b) Na-deal X sample was treated with an aqueous solution of NH_4Cl (5% by weight) in the Teflon beaker using 10 cm^3 of NH_4Cl solution for 1g of zeolite and heated the suspension at 80°C under mild stirring for 2 hours. This procedure was repeated twice for a total of 6 hours. After each treatment, the used solution was decanted and fresh solution was added. The resulting material was separated by vacuum filtration and washed on the filter with distillated water. The product was dried in an oven at 110°C overnight in the air and then activated at 250°C for 4 hours. The resulting solid was called herein (m) or (b) NH_4-deal X.

3.3.3 Activation

The acid form (H-dealX) silica nanoboxes were obtained by activating the NH_4-dealX sample by heating at 300°C for 3 hours, then increasing temperature to 600°C at the rate of 50°C per hour and keeping temperature at 600°C for a period of 17-18 hours.

Silica nanoboxes from CaA zeolite were prepared by dealumination with AHFS followed by calcination treatment as described for H-dealX .

3.4 Thermal stability

The thermal stability of NH_4 -dealX, Na-dealX and deal-CaA was investigated by two types of activated procedures:

A- TPC (a stepwise heating procedure, *i.e.* activated the samples at 300°C for 3 hours, then gradual heating to 600°C at a rate of 50°C per hour, finally heating at 600°C for 17-18 hours);

D- DH (Direct Heating, a two-step heating procedure, *i.e.* heated the samples at 300°C for 3 hours, then rapidly increasing the temperature to 600°C and finally keeping at that temperature for 3 hours)

3.5 Chemical stability

Studies of the chemical stability of the (m)H-deal X and calcined deal-CaA were performed by loading of triflic acid and sulfuric acid. For example, known volumes of an aqueous solution of triflic acid (0.0149g cm^{-3}) or sulfuric acid (0.0151g cm^{-3}) were added to 0.2g of (m)H-deal X sample by two techniques: wet impregnation and dry impregnation. In wet impregnation technique, the acid was added in one shot into (m)H-dealX powder and mixed well. The resulting suspension was then placed in the fume hood, at room temperature, to evaporate all the water for more than 5 hours. The apparently dried solid was further dried in the oven at 110°C overnight. In the dry impregnation technique, the total volume of acid solution was added to the powder in several steps, which was dependent on the mass of the sample and the solid pore volume. For example, it takes 10 steps if a total 0.8cm^3 of acid needs to be deposited into 0.2g sample with pore volume 0.4cm^3g^{-1}. After every addition of 0.08cm^{-3} of the acid, the

solid was placed in the fume hood for 20 minutes to evaporate the water. The obtained material was finally put in the oven at 110°C overnight.

3.6 Modification of the pore characteristics of the silica nanoboxes

Ion exchange of sodium orthosilicate (Na_4SiO_4) with H^+ was performed on Amberlyst 15 ion-exchange resin (acid form). A mass of 5.2g of the acidic resin was packed in a glass column and wetted with distilled water, and then 5cm^3 of aqueous solution of sodium orthosilicate (6wt%, kept in Teflon bottle) were passed through the resin column, using distilled water as elutant. The volume of the collected brownish liquid was ca. 60cm^3 and containing orthosilicic acid (H_4SiO_4). From 5 to 30g of the obtained liquid were then concentrated to a volume of 1-2cm^3 in a rotovap under vacuum and heated at 74°C. (m) H-deal X was then placed in this H_4SiO_4 solution; the evaporation was continued until the solid was completely dried. The resulting solid was further dried in an oven at 110°C overnight in the air and subsequently calcined at high temperature using the TPC procedure as described in 3.4.

3.7 The hydrothermal synthesis of MCM-41

Mixture A was obtained by weighing 20.8g of liquid tetrapropylammonia hydroxide (TPAOH) followed by addition of 3.0g sodium hydroxide, 110cm^3 distilled water, 18.3g of silica gel Baker. Mixture A then was heated at 80°C in the water-bath for 30 minutes with stirring. Mixture B was prepared by dissolving 17.2g of Myristyltrimethyl-ammonium bromide (MTMB, $C_{17}H_{38}BrN$) with 66 cm^3 of distilled water in 250cm^3 Teflon Beaker with stirring. Finally, mixture B was added to mixture A

and the suspension was heated at 80°C in the water-bath for another 30 minutes under stirring. The final mixture was then transferred into a Teflon bottle (using Teflon tape on threads) and placed in water bath at 95°C for 96 hours. The reaction was terminated by cooling the Teflon Bottle at room temperature. The solid product was recovered by vacuum filtration and washed with 1.5 liters of distilled water and dried in the 110°C oven in the air. The organic matter was removed by calcining the sample at 550°C for 6 hours.

3.8 Characterization of "acidic" silica nanoboxes

3.8.1 X-Ray Powder Diffraction (XRD)

XRD basically provides informations about the Bragg angles θ, the reflection of an incident monochromatic X-ray beam on crystal planes. The presence of a single and strong peak at low angle allows predication about the periodicity.

The X-ray powder diffraction method is based on the interactions between X-rays and crystals. X-rays are electromagnetic radiations of short wavelength and have high frequency and high energy. Crystals are capable to diffract a radiation. When a beam of X-rays hit a crystal, wave interference occurs between beams scattered by families of planes (hkl) in the crystal and a diffraction pattern is created as shown in Figure 3.2. The diffraction patterns followed Bragg Law, *i.e.*

$$n\lambda = 2d * \sin\theta$$

where n: the order of the reflection

λ: the wavelength

d: the distance between the planes of a given family

θ: the incident angle between the x-ray beam and the plane

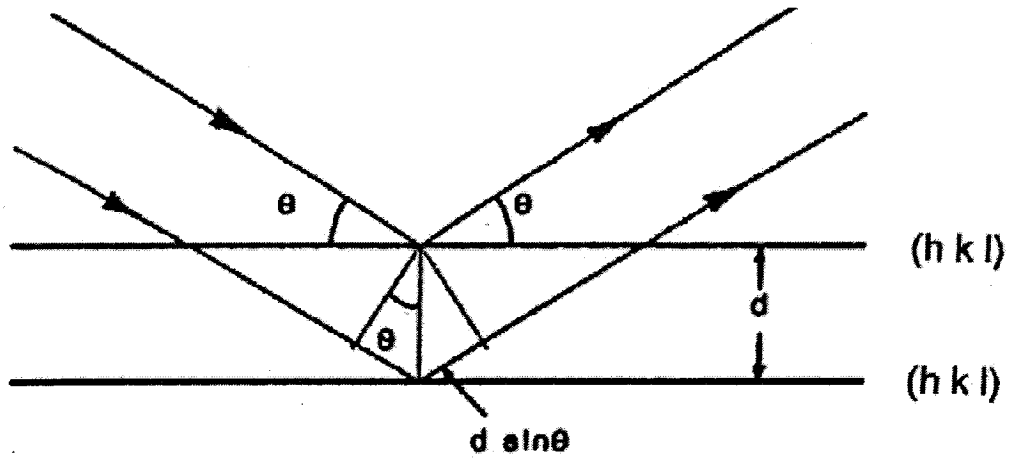

Figure 3.2 Diffraction of a monochromatic radiation by a crystal lattice

X-ray powder diffraction was carried out on a Philips PW 1050-25 diffractometer, using the Ni-filtered Kα radiation of copper (λ=1.54178 Å) and operating at 40kV and 20mA (power of 800W). The geometry of diffraction for the Philips line focusing diffractometer is shown in Appendix A. The patterns were reordered in the step-scanning mode, at an angular speed of 0.5° (θ) per minute with a step size of 2θ = 0.02°, in the angular range of 5 to 60° (2θ).

In particular, the X-ray powder diffraction pattern at small angles [over the angular range of 1 to 10.2° (2θ)] were collected in 0.02° steps and a count time of 1 sec/step on a Siemens D500TT automated diffractometer using Cu (Kα) radiation (λ=1.5405981Å), and equipped with a diffracted-beam graphite monochromator, a scintillation detector and

solid state counting electronics. The generator voltage and current setting were 45kV and 40mA, respectively, and it has the power of 1800W. This X-ray diffraction analysis was used to show the periodicity (homogenous distribution) of the nanosized cavities in the network of the silica nanoboxes. This was also carried out under highly collimated slit arrangement (0.1°) with the sample and holder and then the holder alone, in order to confirm that it was true diffraction of the sample and not an optical artifact of slits.

All of the samples were prepared for the XRD analysis by first being placed in the oven at 120°C overnight in the air to evaporate the adsorbed water, and then being finely ground by using a mortar and pestle and pressed in an aluminum sample holder (efficient to remove some bumps at low angles compared with Plexiglass ®) and make sure to form a smooth flat surface. A solid reference (pure silicon, main peak at 2θ of 28.44°) is scanned before the samples to ensure that the instrument is well calibrated. The peak intensity was the number of counts recorded by digital integrator during a scan.

3.8.2 Brunauer Emmet and Teller (BET) Technique

The textural properties of porous solids, such as the specific surface area, the pore volume, the average pore diameter, the pore shape, the pore size distribution as well as the shape of the nanometric cavities and pore opening can be determined using BET technique.

As previously discussed in Chapter 2, only physical adsorption between adsorbent and adsorbate is considered in the BET method. The most commonly used adsorbates are nitrogen and argon. However, since pure nitrogen is more available and less expensive

than argon, all the textural studies of solids and catalysts in this work are carried out on the basis of nitrogen adsorption isotherms.

Determination of textural properties was carried out with a Micromeretics ASAP 2000 Model system (in Appendix B). BET method was applied to measure the specific surface area (*i.e.* BET plot at relative pressure between 0.05 and 0.35). Microporous volume and surface area were measured by t-plot method. The t-plot is a linear curve of the adsorbed volume against t (the statistical thickness t of the adsorbed layer) in the range of 0.35 and 0.5nm. Its slope m is directly proportional to the surface area and its positive intercept by extrapolating the line to t = 0 corresponds to the adsorbed volume of micropores. The reference isotherm used to determine the dependence of t vs. p/p_o is Harkins-Jura equation: $t = (13.99 / (0.034 - \log (p/p_o)))^{1/2}$. Mesoporous volume and mesopore size distribution was measured by the method of Barrer, Joyner and Halenda (BJH). In mesopores regions, the adsorption capillary condensation takes place when p/p_o is greater than 0.4 based on Kelvin equation. From the adsorbed volume and the assumed pore geometry, it is possible to calculate the physical volume of pores and the average pore size. The pore size distribution was investigated by plotting the differential pore volume F = dV/ dlogD as a function of the pore diameter D (desorption phase, V and D in cm^3 and nm, respectively). Macrospore volume was the difference between the total uptake and the sum of microporous and mesoporous volume.

Pretreatment of the adsorbent was essential. The adsorbent surface will be freed of any adsorbed molecules by degassing the sample before the physical adsorption isotherm can be determined. The degassing process of the solid sample can be performed at room

temperature, or at a higher temperature to promote desorption of strongly adsorbed species. The lower the temperature, the longer the degassing process is.

The BET tube was cleaned with distilled water, then with acetone and finally, it was placed in an oven at 110°C overnight. The samples to be analyzed were placed in an oven at 110°C overnight to prevent any water vapor from adsorbing onto the surface. The dried empty tube was degassed on the ASAP 2000 instrument down to less than 5μm Hg pressure and weighed on a microbalance. Less than 0.25g of dried sample were added into the pre-weighed empty tube. The tube with sample was put back to the preparation sample port to be degassed to thoroughly remove any remaining adsorbate on the surface. All samples except superacid solids (deposition of triflic acid into supports) throughout the project were degassed at 250°C for a period of 4 hours under vacuum (final pressure lower than 5μm Hg). Meanwhile, the degassing conditions on solid superacid had been modified at 120°C for 6 hours under vacuum since the boiling point of triflic acid is 160°C under atmospheric pressure. After degassing the sample and cooling the tube down to room temperature, the net weight of sample was recorded and it was inserted with other run parameters in the ASAP 2000 program. Finally, the tube was connected to the analysis port of the instrument and the adsorption isotherm was determined at constant temperature. The full analysis lasted for 5-6 hours. The procedure is non-destructive and the sample can be reused after the test.

3.8.3 DTA/TGA

DTA / TGA techniques are used to identify the acidic species incorporated into the (m)H-dealX material as deposited liquid form and bound-to-the-surface form [49].

TGA is a technique in which the mass of a substance is measured as the temperature of the substance is varied. Changes in the mass reflect a decomposition or oxidation in the air of the substance. DTA detects the temperature changes between the sample and an inert reference material during a programmed change of temperature, involving an exchange of energy ($\Delta H \neq 0$), *e.g.* chemical change or first order phase transition. The peaks on the DTA curve show either exothermic (give off heat) or endothermic processes takes place in the sample upon heating, combined with the TGA curve, we can determine whether a chemical reaction or a first order phase transition (including classical types and solid state phase transition) occurs.

DTA and TGA were carried out on a PL Thermal Sciences, STA- 1500 Model apparatus (in Appendix C). The mass and microvolts were recorded versus temperature. The stepwise technique of temperature-programmed desorption was used. A starting temperature of 100°C was increased to 120°C at a ramp of 5°C min^{-1}, and then it was kept at 120°C for 1 hour in order to completely remove the adsorbed water. Finally the temperature was increased again to 600°C at a ramp of 5°C min^{-1}.

3.8.4 Atomic absorption spectrometry (AAS)

The chemical composition of the silica nanoboxes, *i.e.*, Si/Al ratio, can be determined by AAS.

AAS technique can be used for the analysis of the chemical composition of the various zeolite and zeolite-like samples. Before analysis, the solid samples must first be dissolved. The fusion melting method was well developed by Le Van Mao [50], involving accurately weighing the sample into two platinum crucibles; each sample was between 0.1100g and 0.1300g. The crucibles were then placed in an oven at 800°C for a period of 2 hours. They were then cooled and reweighed to obtain the net mass of sample. A 0.9g of the fusion mixture, which consisted of potassium carbonate and lithium tetraborate, in a ratio of 8 to 1 (w/w), was added into the pretreated sample. Finally the platinum crucibles with the mixture were replaced in the oven at 800 °C for another 2 hours, which helped in completing the decomposition of the sample. The resulting materials were first dissolved in the platinum crucible with a small amount of strong mineral acid mixture of $5cm^3$ of HCl ($12mol\ dm^{-3}$) and $10cm^3$ of H_2SO_4 (10% by volume) on the low level of the hotplate and then were transferred to $150cm^3$ beaker. The covered beaker was heated on low on a hotplate for 30 minutes. Then $4cm^3$ of 30% hydrogen peroxide was added to the beaker and the dissolution process underwent for a few minutes until effervescence ceased. The final solution was placed on a hotplate on low overnight, covered with a watch glass. After ca 16 hours, the solutions were cooled down and transferred to a $100cm^3$ volumetric flask. It was then diluted to the mark with distilled water. Appropriate dilute solutions were prepared from this stock solution. The standard solutions were prepared from 1000ppm standard solution of Al and Si.

The analysis of the chemical compositions in samples (Al_2O_3, SiO_2) was carried out on a Perkin-Elmer model 2380 Instrument (in Appendix D). The standard solutions of aluminum were prepared from 20ppm to 90ppm with an interval of 10ppm. All sample

solutions were diluted with distilled water in the ratio of 1:1 except (m)H-dealX sample and the absorbance of these samples were within the calibration curve range. The fuel used for analysis of aluminum and silicon was a mixture of nitrous oxide and acetylene to prevent the oxidation of refractory oxides Al_2O_3 and SiO_2. The atomic absorption conditions for Al and Si used in the experiment are shown in table 3.1.

Table 3.1 The atomic adsorption conditions for Al and Si [51]

Element	Wavelength (nm)	Slit (nm)	Linear Range (mg/ L)	Flame
Al	309.3	0.7	100.0	Nitrous oxide-acetylene
Si	251.6	0.2	150.0	Nitrous oxide-acetylene

3.8.5 Solid-state NMR spectroscopy (^{29}Si and ^{27}Al MAS NMR)

Solid-state NMR spectroscopy has been widely used as a tool to solve the structure of the zeolites. ^{29}Si and ^{27}Al MAS NMR are employed to investigate the structure of the Si-Al walls of the nanocavities as well as their chemical composition (Si/Al ratio).

Solid-state NMR spectroscopy gives information on the local order of the structure and thus applied to structural studies of zeolites and related systems. In contrast to liquids NMR, solids NMR suffered from the considerable line broadenings characterized by indistinct chemical shifts (line positions) and intensities (integrated peak area) owing to specific interactions of the nuclear spins tightly bound in the rigid lattice of the solid sample. By using MAS (Magic-Angle Spinning) technique, *i.e.*, fast rotation of the

sample about an axis inclined at the angle θ =54°44' to the direction of the external magnetic field, the problem of line broadenings can be significantly reduced.

In the framework structure studies, the ^{29}Si NMR spectra provide informations on local environment of the SiO_4 tetrahedra, namely SiO_4Al_4, SiO_4Al_3Si, $SiO_4Al_2Si_2$, $SiO_4Al_1Si_3$, SiO_4Si_4 from the chemical shift data, and the relative concentration of the various units present in the structure from the signal intensities; and the ^{27}Al NMR tell us the framework or non-framework aluminum atoms or both existed in the materials based on the chemical shifts. The chemical shift of framework aluminum atoms in tetrahedral configuration of AlO_4 is between 55 and 68 ppm and that of non-framework aluminum atoms in octahedral symmetry of AlO_6 is 0 ppm [29c].

The ^{27}Al NMR spectra are much simpler than the ^{29}Si NMR. Since according to Löwenstein's rule (which forbids AlOAl pairings) only a single tetrahedral environment ($Al(OSi)_4$) exist in the zeolite framework. Consequently, the ^{27}Al NMR spectra of hydrated zeolites consist of only one line of framework aluminum atoms in a relatively small range of chemical shifts between 55 to 68 ppm (referenced to aqueous $Al(NO_3)_3$ solution about 60 ppm). Non-framework aluminum species in zeolites, originating from dealumination by thermal treatment, are octahedrally coordinated (AlO_6) and cause a ^{27}Al signal at about 0 ppm. A broad signal at 30-50 ppm may be caused by a non-framework aluminum species in a disturbed tetrahedral coordination or a penta-coordinated state [52].

Single-pulse ^{29}Si and ^{27}Al MAS NMR were performed on Bruker DSX300 at operating frequency of 7 T (300.13 MHz ^1H frequency). Samples were packed in 4-mm o.d. rotor. ^{29}Si MAS NMR spectra were recorded with a 2μs-20°-pulse at a spinning frequency of 6kHz as the scans between 1100 and 3000 with 20s repetition time. Sodium

salt of 2,2-dimethyl-2-silapentane-5-sulphonic acid (DSS) was used as reference for the ^{29}Si chemical shift. ^{27}Al MAS NMR spectra were obtained with a 2μs-20°-pulse at a rotation frequency of 12-14kHz as the scans between 240 and 8000 with 1s repetition time. The ^{27}Al chemical shifts were reference to $AlCl_3.6H_2O$.

Chapter 4

Results and Discussion

4.1 Synthesis of silica nanoboxes

In previous studies [15,16,17,18], dealumination of NaX and CaA with AHFS solution resulted in mesoporous materials with different pore size and pore size distribution, which was generally dependent upon the parent zeolites. It was found that larger mesopores and broader pore size distribution were obtained with Al-richer zeolites.

4.1.1 Dealuminated mechanism in alumina-rich zeolites

It has been found that Si atoms from AHFS can substitute the zeolite Al sites during dealumination of type Y zeolite (Si/Al ≥ 2.5) with AHFS [14b]. The reaction between AHFS and zeolites is shown in Figure 4.1a. Generally, the aluminum atoms in alumina-poor zeolites such as type Y are separated by several silicon atoms, and can be considered as isolated Al sites. Therefore, AHFS extracts only aluminum atoms and leaves silanol "nests" behind. Afterwards, silica from the hydrolysis of AHFS can be selectively deposited into some dealumination sites. The overall stoichiometric equation is:

$$Na^{+}\underline{AlO_4^{-}} + (NH_4)_2SiF_6 \rightarrow \underline{SiO_4} + (NH_4)_2AlF_5 + NaF \quad [53]$$

where the species underlined represented species which were connected to the zeolite framework.

However, the dealuminated procedures from the alumina-rich zeolites such as NaX and CaA by the extracting agent AHFS is more or less different from that in alumina-

poor zeolites such as type Y as illustrated in Figure 4.1b. Hydrolysis of AHFS results in formation of F^- and proton H^+, which attack the Al sites on zeolite surface to form soluble AlF_6^{3-}. Keep in mind that in alumina-rich zeolites such as NaX and CaA (Si/Al atom ratio is about 1.2 and 1.0 as shown in table 4.7 and 4.8, respectively), much more Al sites are present in the framework where they are separated from each other by one or two Si atoms. As a result, when AHFS extracts the adjacent aluminum atoms, it can also remove the small SiO_4 species linked to the extracted Al atoms (called Al clusters), leading to empty sites on the zeolite surface. In accordance with the results of references 15, 16, 17 and 18, we found that:

a) Most of the SiO_4 species formed by this reaction are not reinserted into the zeolite framework: they are instead removed by the AHFS solution, leading to empty sites on the zeolite surface. This Al removing phenomena, being gradual and homogeneous, results in a general pore enlargement as in pathway 1 of Figure 4.1b.

b) Some other SiO_4 species remained trapped in the newly formed cavities, and may affect the pore characteristics of the mesoporous materials when the material is activated at high temperature. This is ascribed to the mobility of these debris upon heating at high temperature as shown in pathway 2 of Figure 4.1b.

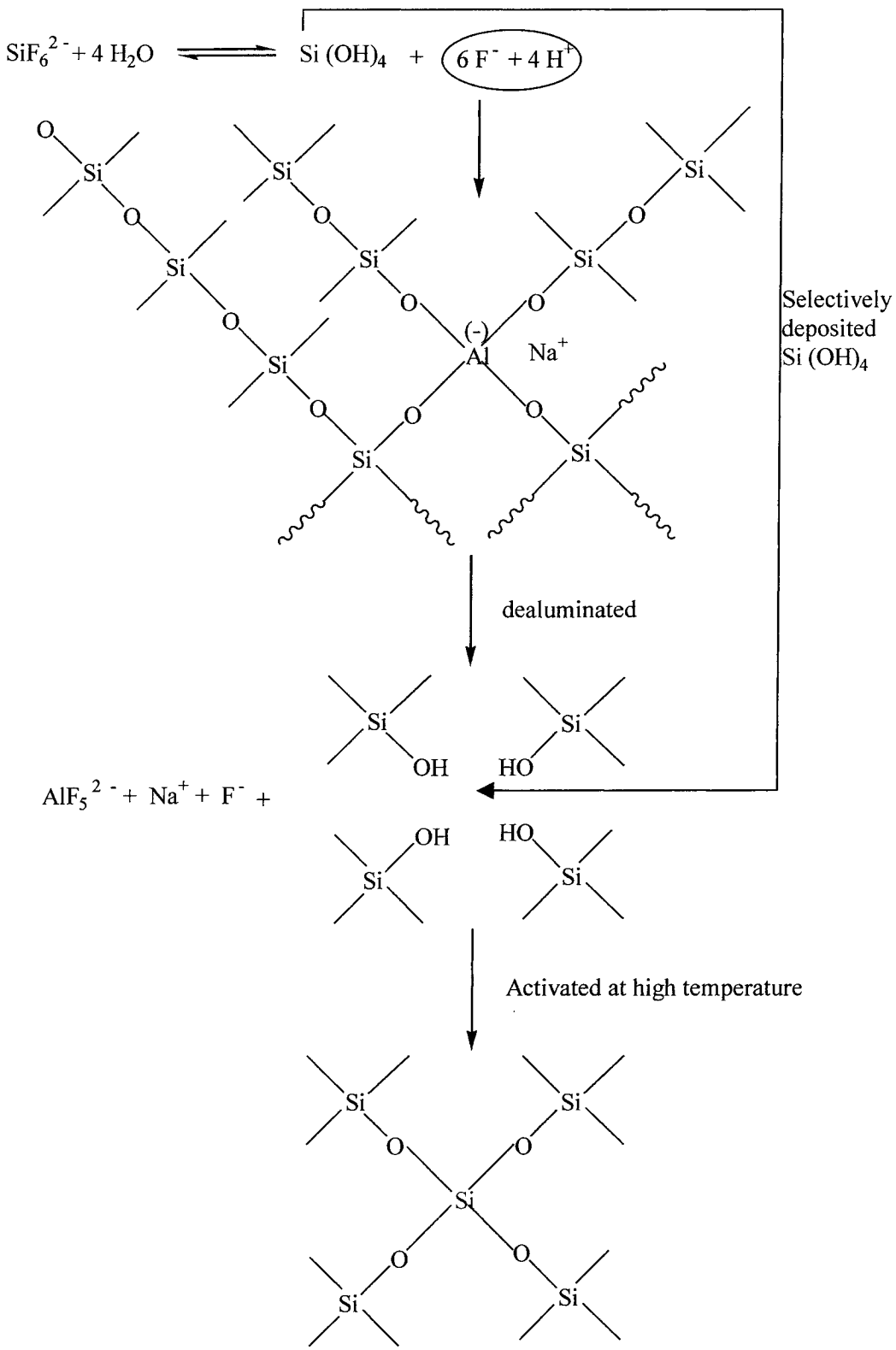

Figure 4.1a Dealumination in alumina-poor zeolites such as Y type

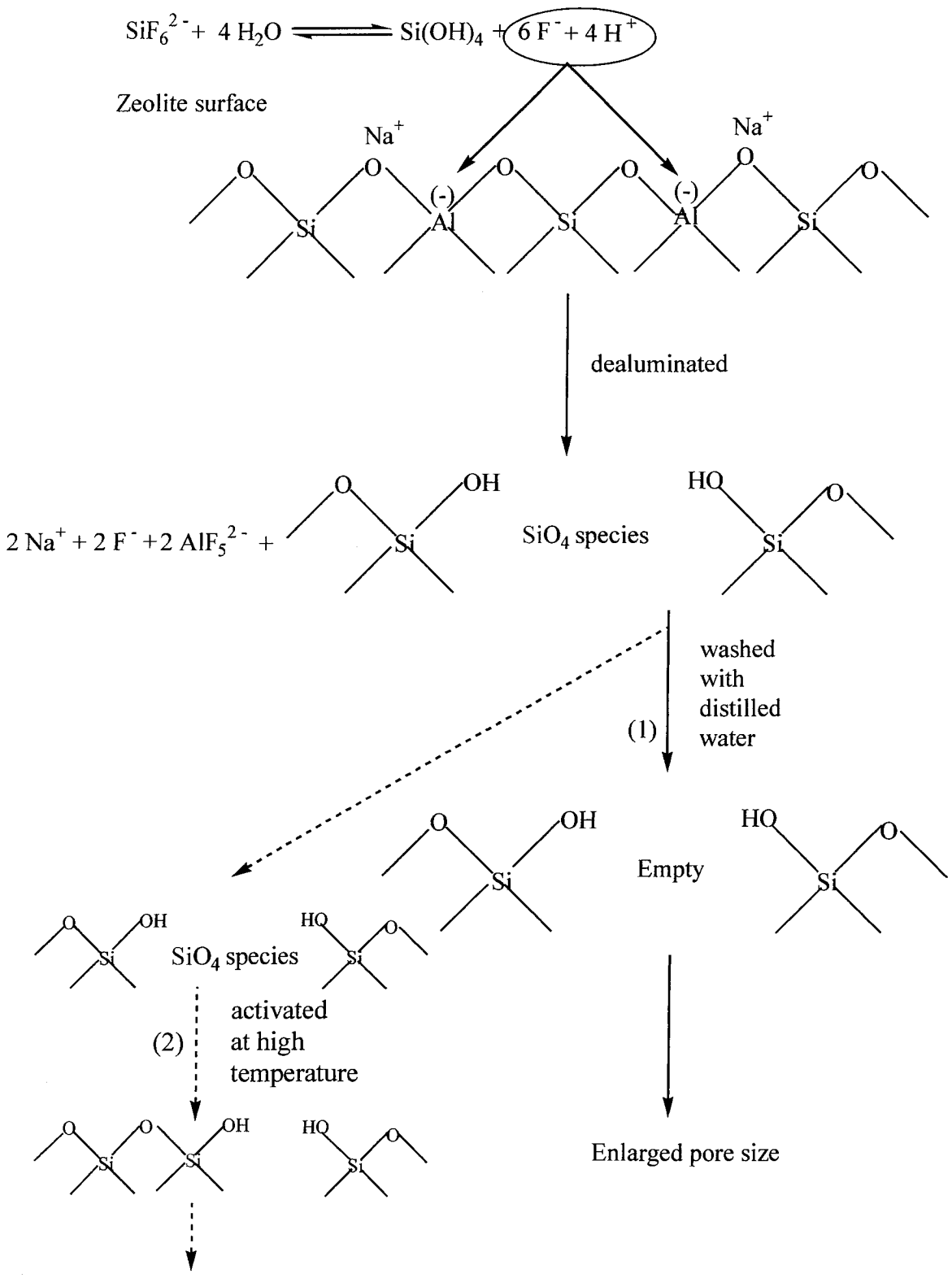

Figure 4.1b Dealumination in alumina-rich zeolites such as NaX, CaA

4.1.2 Parameters affecting the dealumination with AHFS solution

High quality dealuminated mesoporous materials or "good" silica nanoboxes from NaX and CaA (herein designated as (m)Na-dealX and deal-CaA) possess the following pore and surface area characteristics (criteria for obtaining silica nanoboxes):

a) No micropores;

b) Single and narrow mesopore size distribution curve (F=dV/dlogD);

c) Relatively high surface area.

In previous studies of our group [15,16,17,18], dealumination of 2.7g of NaX and 3.0g of CaA with AHFS in the buffer medium ammonium acetate were well developed and the results showed that the aluminum removal by AHFS is gradual and homogeneous resulting in a general pore enlargement. In this project, the optimal dealumination conditions for producing the materials as with good characteristics described above with AHFS from NaX and CaA are determined. These main dealumination parameters involving reaction temperature, total amount of AHFS addition and stirring rate as well as flow rate of AHFS injection, were investigated and the results are shown in Table 4.1.

In the following, the effect of dealumination parameters as a function of an arbitrary "significance value" is reported. The latter is a "pseudo"- statistical value which shows the goodness of the obtained materials. If the characteristics of the material are in perfect compliance with the three criteria previously mentioned, the value is equal to 3. If only one criterion is satisfied, its value is 1. Thus the "significance value" ranges from 0 to 3. It gives an idea about the compliance of the dealuminated materials with the criteria for obtaining silica nanoboxes. Significance value of 3 means that you have obtained good silica nanoboxes.

From the results, the optimal conditions for dealuminating 2.7g of NaX zeolite are as follows:

a) Dealumination temperature:

The reaction temperature is one of the main parameters. The optimum temperature range for 2.7g of NaX is between 60°C and 80°C (Figure 4.1c) because the silica nanoboxes can perfectly meet the three criteria using standard treatment conditions (addition of $20cm^3$ of AHFS ($0.5mol\ dm^{-3}$) at flow rate of $0.81cm^3min^{-1}$ in $200cm^3$ of ammonia acetate).

b) Amount of AHFS injection:

Enough amount AHFS ensures that sole mesopores are present in the dealuminated materials. The volume of $0.5mol\ dm^{-3}$ AHFS solution injected to the reaction medium, sufficient for 2.7g of NaX zeolite to produce the materials with required characteristics, ranges from $15cm^3$ to $20cm^3$ (Figure 4.2) (80°C with addition flow rate of $0.81cm^3min^{-1}$ in $200cm^3$ of ammonia acetate).

c) Mild stirring rate:

The material obtained by mild stirring (level of ca 1.5) has a single and narrow pore size distribution (Figure 4.3). However, the material prepared by rapid stirring rate shows two peaks for the pore size distribution curves (addition of $20cm^3$ of AHFS at a flow rate of $0.81cm^3min^{-1}$ in $200cm^3$ of ammonia acetate at 80°C). This is because rapid stirring (mechanical force) can remove Al containing debris from the structure in a more complete way.

d) The optimal flow rate:

From the Table 4.1, one can find that the injection flow rate of AHFS has an effect

on the textural properties. In general, lower flow rate results in the lower surface area of the sample (Figure 4.4). This is probably due to the longer time the zeolite had been exposed to the corrosive AHFS solution, resulting in loss of more aluminum atoms from the structure.

It is worth noting that buffer solution of ammonium acetate is used to keep the reaction medium at constant pH value of 7.2, *i.e.,* the buffer strength is sufficient to withstand the change in the AHFS concentration at any time. The addition of AHFS is controlled by using the infusion pump. Both methods can effectively prevent structural collapse from loss of many aluminum atoms, and also produce one narrow pore size distribution.

Table 4.1 Determination of dealumination parameters

Parameters	Experimental conditions	Variations	Micropore area m^2/g	Pore size distribution	BET Surface area (m^2/g)	Significance
Temperature (°C)	2.7g * (200,20)** 0.81***	23 (R.T.)	62 (-)	1 peak (+)	491(+)	2
		40	42 (-)	1 peak (+)	501 (+)	2
		60	0 (+)	1 peak (+)	491 (+)	3
		80	0 (+)	1 peak (+)	426 (+)	3
Total amount AHFS injection (cm^3)	2.7g * (200,b)** 0.81***	7	104 (-)	1 peak (+)	431 (+)	2
		12	53 (-)	1 peak (+)	380 (-)	1
		15	0 (+)	1 peak (+)	431 (+)	3
		20	0 (+)	1 peak (+)	426 (+)	3
Stirring rate (level)	2.7g * (200,20)** 0.81***	Fast (5)****	0 (+)	2 peaks (-)	405 (+)	2
		Mild (0.5)****	0 (+)	1 peak (+)	426 (+)	3
Flow rate (cm^3 min^{-1})	2.7g * (200,20)**	0.4	10 (-)	2 peaks (-)	390 (-)	0
		0.6	7 (-)	2 peaks (-)	421 (+)	1
		0.81	0 (+)	1 peak (+)	426 (+)	3

* Mass of NaX
** (a, b) -a cm^3 of 0.85mol dm^{-3} ammonium acetate, b cm^3 of 0.5mol dm^{-3} AHFS
*** Flow rate of 0.5mol dm^{-3} AHFS injection
****Stirring levels on hotplate

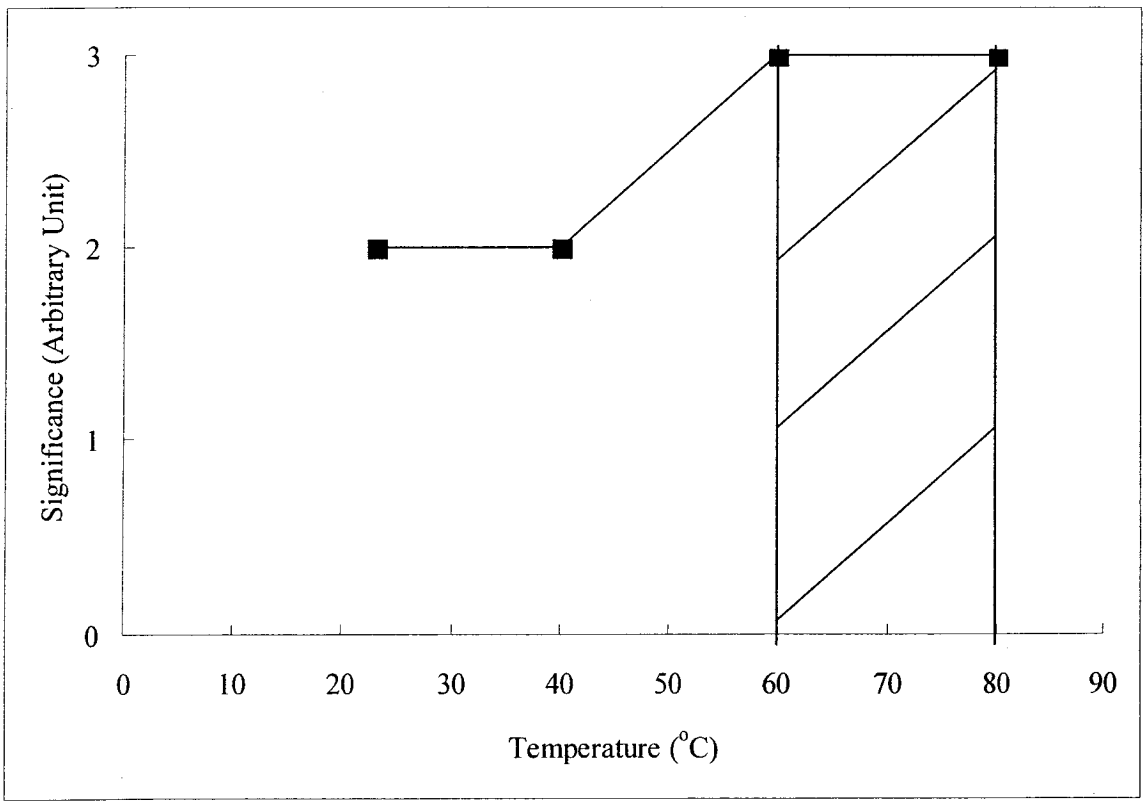

Figure 4.1c Determination of dealumination temperature

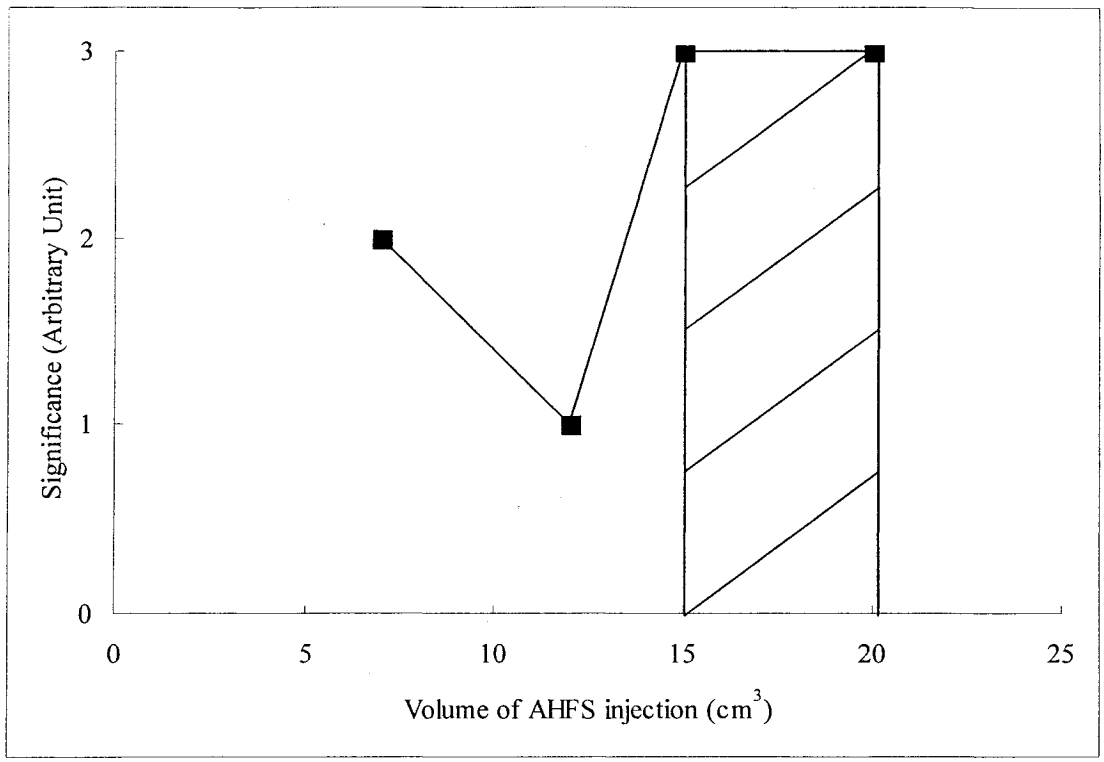

Figure 4.2 Determination of total amount of AHFS addition

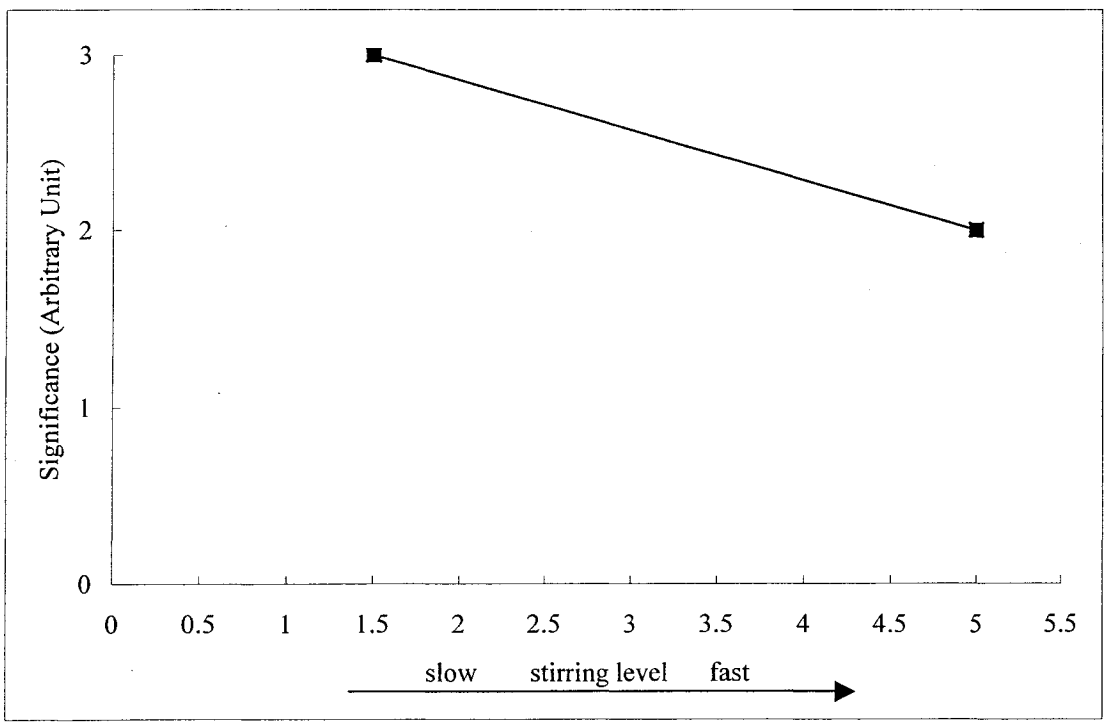

Figure 4.3 Determination of stirring rate

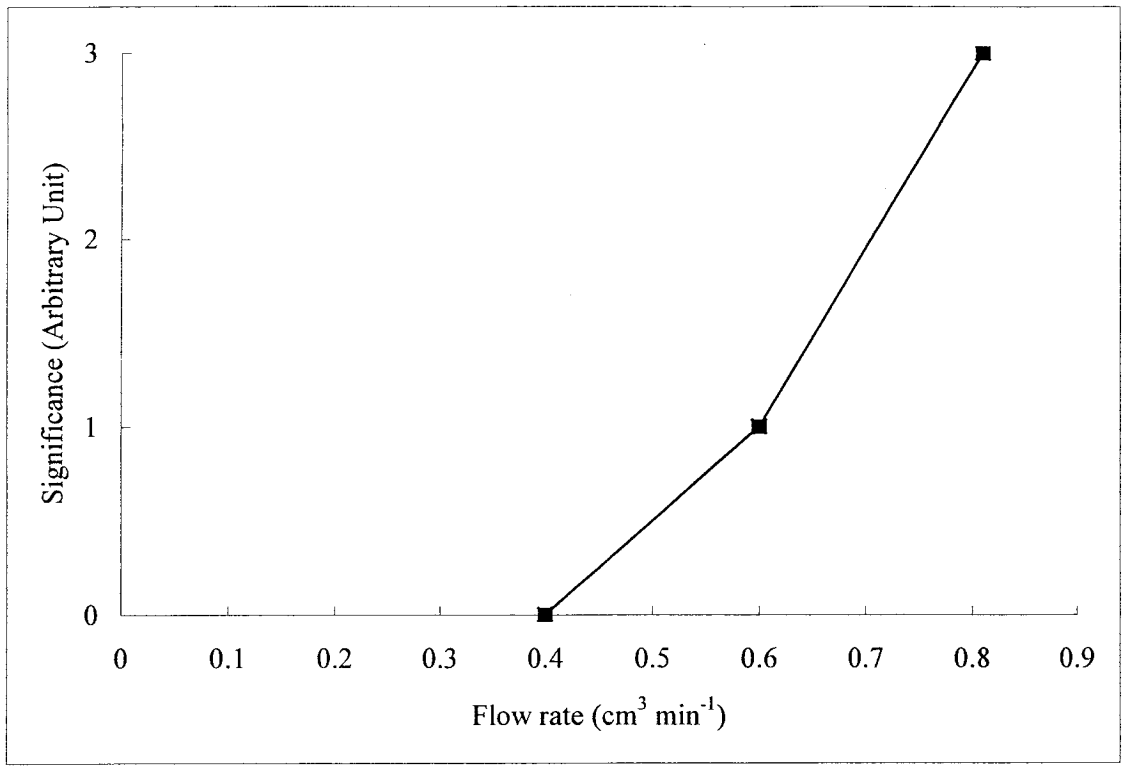

Figure 4.4 Determination of AHFS addition flow rate

Therefore, in order to produce the desired (m)Na-dealX nanoboxes, the dealumination procedures for treating 2.7g of NaX are followed: 2.7g of parent NaX were placed in Teflon beaker containing 200cm^3 of 0.8mol dm^{-3} of ammonia acetate. Under moderate stirring, 20cm^3 of 0.5mol dm^{-3} AHFS was added at room temperature at a flow rate of 0.81cm^3 min^{-1} using an infusion pump. After the AHFS addition, the beaker was kept at 80°C under mild stirring for one hour. Finally the sample was washed with distilled water. Following the above procedure, we synthesized several batches of (m)Na-dealX sample and they exhibit a good reproducibility as shown in Table 4.2.

Table 4.2 Collection of (m)Na-dealX samples

Batches No.	S_{BET} $m^2 g^{-1}$	S_{cum} $m^2 g^{-1}$	S_{mic} $m^2 g^{-1}$	D_{av}, nm	V_t $m^3 g^{-1}$	V_{mes} $m^3 g^{-1}$	V_{mic} $m^3 g^{-1}$	V_{mac} $m^3 g^{-1}$
NaX parent	740	22	696	0.8	0.30	0.02	0.28	0.00
1/(m)Na-dealX	463	534	0	4.4	0.55	0.49	0.00	0.06
2/(m)Na-dealX	367	451	0	5.0	0.51	0.47	0.00	0.04
3/(m)Na-dealX	450	499	10	4.5	0.47	0.47	0.01	0.00
4/(m)Na-dealX	439	520	0	4.6	0.56	0.51	0.00	0.05
5/(m)Na-dealX	507	596	0	4.4	0.61	0.56	0.00	0.06
Mixture of the above (m)Na-dealX samples	436	523	0	4.6	0.56	0.51	0.00	0.05

A total of about 20g of (m)Na-dealX mesoporous material were obtained, with BET surface area 436m^2 g^{-1}, average pore diameter around 4.6nm and one sharp pore size distribution d_{av} = 4.6 ± 1.0 nm (Figure 4.6), without micropores. Moreover, cumulative surface area (S_{cum}) obtained from nitrogen desorption isotherm in (m)Na-dealX materials is much larger than that of specific surface area (S_{BET}) (Table 4.2): this might be ascribed to the existence of intersections between the capillaries [27b], *i.e.* our materials were not isolated but truly interconnecting nanoboxes.

On the other hand, most of the optimal dealumination conditions for 2.7g of NaX can be used to modify 5.0g of CaA zeolite except with 1.7cm^3min^{-1} flow rate of AHFS injection and the slurry was kept at 80°C for 1.5 hours instead of one. The pore characteristics of each batch and the mixture of all batches are shown in Table 4.3. The resulting mesoporous deal-CaA has a surface area of about 250m^2 g^{-1}, an average pore size diameter around 15.1nm, and a quite broad pore distribution d_{av} = 15.1 ± 3.0nm (Figure 4.5) in contrast to the narrow distribution of (m)Na-dealX sample.

Table 4.3 Collection of deal-CaA sample out of 5 batches

Batches No.	S_{BET} $m^2 g^{-1}$	S_{cum} $m^2 g^{-1}$	S_{mic} $m^2 g^{-1}$	D_{av} nm	V_t $m^3 g^{-1}$	V_{mes} $m^3 g^{-1}$	V_{mic} $m^3 g^{-1}$	V_{mac} $m^3 g^{-1}$
CaA parent	661	26	614	0.5	0.27	0.02	0.25	0.00
1/deal-CaA	222	232	34	15.3	0.83	0.78	0.02	0.03
2/deal-CaA	186	235	9	15.5	0.82	0.76	0.01	0.05
3/deal-CaA	220	219	36	14.8	0.78	0.72	0.02	0.04
4/deal-CaA	244	246	44	14.3	0.80	0.77	0.02	0.01
5/deal-CaA	247	249	43	15.5	0.88	0.83	0.02	0.03
Mixture of the above deal-CaA sample	251	230	61	15.1	0.80	0.77	0.03	0.00

4.1.3 Comparison of Na-dealX and deal-CaA

The extent of pore enlargement by controlled dealumination of NaX and CaA zeolites with AHFS are found to depend on the Al composition (or the Si/Al ratio) in the parent sample. The larger the ratio, the larger the average pore size produced, and the narrower the pore size distribution obtained. The Si/Al atom ratios of the parent CaA and NaX are 1.0 and 1.2, respectively. As expected, the deal-CaA has a larger pore size (around 15.1nm) and broader pore size distribution (Figure 4.5) compared to the (m)Na-dealX which shows a narrower pore size distribution (Figure 4.6) with an average pore size of about 4.6nm.

In general, NaX and CaA zeolites are typically micropores with normal average pore size less than 1nm (0.8nm for NaX and 0.5nm for CaA); however, there also exists to some minor extent mesopores as defects in the materials (Figure 4.8 and Figure 4.9). Such mesopores at defect sites are capable of adsorbing a large number of reactant molecules AHFS. As we mentioned earlier, AHFS removed silicate species from the zeolite by extracting the Al atoms, which defined the cleavage lines of the structure. Since Al-rich zeolite can supply many Al-cleavage points, it is believed that pore

enlargement in NaX zeolite mostly appeared in the original mesopores by comparison of Figure 4.6 and 4.8. In the case of CaA zeolite (Figure 4.9), acid leaching and hydrothermal treatment lead to only one pore size distribution of 3.5-4.5nm [54]; on the other hand, a treatment with AHFS produces larger mesopores with an average pore size of ca. 15.1nm and a quite broad pore size distribution as shown in Figure 4.5. It is not clear how the dealumination techniques selectively remove the Al containing species from different sites.

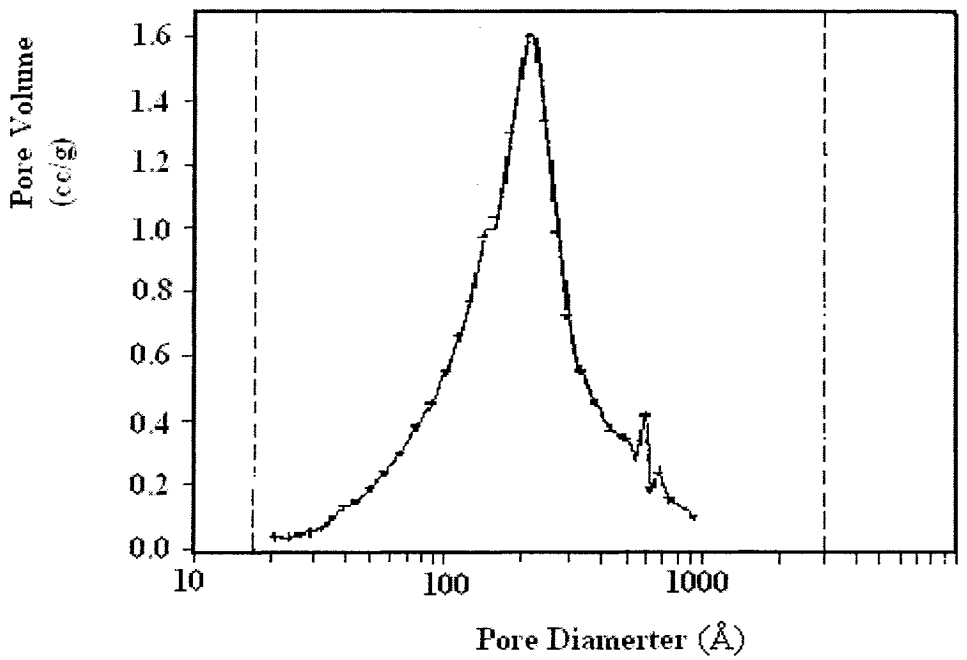

Figure 4.5 dV/dlog(D) desorption pore volume plot of deal-CaA at 250°C

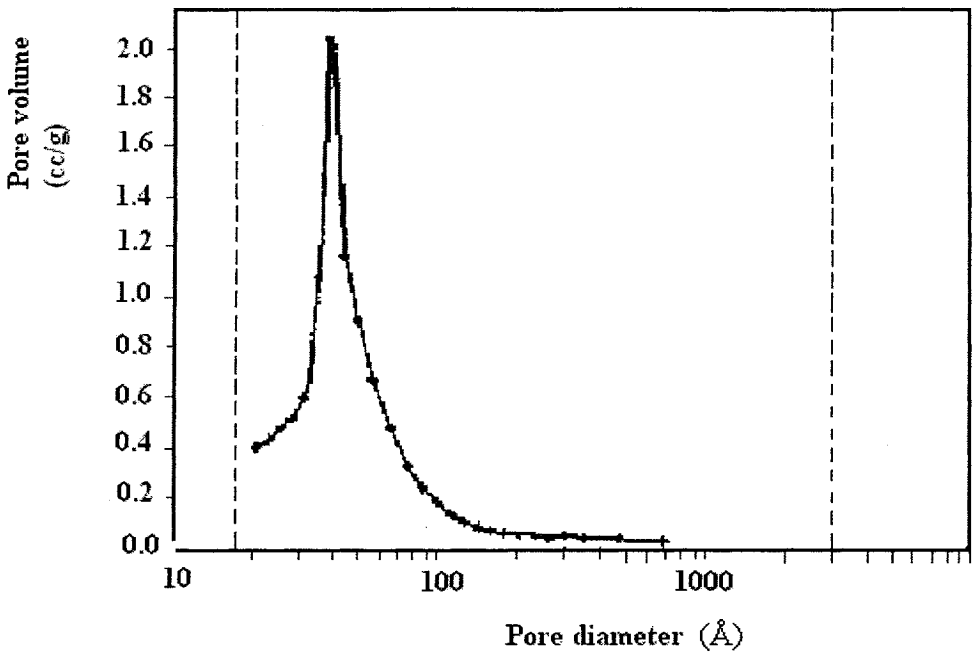

Figure 4.6 dV/dlog(D) desorption pore volume plot of (m)Na-dealX at 250°C

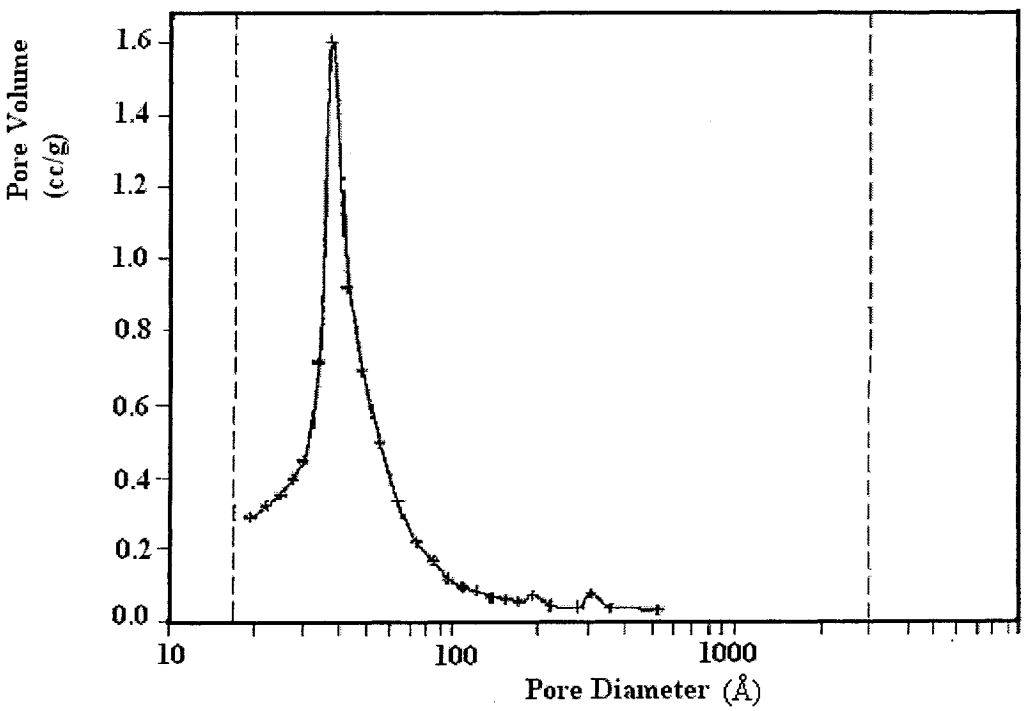

Figure 4.7 dV/dlog(D) desorption pore volume plot of (m)H-dealX at 250°C

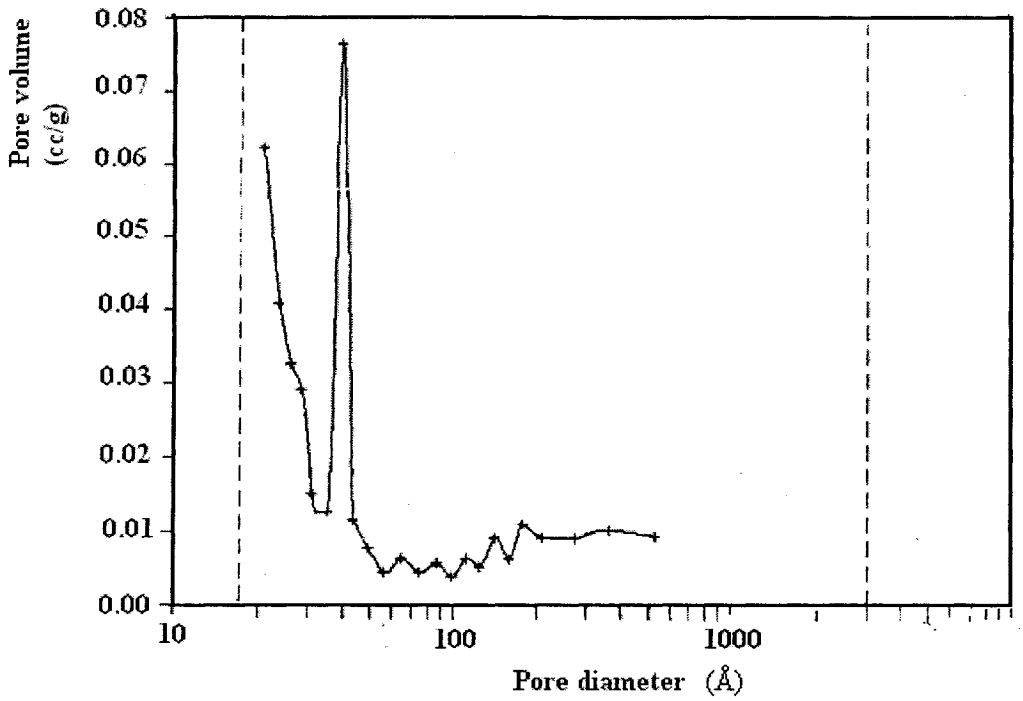

Figure 4.8 dV/dlog(D) desorption pore volume plot of parent NaX zeolite at 250°C

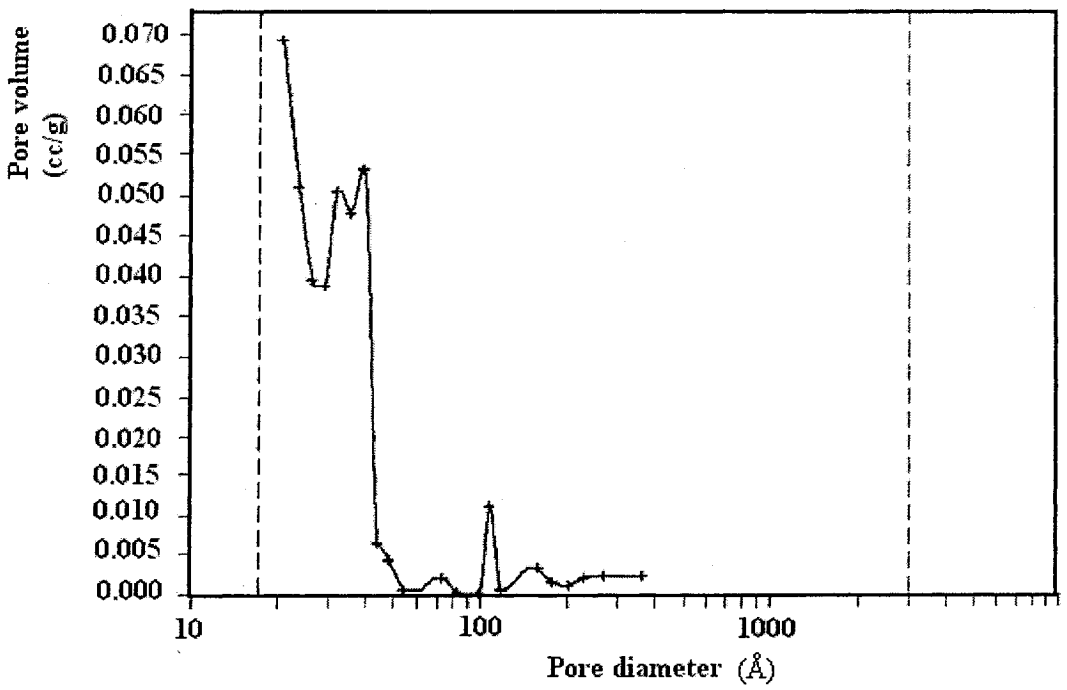

Figure 4.9 dV/dlog(D) desorption pore volume plot of parent CaA zeolite at 250°C

4.2 Preparation of the "acidic" silica nanoboxes (m)H-dealX

The "acidic" silica nanoboxes ((m)H-dealX) were produced by ion exchange of dealuminated NaX with ammonium chloride followed by temperature-programmed calcination (TPC) treatments. This is to test the materials under normal conditions of a catalytic reaction as well as their thermal and chemical stability, since the protons in the structure can damage the network when activated at high temperature.

4.2.1 Ion exchange

In the structure of the Na-dealX sample, there are still some Na^+ ions trapped as counter-ions to balance the negative charges of Al atoms since not all Al are removed. The pores of Na-dealX are sufficiently large to allow a variety of ions to exchange with sodium ions in the cavity. Materials showing acidic catalytic properties are hydrogen zeolites that are produced by an ion exchange with NH_4^+, followed by calcination treatment to create the protonic acid sites (Brönsted acid sites).

When the zeolite was immersed in an aqueous NH_4Cl electrolyte, the Na^+ communicated with NH_4Cl solution, resulting in an exchange of ions between the solid phase and the solution. Since the rate of exchange increases with rising temperature, we decided to perform the ion exchange of Na-dealX with 5wt% of NH_4Cl solution at 80°C in water bath to make sure that the exchange reaction goes to completion. The results were shown in Table 4.4, where (m)Na-dealX has monomodal pore size distribution, *i.e.* all pores in structure are mesopores; (b)Na-dealX has bimodal, *i.e.* both micropores and mesopores are present in the pore system. As we can see, (m)Na-dealX and (m)NH_4-dealX have quite similar textural prosperities; yet (m)NH_4-dealX has appreciably larger

pore volume and pore diameter. This is probably due to the fact upon ions exchange between solid (m)Na-dealX and NH_4Cl solution, some SiO_4 debris trapped in the cavities can be further dissolved in the solution. They are removed from the mesopores along with the NH_4Cl solution. A very clear evidence for this is seen when the (m)H-dealX (activated form of (m)NH_4-dealX) exhibited higher surface area and larger pore diameter and pore volume than those of activated (m)Na-dealX (both samples were activated to 600°C using TPC). On the other hand, in (b)Na-dealX, both micropores (ca.133 $m^2 g^{-1}$) and mesopores (ca. 282 $m^2 g^{-1}$) are present in the pore system after dealumination of NaX with AHFS as shown in Table 4.4. A quite high amount of micropores present in the structure is probably because the dealuminated reaction did not go to completion. It has been reported that the structure of the ammonium form of the parent X zeolite normally starts to rapidly decompose at ca. 100°C [55]. In the same way, when the (b)NH_4-dealX sample (Table 4.4) is heated at 250°C, some remaining micropores collapse by "proton" attack [62], leading to a decrease in the specific surface area by 120 m^2g^{-1}.

4.2.2 Activation

More attention needs to be considered to avoid undesired effects in the calcination process, such as the dealumination of the framework by water vapors, which is already present in the solid or being generated during the combustion. Hence, all the ammonium zeolite prior to thermal decomposition of the NH_4^+ ion need to be placed in the oven overnight in order to remove all adsorbed water. Moreover, Temperature Programmed Calcination (TPC) procedure is recommended. From Table 4.4, the (m)H-dealX obtained from method A (TPC procedure) to 600°C has higher BET surface area and smaller pore

opening than those obtained from method D (Direct Heating to 600°C). In the TPC method, a gradual increase in temperature (at a ramp of around 1°C/min) after 300°C is applied to prevent the mass decomposition of ammonium ions into protons which can lead to some structural collapse. It is believed that these H^+ ions can cause dehydroxylation at high temperature resulting in various effects such as siloxane bond hydrolysis and/or dealumination as shown in Figure 4.9b. Conversely, the activation procedure does not affect the periodicity of nanosized cavities because samples activated from both methods, A (TPC) and D (DH) in Table 4.4 display similar X-ray diffraction patterns as shown in Figure 4.12A. Therefore, (m)H-dealX may also be achieved by direct calcination if some losses of surface area and volume can be neglected. The benefit is more energy saving since heating duration decreases from 27 hours from TPC to 6 hours in DH.

Nonetheless, in the purpose of preparing highest quality of nonstructural materials-(m)H-dealX and deal-CaA, the TPC procedure is therefore used in this project.

In conclusion, (m)H-dealX material is prepared from dealumination of NaX zeolite (totally mesoporous), ion-exchange and temperature programmed calcination; there is almost no change in terms of pore size distribution in (m)H-dealX with respect to the (m)Na-deal X (Figure 4.6 and 4.7).

Table 4.4 Nitrogen adsorption/desorption isotherms of some NaX zeolite-derived mesoporous materials investigated in this work

Sample	S_{BET} $m^2 g^{-1}$	S_{cum} $m^2 g^{-1}$	S_{mic} $m^2 g^{-1}$	D_{av} nm	D^{op} nm	V_t $m^3 g^{-1}$	V_{mes} $m^3 g^{-1}$	V_{mic} $m^3 g^{-1}$	V_{mac} $m^3 g^{-1}$
NaX parent	740	22	696	0.8	0.8	0.31	0.03	0.28	0.00
(m)Na-dealX 250°C	451	509	0	4.6	4.0	0.54	0.53	0.00	0.01
(m)Na-dealX 600°C	252	321	0	4.7	4.0	0.38	0.37	0.00	0.01
(m)NH_4-dealX 250°C	443	528	0	4.7	4.1	0.57	0.52	0.00	0.05
A (m)H-dealX 600°C	328	419	0	4.5	3.9	0.43	0.4	0.00	0.03
D (m)H-dealX 600°C	281	399	0	4.9	4.2	0.44	0.41	0.00	0.03
(b)Na-dealX 250°C [(a)]	363	282	133	5.4	5.0	0.38	0.33	0.05	0.00
(b)NH_4-dealX 250°C [(a)]	234	252	45	6.9	6.2	0.39	0.36	0.02	0.01

[(a)] Sample and data from Dr. Thanh Vu (permission)
A- TPC procedure (Temperature-Programmed calcination)
D- DH procedure (Direct Heating)

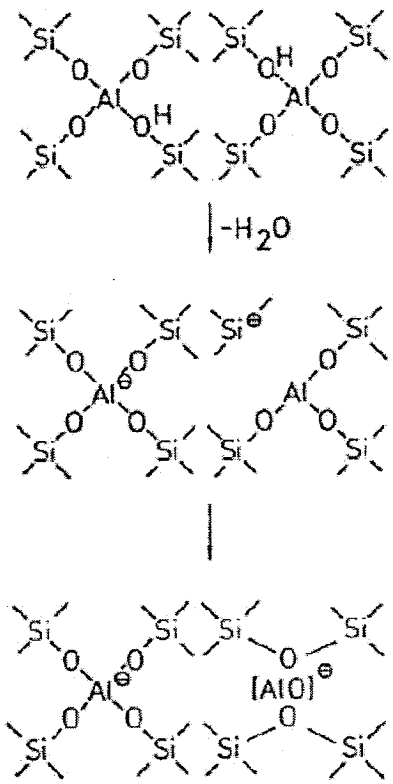

Figure 4.9b Schematic representation of dehydroxylation of a hydrogen zeolite [56]

4.3 Characterization of the nanostructured materials obtained: silica nanoboxes

4.3.1 Homogeneous distribution of the nanometric cavities

X-ray powder diffraction at 2θ between 5° and 60° shows that the original crystallinity of the parent NaX and CaA zeolites almost completely disappeared upon AHFS treatment (Figure 4.10 and Figure 4.11). Thus, the (m)H-dealX material with Si/Al ratio of 3.9 (Table 4.5) was absolutely amorphous from XRD result in Figure 4.10(c). However, a new peak at 2θ of around 1.26 degrees (corresponding to a d-space of less than 7nm) was clearly identified in (m)H-dealX material through XRD at small angles (Figure 4.12A). Figure 4.12B confirms that it is a true diffraction and not an optical artifact which is due to the slits using sample and holder under highly collimated slit arrangement of 0.1 degree. This means that the new materials have a framework with a high periodicity in nano-sized cavities. This recalls the diffraction pattern of MCM-41 [57] whose pure silica form exhibited a very strong reflection at 3.62nm and very weak reflections at 2.12, 1.86 and 1.41nm. However, with the increase in the aluminum content in the material, the main intense peak shifted towards higher d-spacing. Moreover, the main peak became broader and less intense, suggesting a poorly crystalline nature of the material. The weak reflections became much weaker and were not seen in the case of the MCM-41 with Si/Al ratio closes to 2 [57], which was very similar to the (m)H-dealX sample.

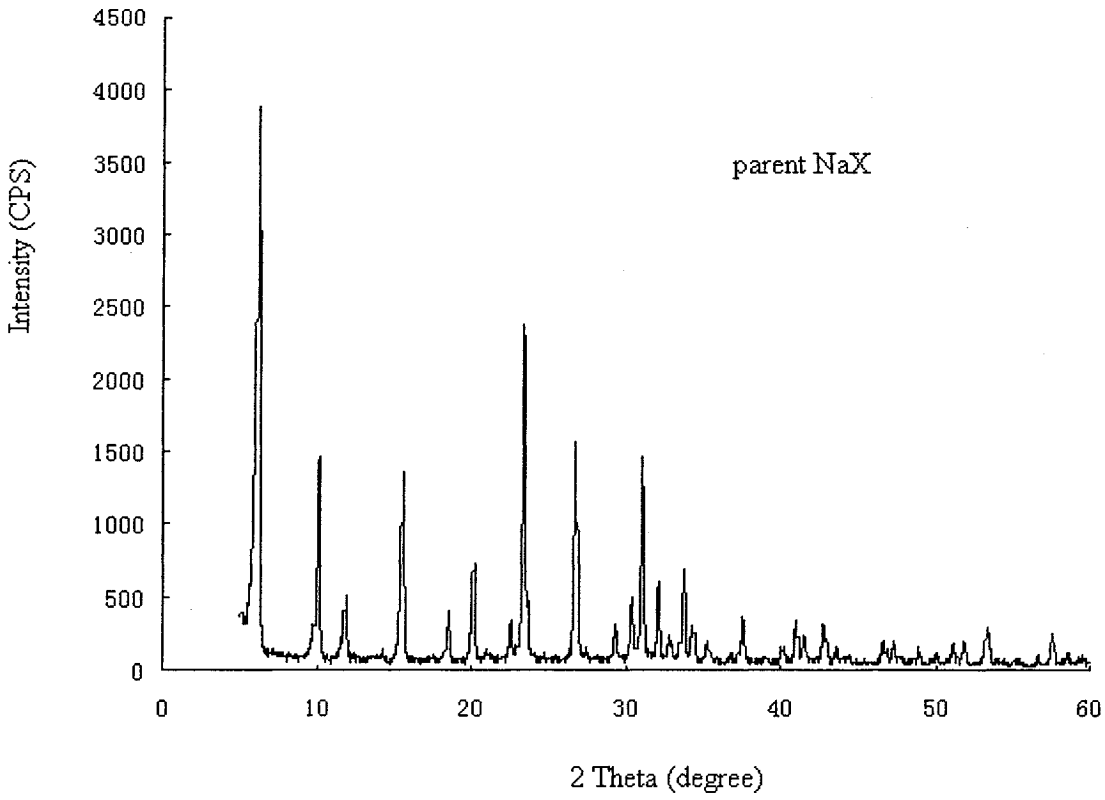

Figure 4.10 (a) X-ray diffraction patterns of parent NaX zeolite,

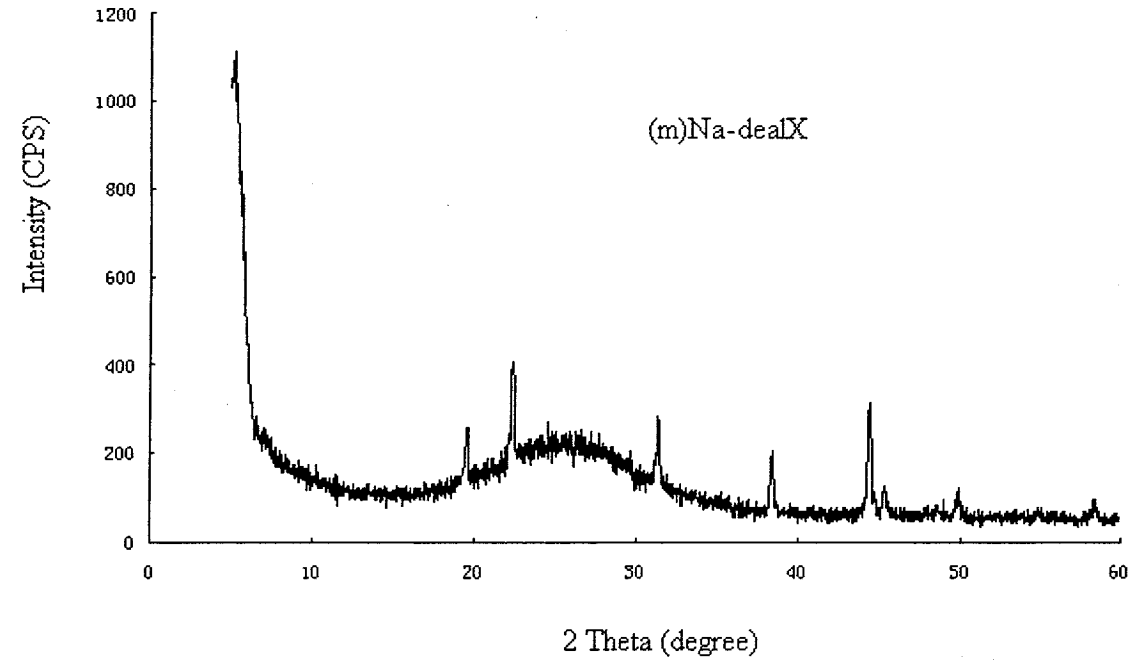

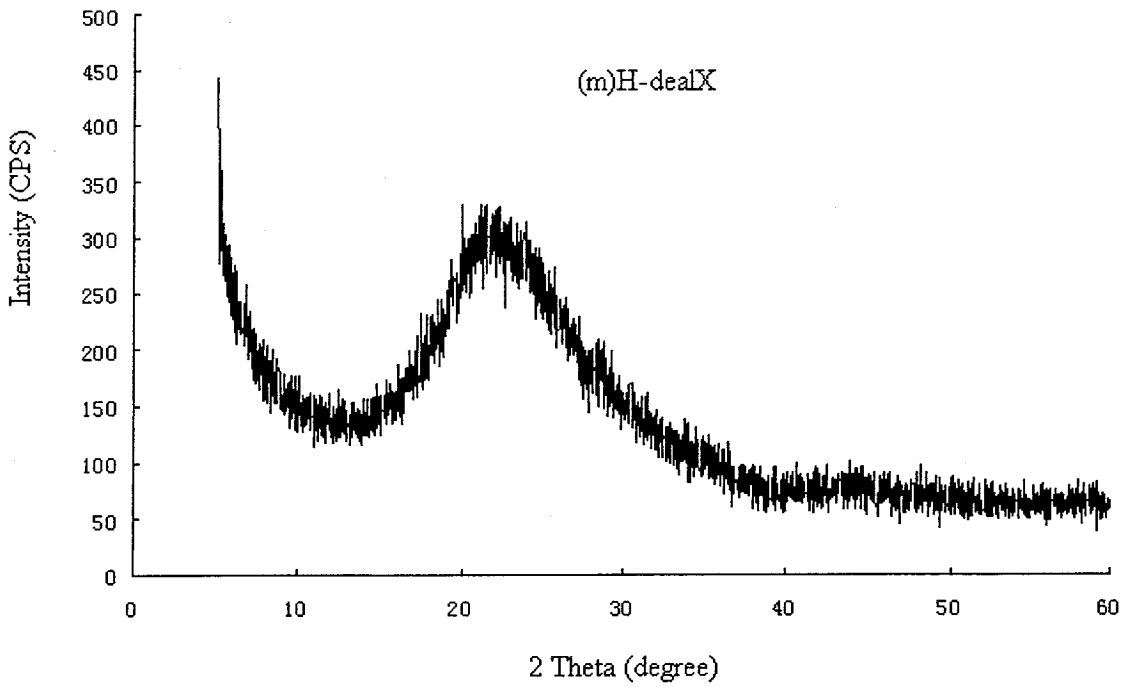

Figure 4.10 (b), (c) X-ray diffraction patterns of (m)Na-dealX and (m)H-dealX

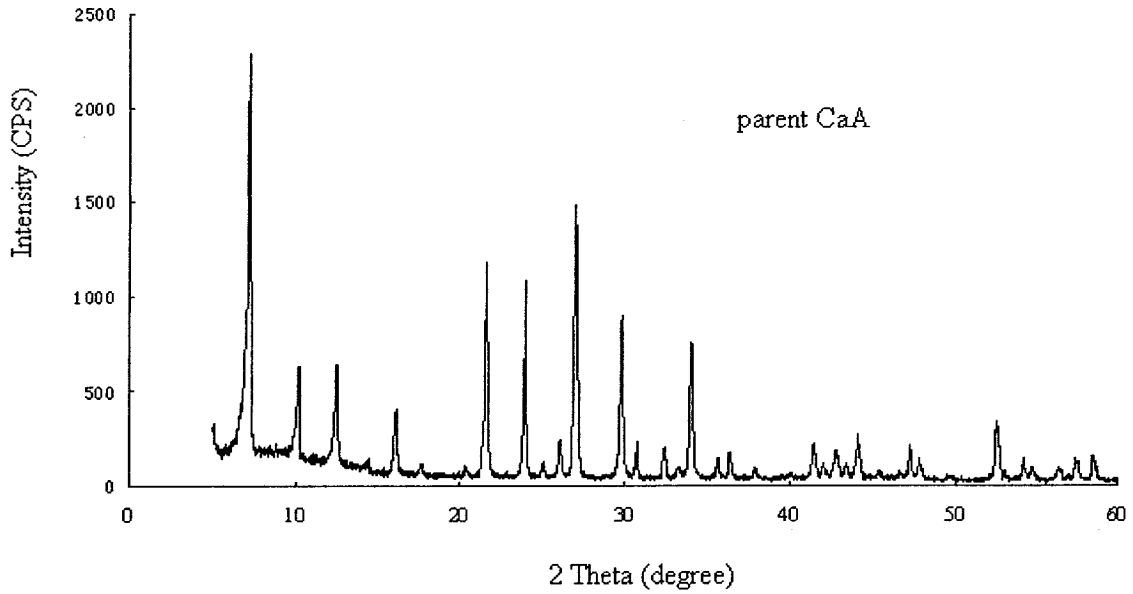

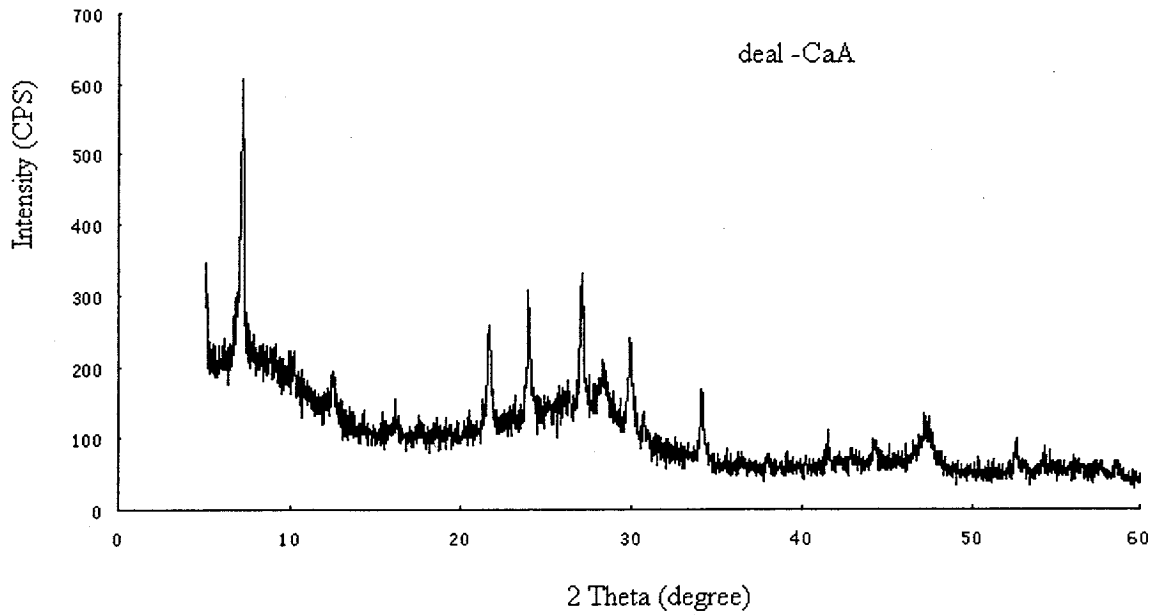

Figure 4.11 X-ray diffraction patterns of parent CaA zeolite and mesoporous deal-CaA

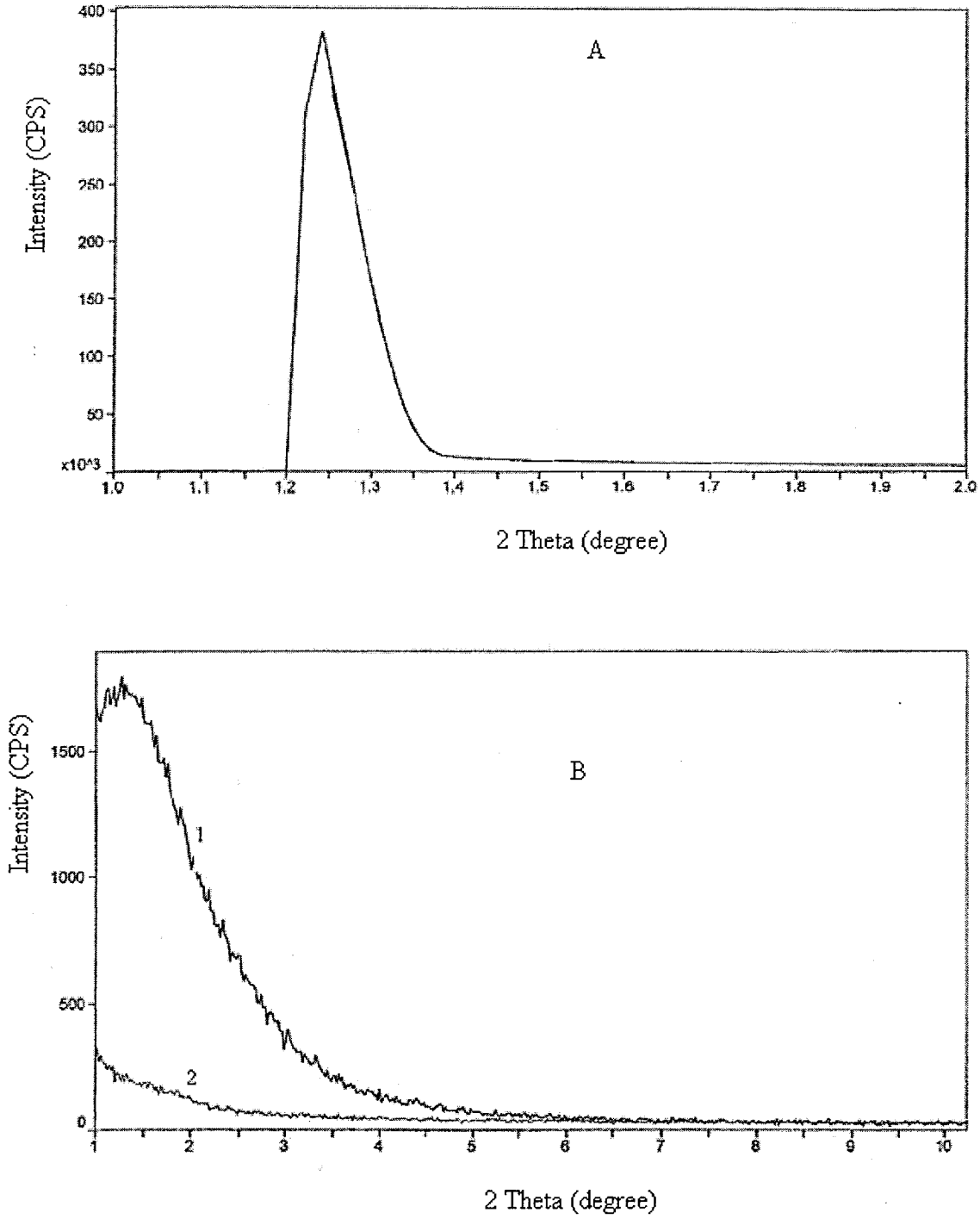

Figure 4.12 X-ray diffraction at low angle of the (m)H-dealX sample(A=diffraction under normal (1°) collimation slit arrangement; B=diffraction under highly collimated slit arrangement (0.1°):1=sample, 2=zero-background holder)

4.3.2 Shape of the nanometric cavities

The definition of the average pore size in a mesoporous material is based on the assumption that all pores are cylindrically shaped. Similarly, we have to consider the pore shape in our new mesoporous material prior to the determination of the pore opening. According to De Boer [27], based on the shape of sorption isotherms (*i.e.* hysteresis loop) in a mesoporous solid, one can outline the pore shapes. As previously mentioned, a hysteresis loop is created by the fact that evaporation (desorption) usually takes place at a pressure lower than that of capillary condensation (adsorption) from mesopores. The shape of a hysteresis loop is determined by the difference in behavior of adsorption and desorption. This difference stems from the value of $\cos\theta$ [26] and also the shape of the pores if capillary condensation is considered. The equation that is normally used is the Kelvin equation, which states that a liquid drop of radius r is proportional to the partial pressure of a vapor in equilibrium [25, 26].

The sorption isotherms of (m)Na-dealX and deal-CaA show important hysteresis loops (Figure 4.13 and Figure 4.14). This is indicative that the samples are mostly mesoporous materials because capillary condensation only takes place in the mesopores resulting in rapid increase in nitrogen volume adsorbed. In contrast, the adsorption/desorption isotherms of the parents NaX and CaA zeolites do not show any hysteresis loop because they contain only micropores; and capillary condensation is unable to occur in the micropore region, even in the region of relatively high relative pressure. This suggests that there is no apparent effect of (nitrogen) interparticle uptake or desorption. Since the dealuminated samples ((m)Na-dealX and deal-CaA) exhibited the same particles sizes as their corresponding parent zeolites, the hysteresis loops

reported in Figure 4.13 and Figure 4.14 for theses dealuminated materials could be correctly ascribed to intracrystalline sorption phenomena.

Since the adsorption isotherms of dealuminated silica nanoboxes have the shape of type IV isotherm and their hysteresis loops are of type E loop, it is assumed that the shape of their pores is that of an ink-bottle (Figure 4.15A) or spheroidal cavity (Figure 4.15B) [27a, 25]. In these cases, the pore opening can be derived from the nitrogen adsorbed and desorbed volumes since only desorption procedure is affected by the narrow pore mouth which results in a hysteresis loop.

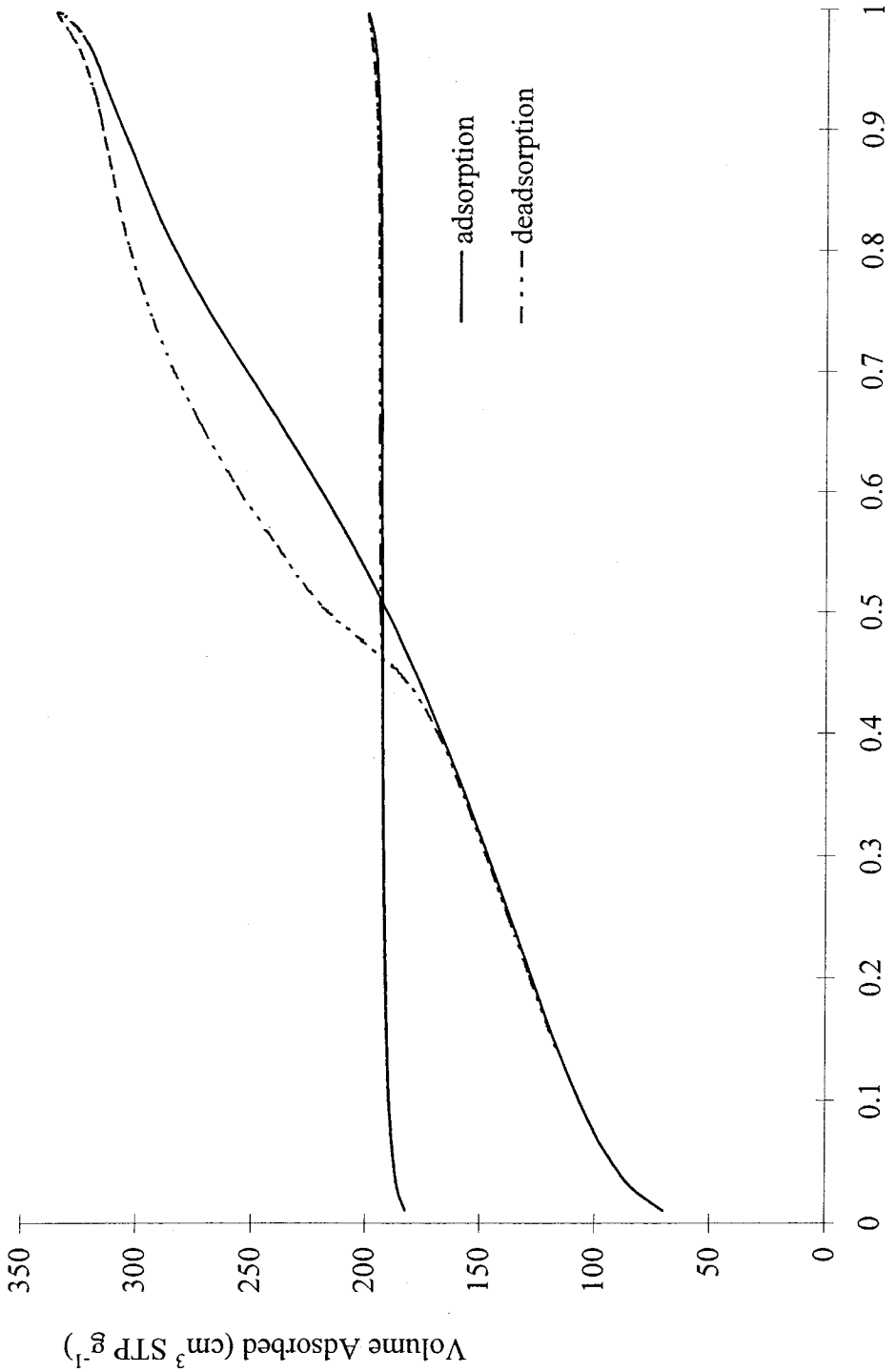

Figure 4.13 Nitrogen adsorption and desorption isotherms of (m)Na-dealX and parent NaX zeolite

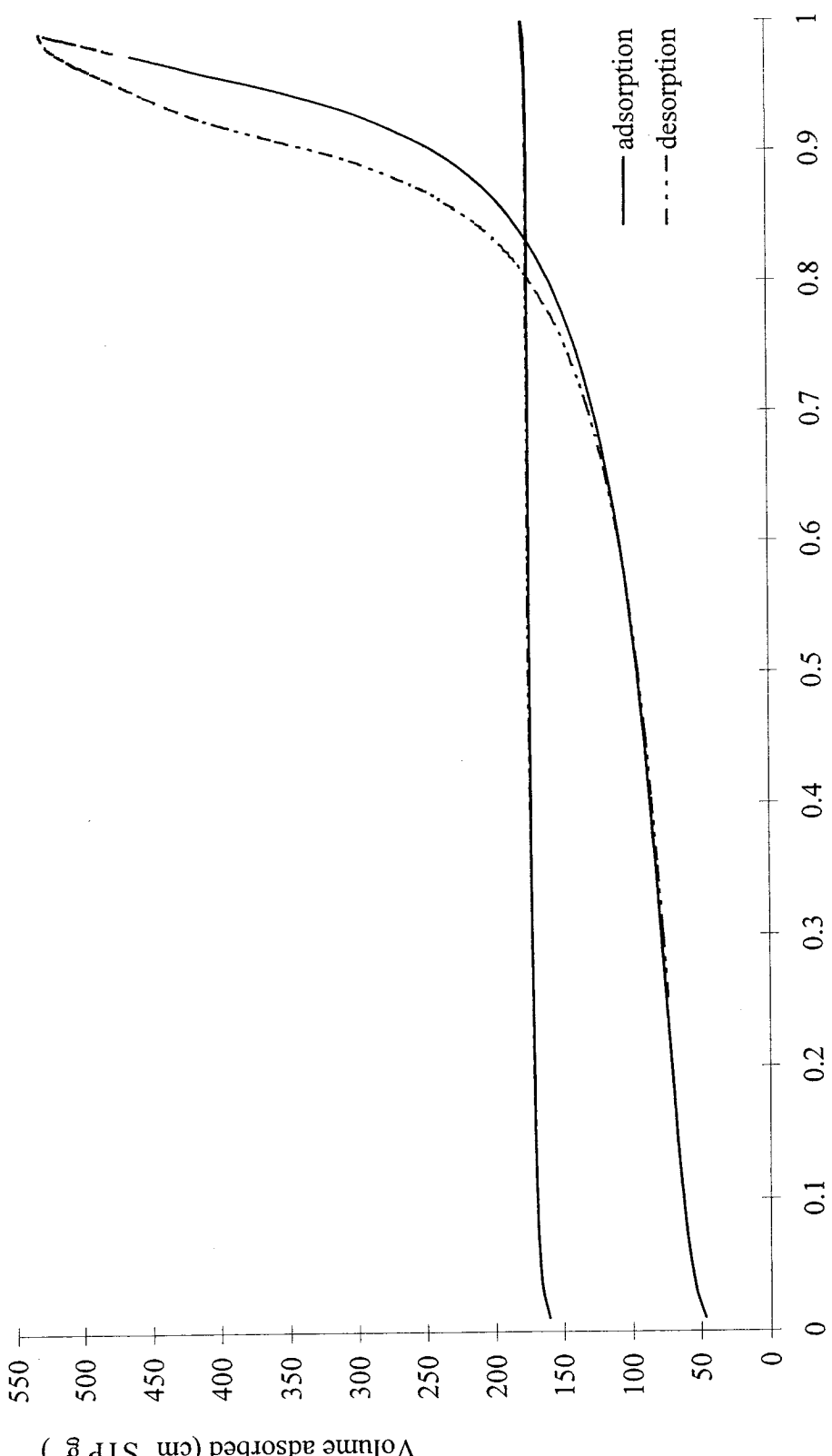

Figure 4.14 Nitrogen adsorption and desorption isotherms of deal-CaA and parent CaA zeolite

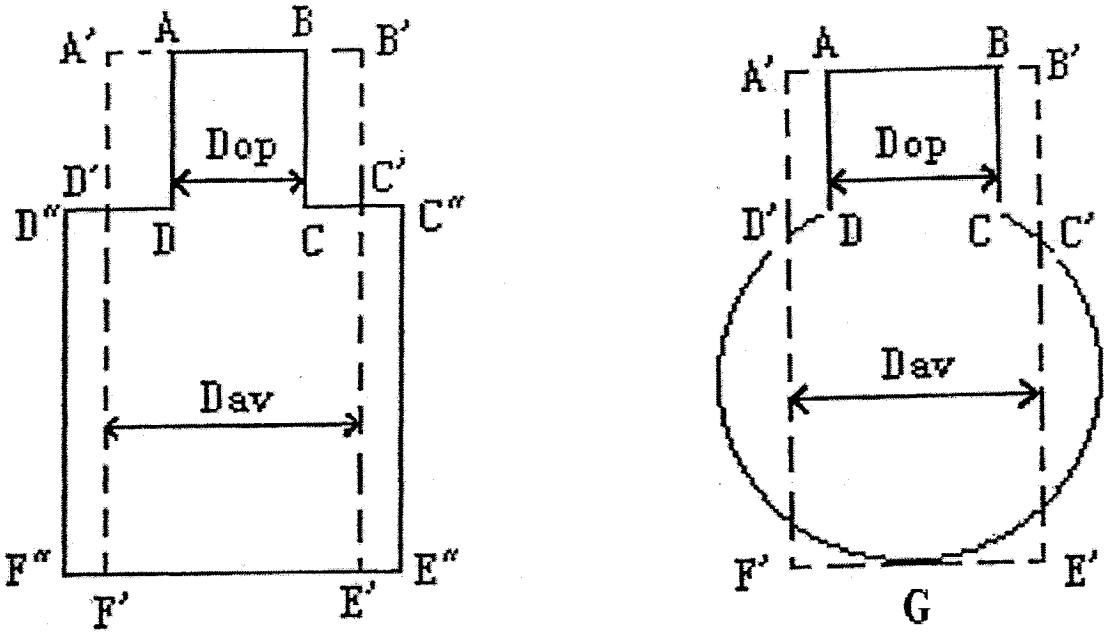

Figure 4.15 The possible shapes of nanometric cavities

4.3.3 Determination of the size of the nanocavity opening

In the mesopore region, the relative pressures for both adsorption and desorption isotherms are relatively high approaching to 1 (in practice, 0.98) so that cosθ can be assumed equal to 1 (high wetness of the pore walls) [58]. Thus, in that case, the adsorption isotherm is less affected by the shape of the pores than the corresponding desorption branch. This allows us to argue that the average value of the pore size determined using the adsorption isotherm is closer to the real value than that determined using the desorption isotherm. Indeed, because of the influence of the pore shape, there

is always some delay in the desorption process resulting thus in narrower calculated pore size (average), *i.e.*:

$D_{av}^{ads} > D_{av}^{des}$ (average pore diameters in the adsorption and desorption phases, respectively).

Figures 4.15A and Figures 4.15B show that in the desorption phase: only the nitrogen molecules in the volume ABCD in both shapes is effectively desorbed, i.e.

V_{ABCD} = Vrl (cylinder having a diameter equal to the pore opening)

If there were no significant change between the pore shape and the pore opening, i.e. the pore was perfectly cylindrical with the pore diameter equal to the calculated value of the average pore diameter; the volume would be calculated as follows:

$V_{A'B'C'D'} = V_l$ (cylinder having a diameter equal to the average pore size).

This situation can be assumed as that of the adsorption over the calculated value of the average pores diameter, as mentioned earlier.

It is obvious that the two cylinders (ABCD and A'B'C'D') have the same height of l.

In the two Figures 4.15A and 4.15B, the following volumes are equal to each other:

(ABCC''E''F''D''DA) (Bottle) = (A'B'E'F'A') (Cylinder)

(ABCC'GD'DA) (Spheroid) = (A'B'E'F'A') (Cylinder)

Therefore, V_{rl} and V_l can be experimentally determined using the desorption and adsorption isotherms, respectively. The levels CC'C'' D D'D" and CC'DD' in both pore

configurations correspond to the levels of adsorption or desorption change from the larger pore diameter to the value of average pore size (desorption phase) or vice-versa (adsorption phase). Knowing the value of the average pore size allows the determination of V_{rl} and V_l (cumulative volume of desorption and adsorption, respectively) using the tables of BET results for adsorption and desorption, respectively.

Since, Vrl = $[\pi (D_{av}{}^{op})^2]/4$ x 1 and V_l = $[\pi (D_{av}{}^{ads})^2]/4$ x 1, we finally have:

$$(D_{av}{}^{op})^2/(D_{av}{}^{ads})^2 = V_{rl} / V_l \quad \text{or} \quad (D_{av}{}^{op}) = (D_{av}{}^{ads}) \times (V_{rl} / V_l)^{1/2}$$

Thus, it is possible to calculate the diameter of the pore opening, $D_{av}{}^{op}$ or simply: D^{op}.

Since the shape of (m)H-deal-X hysteresis loop is similar to that of (m)Na-dealX material except for the volume of the nitrogen adsorbed as shown in Figure 4.16, its pore opening can also be calculated using the same method as previously described (m)Na-dealX (calculated values reported in Table 4.4 and 4.7 to 4.12).

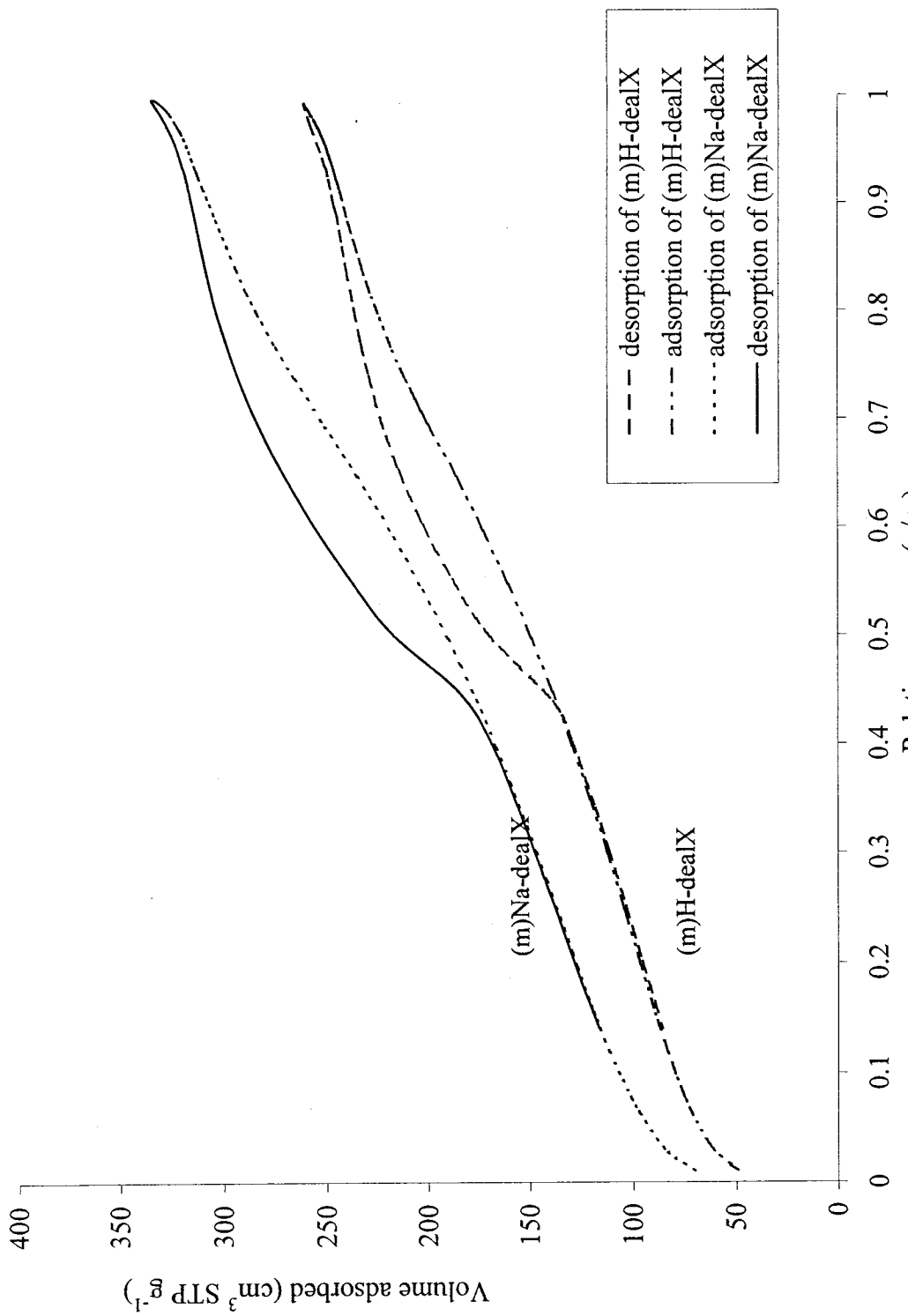

Figure 4.16 Nitrogen adsorption and desorption isotherms of (m)H-dealX and (m)Na-dealX

4.3.4 The Si-Al walls of the nanocavities

By using the Magic Angle Spinning (MAS) technique, high-resolution NMR spectra of solids are obtained. ^{27}Al MAS NMR spectra provide information on the configuration of aluminum, *i.e.*, tetrahedral coordination (AlO_4) or octahedral coordination (AlO_6). On the other hand, ^{29}Si MAS NMR spectra can show the local environment of SiO_4 tetraherdra, i.e. the number of Al neighbors of Si which are linked to it through –O- bonds, usually denoted Si(nAl). Each type of Si(nAl) unit (n=0,1,2,3 or 4) yields ^{29}Si MAS NMR signal in a well defined range of chemical shifts. These ranges are summarized for the various silicon units in Figure 4.17. The Si/Al ratio of zeolites can also be estimated using the peaks intensities.

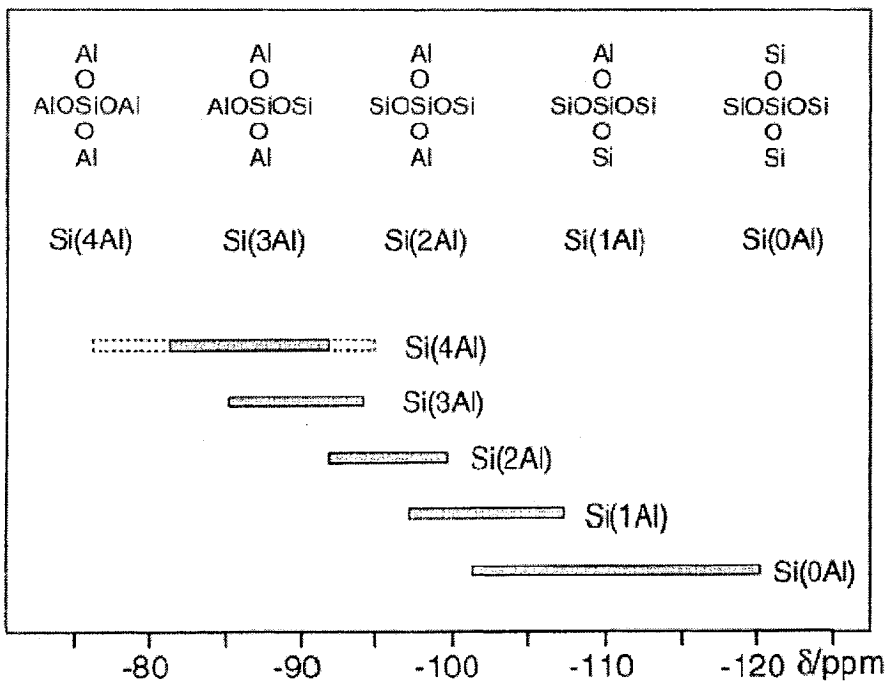

Figure 4.17 ^{29}Si chemical shifts of Si(nAl) units in zeolite frameworks. The dotted lines for Si(4Al) designated the chemical shift range observed for 1:1 aluminosilicate sodalites with different cage fillings [14c]

The ^{27}Al MAS NMR spectra of parent NaX and (m)H-dealX are shown in Figure 4.18. The parent NaX zeolite (*top*) shows a single narrow line with a chemical shift of about 60ppm caused by a single tetrahedrally coordinated aluminum, namely AlO_4, which exists in the zeolite framework. However, a broader peak and a small shoulder are observed in (m)H-dealX sample (*bottom*). One chemical shift at about 51ppm for the peak and at 3.71ppm for the shoulder, which are assigned to distorted tetrahedral coordination of aluminum (framework aluminum) and distorted octahedral coordination of aluminum (AlO_6) (non-framework aluminum species), are observed. Both of chemical shifts deviate more or less from the reference (60ppm and 0ppm) because of the distortions of the octahedral symmetry of AlO_6 units and the tetrahedral symmetry of AlO_4 when non-framework aluminum exists as polymeric aluminum oxide or oxide hydrates in zeolite cages or channels [59]. The non-framework aluminum species (AlO_6) are originated from the calcination of samples at 600°C.

From the ^{29}Si MAS NMR spectrum of NaX zeolite in Figure 4.19 (*top*), there are up to 5 well separated peaks at –86.26ppm, -90.68ppm, -95.58ppm, -100.48ppm and –104.48ppm (each peak represents a different environment for a Si atom, depending on the number of Al atoms directly surrounded it) are observed, which can be assigned to Si(4Al), Si(3Al), Si(2Al), Si(1Al), Si(0Al), respectively. Their intensities are found to decrease also in such order. Generally, it tells us a high aluminum content found in the parent NaX. In fact, the Si/Al atom ratio of the framework can be calculated directly from the ^{29}Si MAS NMR spectra using the relative intensities of the Si(nAl) peaks ($I_{Si\text{-}nAl}$) because each Al atom is surrounded by 4 Si atoms according to Löwenstein's rule, while the Si atoms can be surrounded by up to four Al atoms. Using the following equation we

calculated that the Si/Al ratio is about 1.3, which is close to the value of 1.2 determined by the AAS technique.

$$Si/Al = \frac{\sum_{n=0}^{4} I_{Si(nAl)}}{\sum_{n=0}^{4} 0.25 * n * I_{Si(nAl)}}.$$

On the other hand, in the (m)H-dealX spectrum (Figure 4.19 *bottom*), a broad peak at -109.67ppm is assigned to Si(0Al) environment. Also, several bumps, which can be assigned to the amount of Si(3Al), Si(2Al), Si(1Al), are also observed. Another small peak at around -40ppm might be the Si atom connected to a seriously distorted tetrahedral coordinated AlO_4. This evidence the gradual removal of the aluminum atoms in the dealumination process to produce (m)H-dealX from NaX leading to the disappearance of the signals of Si(4Al) units, and an increase in peaks intensities in the reverse order compared to the parent NaX zeolite. The calculated Si/Al atom ratio from the intensity is about 3.5, which is quite close to that determined by the AAS technique (Si/Al=3.9). Therefore, a higher Si/Al atom ratio is the primary reason for the higher thermal stability of the silica nanoboxes material. The Si/Al atom ratios in different samples associated with NaX are listed in Table 4.5. Moreover, the two ^{29}Si NMR spectra are similar to those reported in the corresponding Si/Al ratio range [60].

Table 4.5 The Si/Al ratios of NaX-related samples

Sample	Si/Al
NaX	1.2
(m)Na-dealX	3.2
(m)H-dealX	3.9

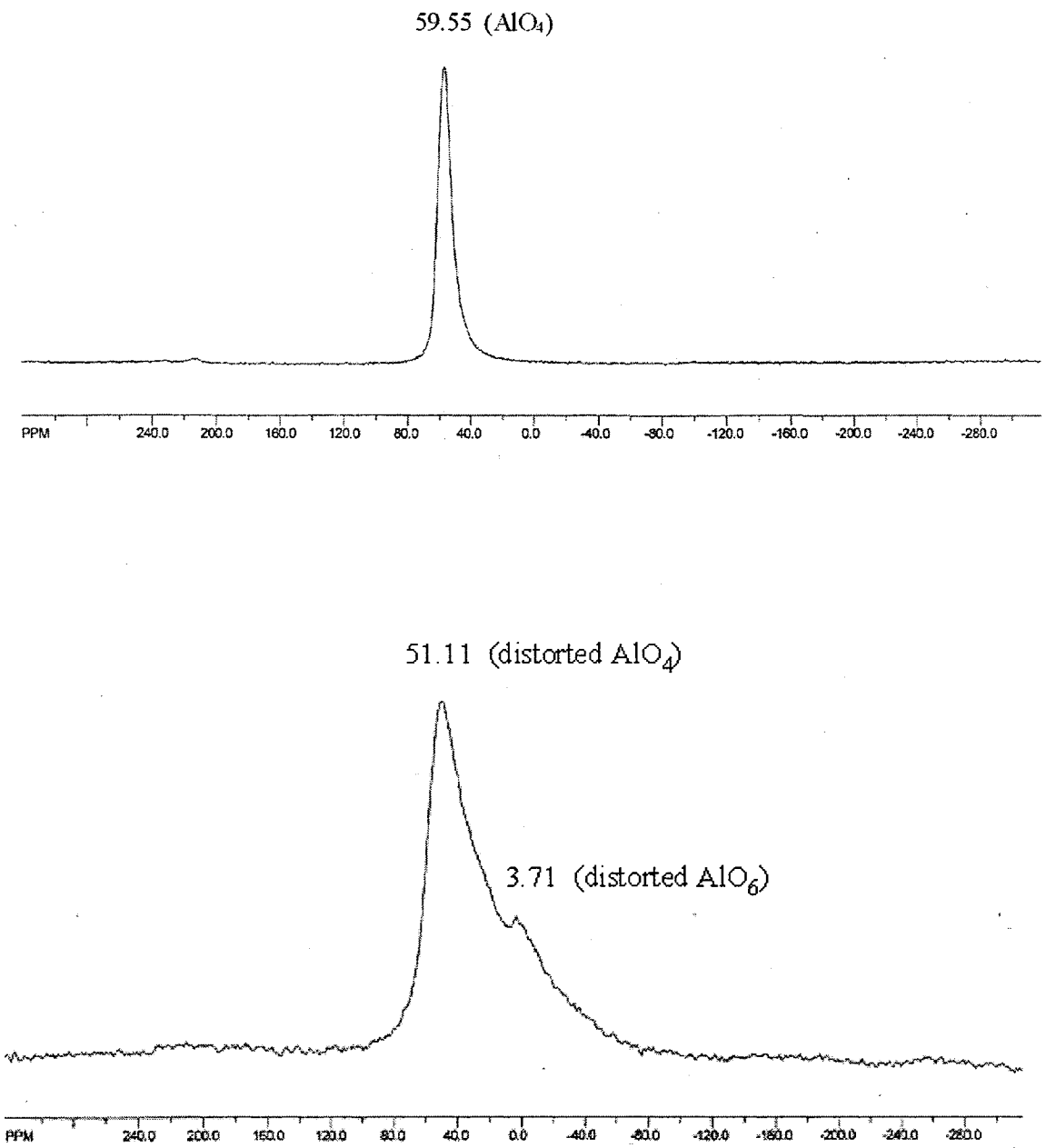

Figure 4.18 ^{27}Al MAS NMR spectra of NaX zeolite (*top*) and (m) H-dealX (*bottom*)

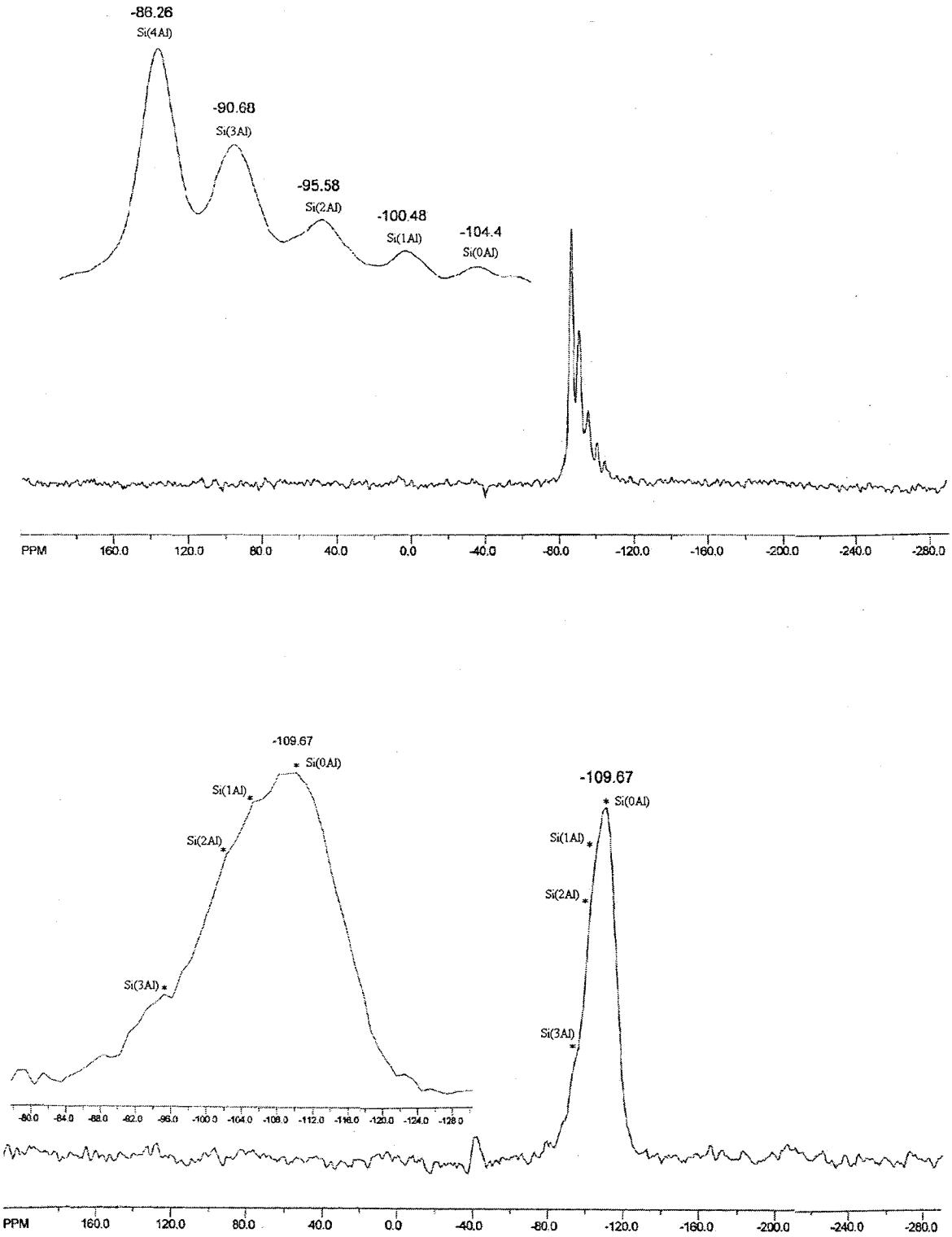

Figure 4.19 ^{29}Si MAS NMR spectra of NaX zeolite (*top*) and (m) H-dealX (*bottom*)

4.4 Thermal and hydrothermal stability of the nanoboxes

The thermal stability of H-dealX is found to depend on the extent of the removal of Al atoms from NaX. In fact, two types of dealuminated NaX materials are obtained: one has monomodal pore size distribution, *i.e.* all pores in the final structure are mesopores called (m)Na-dealX; another has bimodal, *i.e.* both micropores and mesopores are present in the pore system designated as (b)Na-dealX. (m)H-dealX from (m)Na-dealX is highly thermal resistant, whereas (b)H-dealX from (b)Na-dealX is not because pore occlusion occurs when the latter material is activated at high temperature. However, the existence of some micropores in the deal-CaA material does not seem to affect its thermal stability.

4.4.1 Thermal stability and hydrothermal stability of (m)H-dealX

TPC of the (m)Na-dealX and (m)NH_4-deal samples at 600°C results in some loss of surface area and sorption volume when compared to the untreated materials, respectively (Table 4.7). This is probably due to some SiO_4 debris still trapped inside the mesoporous cavities upon AHFS treatment and which had agglomerated to larger internal particles due to calcination, blocking thus some pores. However, the resulting (m)H-dealX activated at 600°C still shows quite high surface areas and large sorption volumes. This is very surprising because normally the structure of ammonia form of the parent X zeolite starts to rapidly decompose at around 100°C [55] indicating a high thermal instability. Therefore, the high thermal stability of the (m)H-dealX is due to its higher Si/Al ratio of 3.9 (Table 4.5) and its amorphous character. As mentioned earlier, the (m)H-dealX can also be achieved by DH (direct heating) calcination procedure which

results in some (minor) loss of surface area compared to that by TPC procedure as shown in Table 4.7.

Hydrothermal stability of extruded (m)H-dealX with 20wt% bentonite was tested at 500°C for 5 hours in presence of steam by injection of water, in the following conditions: weight space hourly velocity is 3.5$cm^3\ hr^{-1}$ with a nitrogen flow rate of 5$cm^3\ min^{-1}$. The results are shown on Table 4.6 [61].

Table 4.6 Hydrothermal stability of (m)H-dealX

Sample	S_{BET} $m^2 g^{-1}$	S_{cum} $m^2 g^{-1}$	S_{mic} $m^2 g^{-1}$	D_{av} (nm)	V_t $cm^3 g^{-1}$	V_{mes} $cm^3 g^{-1}$	V_{mic} $cm^3 g^{-1}$	V_{mac} $cm^3 g^{-1}$
Untreated Sample*	193	252	0	55.1	0.28	0.27	0.00	0.01
Treated Sample*	181	243	0	55.8	0.27	0.25	0.00	0.02
Treated Sample*	176	240	0	56.9	0.27	0.25	0.00	0.02

Sample* (m)H-deal X with 20wt% bentonite

From the results in Table 4.6, the "acidic" silica nanoboxes (m)H-dealX exhibit quite high hydrothermal stability because the material still have almost the same BET surface area as the untreated one after exposure to the steam for five hours at high temperature of 500°C.

4.4.2 Thermal stability of (b)H-dealX

Calcination of the "bimodal" (b)NH_4-dealX sample at 600°C results in very low BET surface area (8$m^2\ g^{-1}$) and sorption volume (0.02$cm^3\ g^{-1}$) (sample (b)H-dealX in Table 4.7). This is because the presence of the microporous zeolite component in (b)NH_4-dealX material. When (b)NH_4-dealX was heated rapidly to an elevated

temperature, the sudden decomposition of ammonium ions into protons provoked the collapse of the remaining micropores, leading to the extraction of large Al containing debris with the obvious consequence of a significant pore blocking (occlusion). In fact, micropores undergoes a rapid structural collapse due to "proton" attack [62] and the collapsed species agglomerate in the mesopores and migrate to the pore mouth resulting in serious mesopores occlusion. Nevertheless, thermal stability of bimodal nanoboxes can be improved by ion exchange with Cerium, Lanthanum, and Yttrium etc.

In conclusion, (m)H-dealX are highly thermally resistant compared to (b)H-dealX. This can be seen from the Table 4.7: (m)H-dealX (without any micropores) still has quite large surface area ($281 m^2 g^{-1}$) when calcined at 600°C compared to $8 m^2 g^{-1}$ in the (b)H-dealX sample. Therefore, to obtain highly thermally resistant silica nanoboxes, these materials should not contain any microporous remnant of the dealumination of the parent zeolite.

The general morphology and characterization of silica nanoboxes derived from NaX zeolite are represented in Table 4.7.

Table 4.7 Characterization of the NaX zeolite-derived mesoporous materials investigated in this work.

Sample	S_{BET} $m^2 g^{-1}$	S_{cum} $m^2 g^{-1}$	S_{mic} $m^2 g^{-1}$	Crystallinity Si/Al	D_{av} nm	D^{op} nm	V_t $cm^3 g^{-1}$	V_{mes} $cm^3 g^{-1}$	V_{mic} $cm^3 g^{-1}$	V_{mac} $cm^3 g^{-1}$
NaX parent	740	22	696	high(1.2)	0.8	0.8	0.31	0.03	0.28	0.00
(m)Na-dealX 250°C	451	509	0	Very low(*) (3.2)	4.6	4.0	0.54	0.53	0.00	0.01
(m)Na-dealX 600°C	252	321	0	amorphous(*)	4.7	4.0	0.38	0.37	0.00	0.01
(m)NH_4-dealX 250°C	443	528	0	amorphous(*)	4.7	4.1	0.57	0.52	0.00	0.05
A (m)H-dealX 600°C	328	419	0	amorphous(*) (3.9)	4.5	3.9	0.43	0.4	0.00	0.03
D (m)H-dealX 600°C	281	399	0	amorphous(*)	4.9	4.2	0.44	0.41	0.00	0.03
(m)H-dealX at 700°C	284	385	0	amorphous(*)	4.8	4.3	0.43	0.4	0.00	0.03
(b)Na-dealX 250°C[(a)]	363	282	133	n.a.	5.4	5.0	0.38	0.33	0.05	0.00
(b)NH_4-dealX 250°C [(a)]	234	252	45	n.a.	6.9	6.2	0.39	0.36	0.02	0.01
D (b)H-dealX 600°C [(a)]	8	8	0	n.a.	11.8	11.6	0.02	0.02	0.00	0.00

(*): Except for peak of X-ray powder diffraction at low angles.
n.a.= not available
[(a)] Sample and data from Dr. Thanh Vu (permission)
B- TPC procedure (Temperature-Programmed calcination)
D- DH procedure (Direct Heating)

4.4.3 Thermal stability of deal-CaA

The thermal stability of deal-CaA is shown in Table 4.8, where "A" stands for the TPC activation procedure. Unlike (b)H-dealX, the remaining micropores in deal-CaA material do not give rise to complete pore occlusion. This is probably due to the absence of protons, which prevents the phenomenon of proton attack on HO-Al bonds, thus minimizing pore occlusions. The general morphology and characterization of silica nanoboxes derived from CaA zeolite are represented in Table 4.8.

Table 4.8 Characterization of the CaA zeolite-derived mesoporous materials investigated in this work.

Sample	S_{BET} $m^2 g^{-1}$	S_{cum} $m^2 g^{-1}$	S_{mic} $m^2 g^{-1}$	Crystallinity Si/Al	D_{av} nm	D^{op} nm	V_t $cm^3 g^{-1}$	V_{mes} $cm^3 g^{-1}$	V_{mic} $cm^3 g^{-1}$	V_{mac} $cm^3 g^{-1}$
CaA parent	661	26	613.6	high (1.0)	0.5	0.5	0.27	0.02	0.25	0.00
deal-CaA 250°C	251	291	61.3	very low(*) (1.7)	15.1	14.5	0.8	0.77	0.03	0.01
A deal-CaA 600°C	215	236	27.7	amorphous	14.0	14.1	0.72	0.67	0.01	0.01

4.5 Chemical stability of the silica nanoboxes

The Chemical stability of (m)H-dealX and deal-CaA are assessed by deposition of sulfuric acid and triflic acid. Since (m)H-dealX exhibits a network of inkbottle shaped cavities, it is our intention to incorporate significant amounts of liquid acidic species (sulfuric acid and triflic acid) into these solid supports. This provides interesting acid catalysts with sufficiently large cavities to convert bulky molecules. The liquid surface of these acidic species could express catalytic properties as if it were a free liquid surface; thus these materials may be more advantageous than the simply supported catalysts in

some industrial reactions, such as the isobutane/olefin alkylation [63] or others catalytic reactions [64]. In addition, it would be easier to separate and recover the solid catalyst at the end of the reaction.

4.5.1 Incorporation techniques

Incorporations of liquid acidic species into the (m)H-dealX cavity by wet and dry impregnation techniques have been developed [64]. The resulting solid superacids exhibit different textural properties as listed on Table 4.9.

Table 4.9 Wet impregnation and dry impregnation technique

Sample	TFA loading (wt%)	S_{BET} $m^2 g^{-1}$	S_{cum} $m^2 g^{-1}$	S_{mic} $m^2 g^{-1}$	D_{av} nm	D^{op} nm	V_t $cm^3 g^{-1}$	V_{mes} $cm^3 g^{-1}$	V_{mic} $cm^3 g^{-1}$	V_{mac} $cm^3 g^{-1}$
Initial A		328	419	0	4.5	3.9	0.43	0.40	0.00	0.03
Wet I.T.	7.2	326	419	0	4.6	3.9	0.44	0.41	0.00	0.03
Dry I.T.	7.2	234	323	0	4.8	3.9	0.35	0.32	0.00	0.03
Initial B		347	423	0	4.4	3.7	0.42	0.38	0.00	0.04
Wet I.T.	10.0	264	330	0	4.4	3.7	0.33	0.31	0.00	0.02
Dry I.T.	10.0	188	265	0	4.5	3.7	0.27	0.26	0.00	0.01

Wet I.T.-wet impregnation technique.
Dry I.T.-dry impregnation technique.
Initial A-(m)H-dealX is (0)(m)H-dealX in Table 4.12.
Initial B-(20)(m)H-dealX in Table 4.12.

The results show that the dry impregnation technique is more aggressive and destroys more zeolite structure than the wet one. This may be because of the cumulative acidity when later additions of TFA solution into solid superacid are more corrosive (high concentration of liquid TFA) than original acid solution. Therefore, all solid superacids through the project were prepared by wet impregnation technique.

4.5.2 The amounts of deposited sulfuric acid and TFA

The deposited amount started with 15wt% sulfuric acid (Hammet acidity function H_0 = -12) and 7wt% TFA (H_0 = -14.1) into the (m)H-dealX. As we can see in Table 4.10, mesoporous sample (m)H-dealX allows a loading of sulfuric acid up to 20wt% and up to 24wt% of triflic acid while maintains quite decent surface areas and pore volumes. However, when 15wt% of TFA was deposited into calcined deal-CaA, the mesoporous material exhibits a quite large pore volume, yet very low surface area (ca. 100$m^2 g^{-1}$) (Table 4.11). This would significantly decrease the number of catalytic sites and catalytic properties of the material.

Table 4.10 Modification of the pore characteristics upon loading of sulfuric acid and triflic acid onto (m)H-dealX support

Sample	Acid	Acid loading (wt%)	S_{BET} $m^2 g^{-1}$	S_{cum} $m^2 g^{-1}$	S_{mic} $m^2 g^{-1}$	D_{av} nm	D^{op} nm	V_t $cm^3 g^{-1}$	V_{mes} $cm^3 g^{-1}$	V_{mic} $cm^3 g^{-1}$	V_{mac} $cm^3 g^{-1}$
(S15) (m)H-dealX	H_2SO_4	15	252	313	0	4.9	4.1	0.35	0.32	0.00	0.03
(S20) (m)H-dealX	H_2SO_4	20	236	293	0	4.9	4.1	0.32	0.30	0.00	0.02
(S25) (m)H-dealX	H_2SO_4	25	151	207	0	5.5	4.4	0.25	0.24	0.00	0.01
(T7) (m)H-dealX	CF_3SO_3H	7	327	419	0	4.6	4.0	0.44	0.41	0.00	0.03
(T10) (m)H-dealX	CF_3SO_3H	10	282	366	0	4.6	3.7	0.39	0.36	0.00	0.03
(T16) (m)H-dealX	CF_3SO_3H	16	244	336	0	4.6	3.9	0.36	0.33	0.00	0.03
(T24) (m)H-dealX	CF_3SO_3H	24	215	297	0	4.7	3.9	0.31	0.29	0.00	0.02
(T32) (m)H-dealX	CF_3SO_3H	32	101	155	0	5.2	4.2	0.18	0.17	0.00	0.01

Table 4.11 Modification of the pore characteristics upon loading of sulfuric acid and triflic acid onto deal-CaA support

Sample	TFA loading wt%	S_{BET} $m^2 g^{-1}$	S_{cum} $m^2 g^{-1}$	S_{mic} $m^2 g^{-1}$	D_{av} nm	D^{op} nm	V_t $cm^3 g^{-1}$	V_{mes} $cm^3 g^{-1}$	V_{mic} $cm^3 g^{-1}$	V_{mac} $cm^3 g^{-1}$
deal-CaA (600°C)	0	215	236	28	5.0	5.0	0.72	0.67	0.01	0.01
(T15) deal-CaA (600°C)	15	108	141	0	15.1	14.7	0.50	0.47	0.00	0.03
(T25) deal-CaA (600°C)	25	86	119	0	14.7	14.3	0.40	0.37	0.00	0.03
(T35) deall-CaA (600°C)	35	87	112	0	15	14.5	0.38	0.36	0.00	0.02

By using the DTA/TGA technique, it is possible to qualitatively assess the amounts of TFA in the liquid as well as in the bound phases [49]. As reference, the DTA/TGA analyses of the (m)H-dealX, which was heated to 600°C in argon with flow rate: $4cm^3min^{-1}$, is shown in Figure 4.21. There is no mass change, and the difference in heat is within the range of instrumental deviation (according to the manual, the baseline of DTA deviation should be less than ± 5 μV). This indicates that the materials are quite stable. However, in the case of the (T24)(m)H-dealX sample (24wt% TFA originally loaded), the TGA/DTA is performed at argon environment in order to avoid the decomposition of the TFA by the moisture in the air at the temperature range of 290°C to 320°C. The results are shown in Figure 4.22. As we can see there is some sorbed species (more than 4wt%) desorbed (see the sign of the corresponding DTA peak-endothermic

peak) at 200-220°C that could be easily attributed to the free TFA form (boiling point=161°C [65]). In the range of 280-340°C, other surface species (more than 15wt%) are assigned to the bound form of TFA. The TFA binds to the surface by Coulombic force through interaction of $CF_3SO_3^-$ and the protonic form of the zeolitic surface (Figure 4.24), since TFA is highly dissociated in aqueous solution. Due to the presence of hydroxyl groups (-OH) on the surface of (m)H-dealX or water from dehydration at high temperature (between 280-340°C), the bound TFA underwent a decomposition via two pathways as described by L. Fabes [48]. And a corresponding broad exothermic peak on the DTA curve at that temperature is clearly shown because of the formation of more stable products. The whole reaction process and reaction mechanisms are shown in Figure 4.24.

On the other hand, the (m)H-dealX material loaded with sulfuric acid does not show such clear distinction between surface species (Figure 4.23) because sulfuric acid reacted readily with Al atoms which are gradually removed from their locations as the temperature increased.

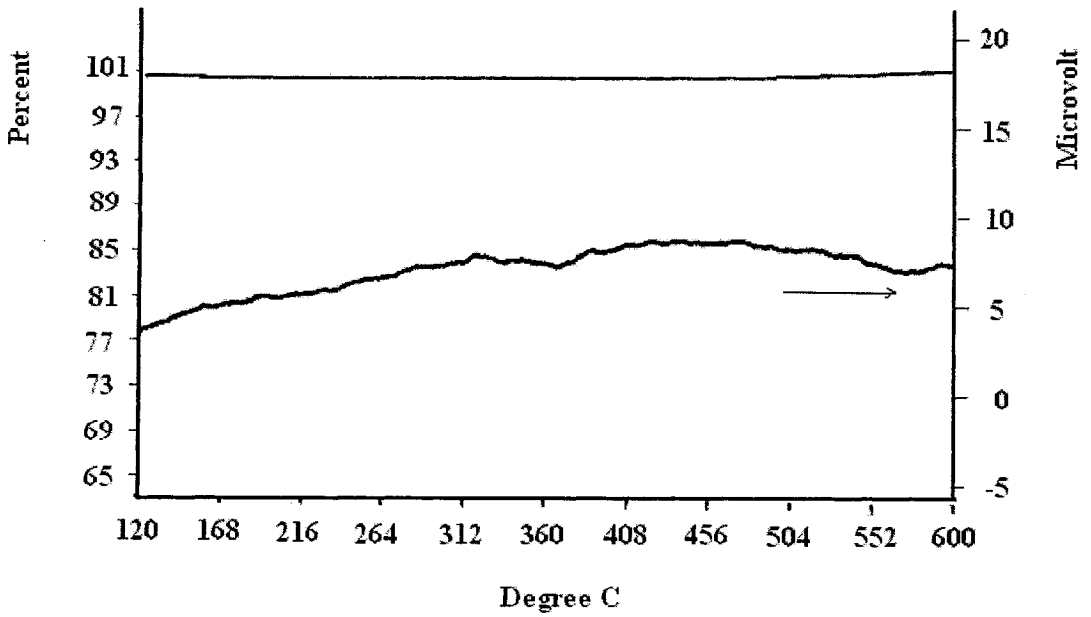

Figure 4.21 DTA / TGA analyses of (m)H-dealX in argon with flow rate: $4cm^3min^{-1}$.

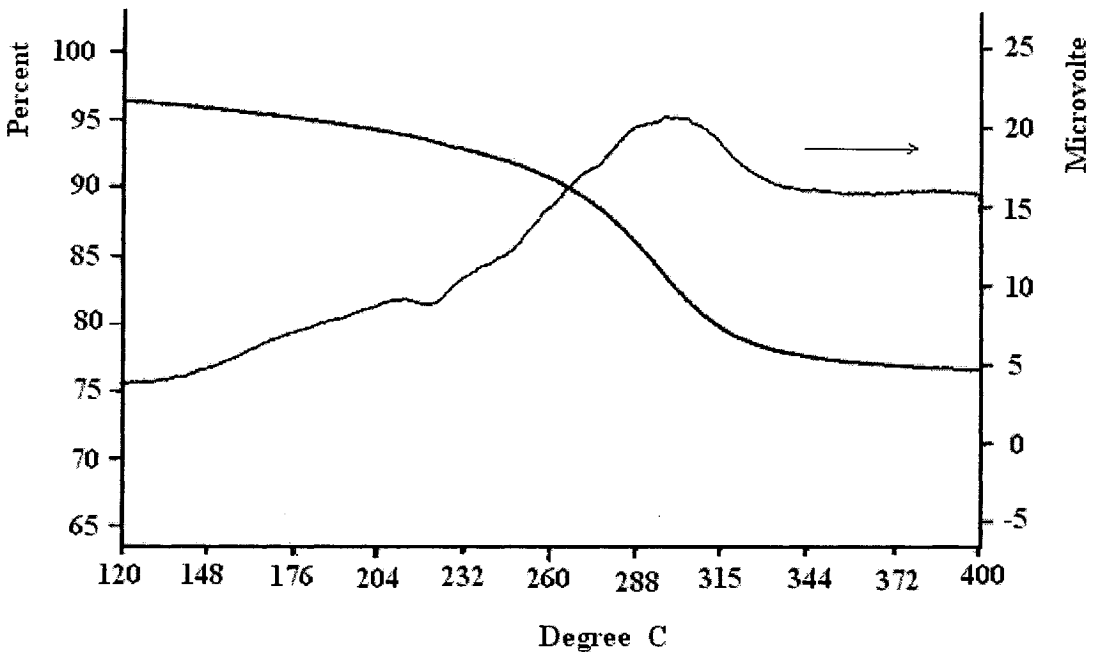

Figure 4.22 DTA / TGA analyses of (m)H-dealX incorporated with 24wt% TFA in argon with flow rate: $4cm^3min^{-1}$.

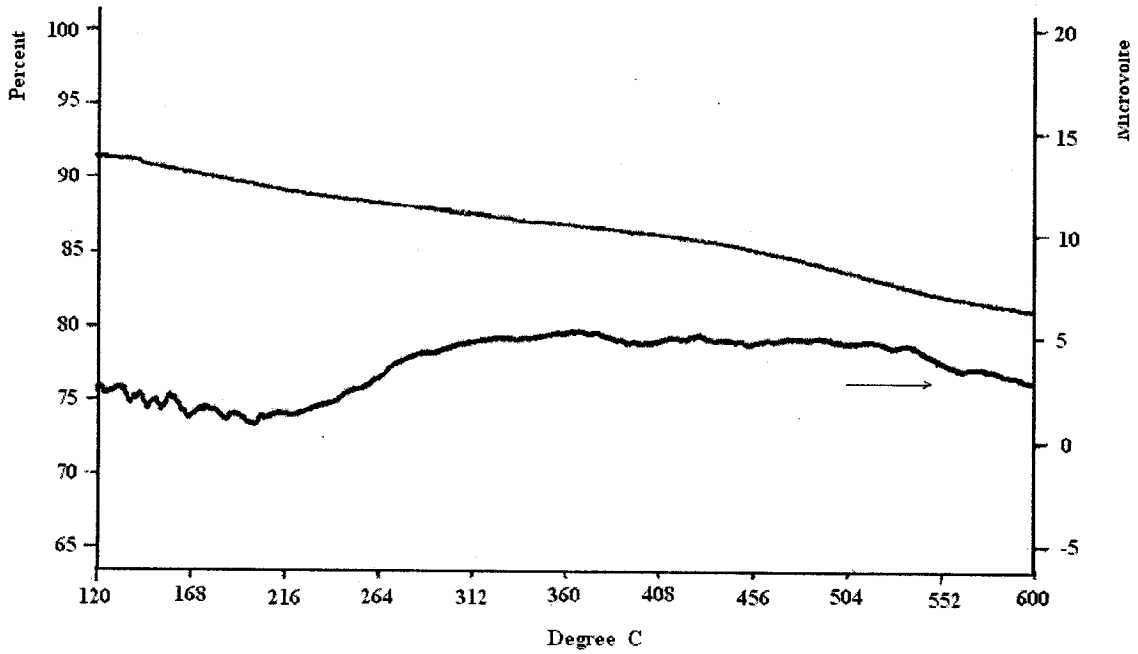

Figure 4.23 DTA / TGA analyses of (m)H-dealX incorporated with 20wt% sulfuric acid in argon with flow rate: $4cm^3min^{-1}$.

TFA

$$CF_3SO_3H + H_2O \rightleftharpoons CF_3SO_3^- + H_3O^+$$

deposition

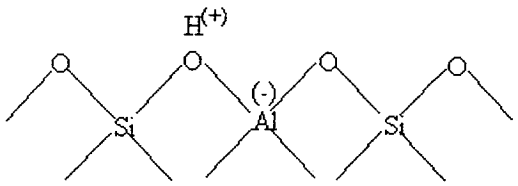

Form I acidic (protonic form)

Zeolite surface

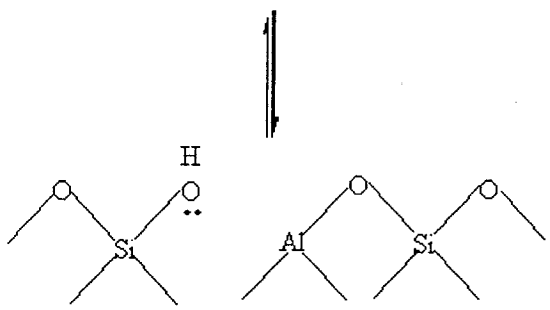

Form II acidic (silanol)

Next page

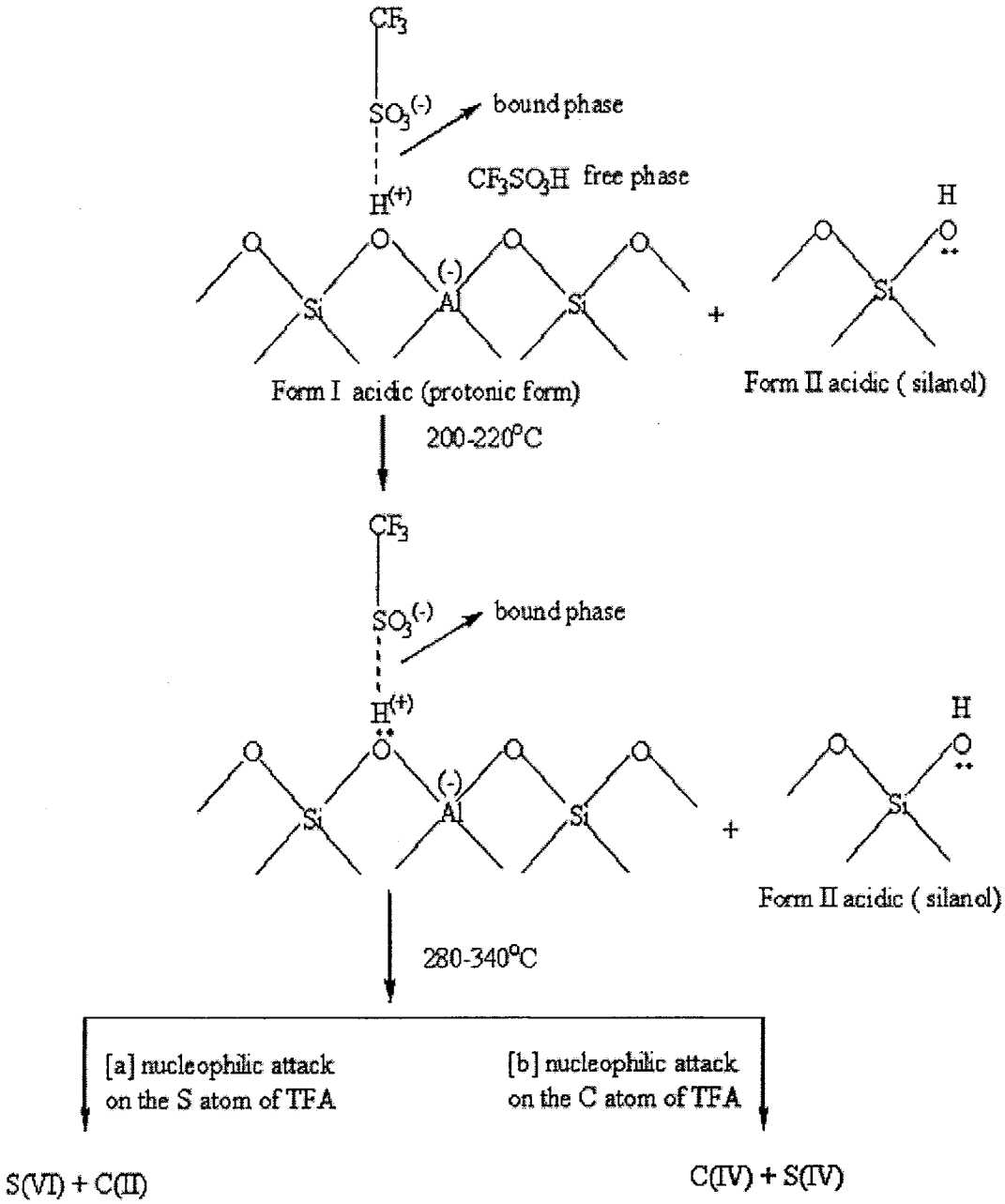

Figure 4.24 illustration of free and bound phase of TFA changes supported on (m)H-dealX material upon thermal treatment

4.6 Modification of the pore characteristics

We are interested in the preparation of host materials suitable for accommodation of a homogenous catalyst. In order to encapsulate a large amount of liquid, the solid supports need to have a large pore volume as well as a small pore aperture. From previous work in our lab, when orthosilicate species were incorporated into the ZSM-5 zeolite, which was subsequently activated at high temperature, the pore opening could be reduced from an average of 0.55nm to 0.47nm [21]. When this method was applied to our materials, particularly the (m)H-dealX, significant decrease in the pore opening was found. Unfortunately, the average pore diameter is also affected to almost the same extent. A maximum pore opening narrowing (from 3.9nm for the (m)H-dealX sample to 3.7nm for the (20)(m)H-dealX sample) is observed with an incorporation of 20wt% of orthosilicate as shown in Table 4.12 and Figure 4.25. As the deposited amount of orthosilicate exceeds 20wt%, both the specific surface area and pore volume decrease with the increase in the amount of orthosilicate. This is probably caused by the migration and further agglomeration of SiO_4 in excess in the mesopores. Most important, by the incorporation of orthosilicate reinforces the walls of the silica nanoboxes and increases the number of hydroxyl groups that can be useful in various other procedures for grafting of active functions.

Table 4.12 Modification of the pore characteristics upon incorporation of orthosilicate (and subsequent thermal treatment)

Sample	SiO_4 wt%	S_{BET} $m^2 g^{-1}$	D_{av} nm	D^{op} nm	V_t $cm^3 g^{-1}$	V_{mes} $cm^3 g^{-1}$	V_{mic} $cm^3 g^{-1}$	V_{mac} $cm^3 g^{-1}$
(0) (m)H-deal X	0	328	4.46	3.88	0.43	0.40	0.00	0.03
(5) (m)H-deal X	5	324	4.45	3.87	0.42	0.39	0.00	0.03
(10) (m)H-deal X	10	343	4.40	3.85	0.44	0.40	0.00	0.04
(15) (m)H-deal X	15	348	4.39	3.77	0.43	0.39	0.00	0.04
(20) (m)H-deal X	20	347	4.37	3.70	0.42	0.38	0.00	0.04
(25) (m)H-deal X	25	345	4.29	3.85	0.41	0.37	0.00	0.04
(40) (m)H-deal X	40	331	4.22	3.83	0.38	0.34	0.00	0.04

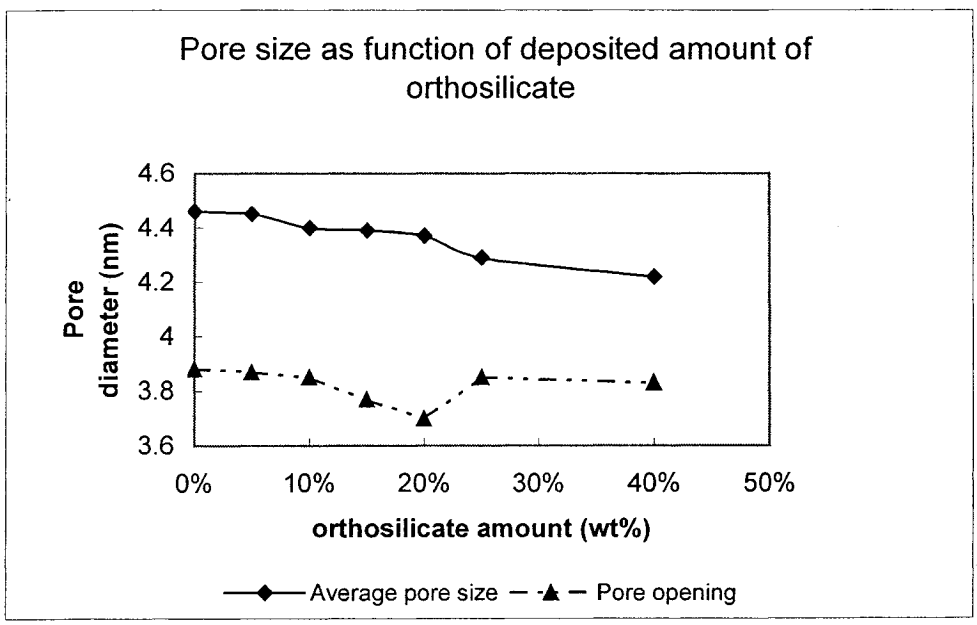

Figure 4.25 Profile of average pore size and pore opening diameter as function of deposited amount of orthosilicate

4.7 Mesoporous material MCM-41 (pure silica)

Hydrothermal synthesis of MCM-41 (pure silica) from surfactant MTMA cations in our lab is listed on table 4.13 as sample 1. It is believed that pure silica form of MCM-41 should have higher thermal and hydrothermal stability than that of aluminosilicate. Some properties of the MCM-41 material concerning thermal, hydrothermal (immersed in 5wt% NH_4Cl aqueous solution at 80°C) and chemical stability (incorporated with 16wt% of TFA) are tested and the results are also reported in table 4.13.

Table 4.13 Templated synthesis of pure-silica MCM-41 and its thermal, hydrothermal and chemical stability

Sample No.	S_{BET} $m^2 g^{-1}$	S_{cum} $m^2 g^{-1}$	S_{mic} $m^2 g^{-1}$	D_{av} nm	V_t $cm^3 g^{-1}$	V_{mes} $cm^3 g^{-1}$	V_{mic} $cm^3 g^{-1}$	V_{mac} $cm^3 g^{-1}$
1	1027	1380	0	2.7	0.94	0.76	0.00	0.18
2	178	174	6	3.8	0.15	0.15	0.00	0.00
3	667	566	53	4.5	0.62	0.59	0.03	0.00
4	370	259	42	3.6	0.26	0.21	0.02	0.03

1-pure-silica MCM-41
2-pure-silica MCM-41 was activated by TPC (A method)
3-pure-silica MCM-41 in 5wt% NH_4Cl aqueous solution at 80°C (same procedure as ion-exchange for Na-dealX)
4-pure-silica MCM-41 incorporated with 16wt% triflic acid by wet impregnation technique

From the results in Table 4.13, we can conclude that:

a) Pure-silica MCM-41 is typically mesoporous material with high specific surface area (>1000$m^2 g^{-1}$) and large sorption volume (total volume > 0.9$cm^3 g^{-1}$). However, its nitrogen adsorption and desorption isotherm plot as shown in Figure 4.26 indicates that the mesopores in MCM-41 are not of perfectly cylindrical shape.

b) Pure-silica MCM-41 has low thermal stability compared to (m)H-dealX at 700°C in Table 4.7. At first, one had hoped that MCM-41 based catalysts would crack heavier crude oil based on its large pores. However, sample No.2 indicates that the mesoporous framework of MCM-41 completely collapsed upon calcination at 700°C, a commonly used temperature in the catalytic cracking process.

c) Lower hydrothermal stability of pure-silica MCM-41 can be confirmed from sample No.3 result. Even in the aqueous solution of 80°C, a collapse of the structure framework in sample No.3 is clearly indicated by a decrease (nearly half) in the BET surface area and a decrease in the sorption volume by $0.3cm^3\ g^{-1}$, along with the formation of some micropores. The structural collapse would be much more severe in the presence of the steam at high temperature.

d) Pure-silica MCM-41 is chemically nonresistant. The BET surface area and sorption volume have been found to decrease by 64% and 72%, respectively after the pure silica MCM-41 was loaded with 16wt% TFA (sample No.4).

The differences in properties between the (m)H-dealX material and pure-silica MCM-41 probably originate from their pore structures. In fact, the pore walls of MCM-41 are merely a stack of silica layers, which are less solid than those in (m)H-dealX which are similar to that of the walls of siliceous zeolites. Therefore, MCM-41 has limited their applications, instead, (m)H-dealX material will reveal a splendid prospect in the field of petrochemical industry .

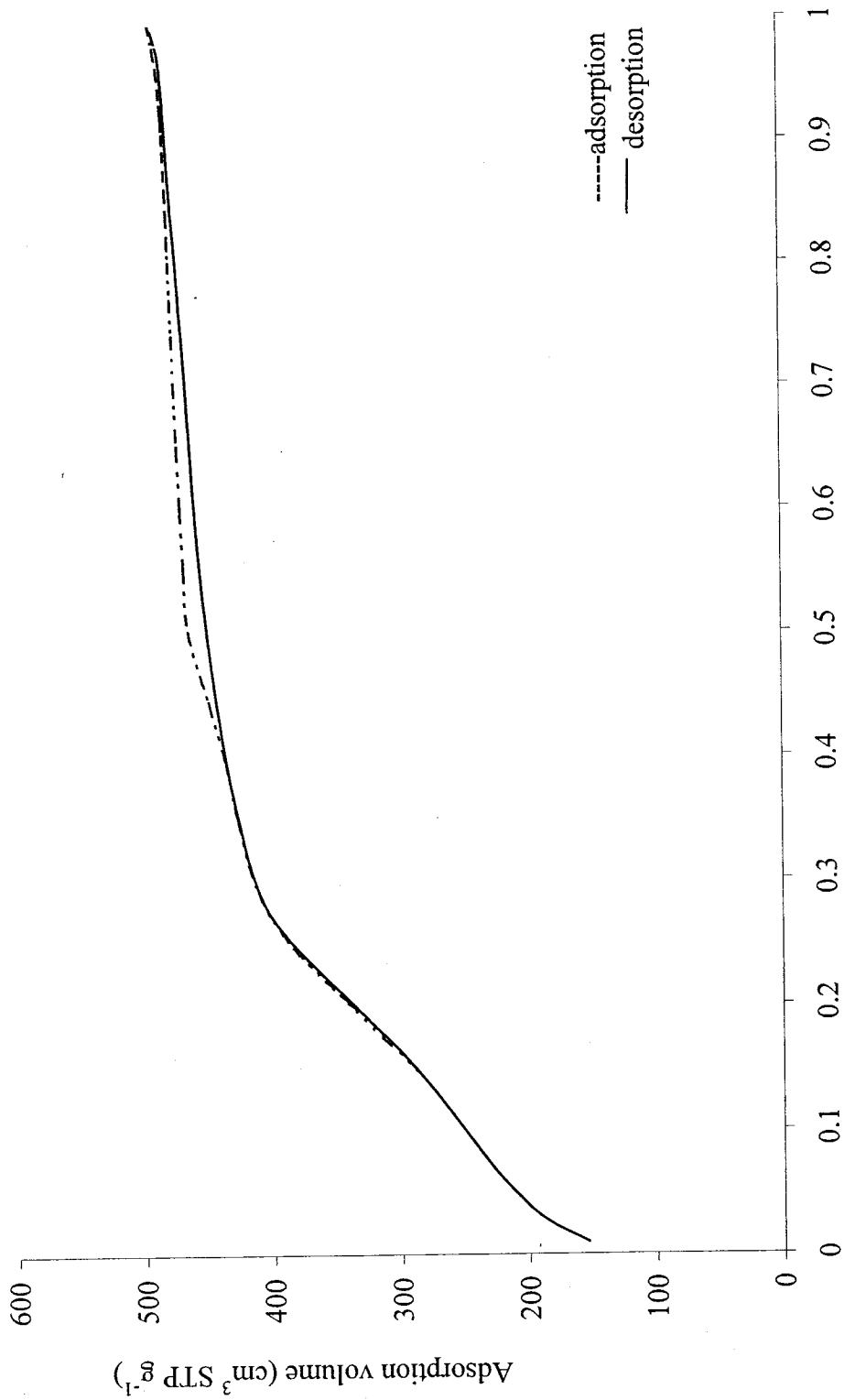

Figure 4.26 Nitrogen adsorption and desorption isotherms plot of pure silica MCM-41

Chapter 5

Conclusions

In recent years, several nanomaterials expected to have interesting applications in catalysis, separation technology and chemical sensing have been synthesized [10-11, 41-44]. In particular, in some catalytic applications, strong surface acidity and high thermal stability are essential [42, 43]. To accommodate for the need of such a material, we report the production of a new thermally (using the TPC procedures of calcination) and chemically stable nanomaterials having periodic arrangement of interconnecting mesopores. This material, which is called silica nanoboxes, is found to have better thermal and chemical stability properties than the mesoporous MCM-41. These silica nanoboxes which are prepared by a controlled dealumination of alumina-rich zeolites, show pore characteristics which depend on the parent zeolites: the alumina-richer the zeolite, the narrower the mesopores of the resulting nanoboxes. Silica nanoboxes, (m)Na-dealX, have BET surface area of 435 $m^2 g^{-1}$, average pore diameter around 4.6nm and a single pore size distribution, d_{av} = 4.6 ± 1.0 nm. On the other hand, the pore characteristics of the deal-CaA are: BET surface area of about 250m^2g^{-1}, pore size diameter of around 15.0nm, and quite broad pore distribution, d_{av} = 15.1 ± 3.0 nm. The dissimilarities are due to the difference in the Si/Al atom ratio: 1.2 for NaX and 1.0 for CaA. The optimum conditions for dealuminating 2.7g of NaX and 5.0g of CaA are: injection of 20cm^3 of 0.5$moldm^{-3}$ AHFS at the rate of 0.81cm^3min^{-1} and 1.7cm^3 min^{-1}, respectively; reaction temperature at 80°C under mild stirring. Finally the solids were

completely washed in the vacuum filtration with distillated water. The Si/Al ratios in (m)Na-dealX and deal-CaA are 3.2 and 1.7 using an AAS technique, respectively.

Only, dealuminated NaX showing only mesopores are thermally very stable. Temperature-programmed calcination of (m)NH_4-dealX resulted in silica nanoboxes exhibiting an ink-bottle shape with a quite high surface area (330 m^2/g, no micropores), an average pore diameter of 4.5 nm with a quite narrow pore size distribution (+/- 1.0 nm), and finally, a pore opening diameter of 3.9 nm. The latter was determined by using the nitrogen sorption isotherms (BET technique) and related textural data. The sorption behavior also suggested the interconnecting character of the newly created nanoboxes. The periodicity of these nanoboxes throughout the mesoporous material was clearly shown by X-ray powder diffraction at very small angles. The Si/Al ratio in (m)H-dealX is about 3.9 by AAS.

Incorporation of orthosilicate into the obtained mesoporous materials using the recently developed technique for pore size engineering in zeolites, led to materials with smaller pore openings (the smallest pore mouth of 3.7nm occurred at the incorporation of 20wt% of orthosilicate), with almost the same textural properties as the original mesoporous material.

Solid superacidic materials were prepared by incorporating a liquid superacid (triflic acid or trifluoromethanesulfonic acid) into the silica nanoboxes using wet impregnation technique. The maximum triflic acid loading, which did not significantly affect the mesoporous framework of the materials, was 24wt%. As reference, the maximum loading of a less acidic sulfuric acid was slightly lower (almost 20wt%). All these indicate a high chemical stability for the silica nanoboxes in supporting very acidic

species. Temperature-programmed desorption using a combined DTA/TGA system allowed the assessment of the amounts of the acidic species corresponding to the liquid acid (4wt%) and to the acid-bound phases (15wt%).

Prospects for applications of the new silica nanoboxes are particularly brilliant in Catalysis (encapsulation of "liquid" acidic species and ionic liquids, the latter might be used as a media for organic synthesis [66]) and in Separation technology (for instance, separation of peptides by gel-filtration chromatography or by ultrafiltration using pinhole-free membrane or filters prepared by special technique [67]). Especially in Catalysis, a solid superacid is most advantageous in acid catalyzed reaction, such as Friedel-crafts acylation because of its high acidity. Furthermore, the conventional catalyst for this reaction is Lewis acid such as $AlCl_3$, which forms a stoichiometric complex with the product (important intermediates for the production fine chemicals, such as pharmaceutical, cosmetic). To obtain the pure product, the decomposition of this complex is generally washed with water several steps followed by distillation. However, a solid superacid as a catalyst does not need any solvent and thus can simplify the industrial processes to at least one [68].

References

[1] K.S.W. Sing, D.H. Everett, R.A.W. Haul, L. Moscou, R.A. Pierotti, J. Rouquerol, T. Siemienewska, *Pure Appl. Chem.* **57**, (1985), 603.

[2] M.E. Davis, C. Saldarriaga, C. Montes, J.M. Garcés, C.E. Crowder, *Nature*, **331**, (1988), 698.

[3] R.M. Dessau, J.L. Schlenker, J.B. Higgins, *Zeolites*, **10**, (1990), 522

[4] R. Szostak, R. Kuvadia, J. Brown, T.L. Thomas, *Zeolites: Facts, Figures, Future, Proceedings 8th International Zeolite Conference, Studies in Surface Science and Catalysis*, Vol.**49**, Jacobs and Van Santen, eds., Elsevier, Amsterdam, 1989, 439.

[5] M. Estermann, L.B. McCusker, C. Baerlocher, A. Merrouche, H. Kessler, *Nature*, **352**, (1991), 320-323.

[6] Q. Huo, R. Xu, S. Li, Z. Ma, J.M. Thomas, R.H. Jones, A.M. Chippendale, *J. Chem. Soc. Chem. Commun.*, (1992), 875.

[7] C.C. Freyhardt, M. Tsapatsis, R.F. Lobo, K.J. Balkus, Jr., M.E. Davis, *Nature*, **381**, (1996), 295.

[8] P. Wagner, M. Yoshikawa, M. Lovallo, K. Tsuji, M. Tsapatsis, and M.E. Davis, *J. Chem. Soc., Chem. Commun.* (1997), 2179.

[9] J.S. Beck, C.T. Chu, I.D. Johnson, C.T. Kresge, M.E. Leonowicz, W.J. Roth, J.C. Vartuli, Int. Pat. Appl. WO 91/11390, August 8, 1991.

[10] C.T. Kresge, M.E. Leonowicz, W.J. Roth, J.C. Vartuli, J.S. Beck, *Nature*, **359,** (1992), 710.

[11] J.S. Beck, J.C. Vartuli, W.J. Roth, M.E. Leonowicz, C.T. Kresge, K.D. Schmitt, C.T.-W. Chu, D.H. Olson, E.W. Sheppard, S.B. McCullen, J.B. Higgins, J.L. Schlenker, *J. Am. Chem. Soc.* **114**, (1992), 10834.

[12] P.T. Tanev, M. Chibwe, and T.J. Pinnavaia, *Nature*, **368**, (1994), 321.

[13] G.K. Chuah, X. Hu, P. Zhan, S. Jaenicke, *Journal of Molecular Catalysis A: Chemical,* **181**, (2002), 25.

[14] J. Weitkamp, *Catalysis and Zeolites Fundamentals and Applications*, Eds. L. Puppe, © Springer- Verlag Berlin Heidelberg 1999. a) 330; b) 152; c) 251.

[15] R. Le Van Mao, N.T.C. Vo, B. Sjiariel, L.Lee, G. Denes, *J. Mater. Chem.*, **2** (6), (1992), 595.

[16] R. Le Van Mao, N.T.C. Vo, G. Denes, T.S. Le, *J. Porous Mater.*, **1**, (1995), 175.

[17] R. Le Van Mao, J.A. Lavigne, B. Sjiariel, C.H. Langford, *J. Mater. Chem.*, **3** (6), (1993), 679.

[18] R. Le Van Mao, G. Denes, N.T.C. Vo, J.A. Lavigne, S.T. Le, *Mat. Res. Soc. Symp. Proc.*, **371**, (1995), 123.

[19] C. Marcilly, in *Catalyse acido-basique : Application au raffinage et la pétrochimie*, Vol. **2**(ed.), Technip, Paris, 2003, 720 and reference therein.

[20] A.H. Janssen, A.J. Koster, K.P. de Jong, *Angew. Chem. Int. Ed.*, **40** (6), 2001, 1102.

[21] D. Ohayon, R. Le Van Mao, D. Ciaravino, H. Hazel, A. Cochennec, N. Rolland, *Applied Catalysis, A*: General **217**, (2001), 241.

[22] S. Brunauer, P. H. Emmett and E. Teller, *J. Am. Chem. Soc.*, **60**, (1938), 309.

[23] G. Leofanti, M. Padovan, G. Tozzola, B. Venturelli, *Catalysis Today*, **41**, (1998), 207.
[24] Brunauer, S., Deming, L. S., Deming, W. S., Teller, E.: *J. Am. Chem. Soc.* **62**, (1940), 1723.
[25] A.J. Lecloux, in: *Catalysis Science and Technology*, ed. by J.R. Anderson and M. Boudart, Spring-Verlag, Berlin, Vol.**2**, 1981, 171.
[26] J. Fripiat, J. Chausson and A. Jelli, in : *Chimie-Physique des Phénomènes de Surface*, Masson et Cie, Paris, 1971, 26.
[27] a) J. H. de Boer, The shape of capillaries. In: *The Structure and Properties of Porous Materials*. ed. D.H. Everett, and F.S. Stone, Butterworths, London: 1958, 68-94; b) J.H. de Boer, ibidem, 88.
[28] Ch. Baerlocher, W.M. Meier, D.H. Olson, In: *Atlas of Zeolite Framework Types (Fifth Revised Edition)*, Elsevier ScienceB.V., Amsterdam, the Netherlands, 2001, 297-302.
[29] a) W.F. Hölderich and H. Van Bekkum, 822; b) Appendix 1029; c) G. Engelhardt 405; d) Eelco T.C. Vogt et al., 1004, In: *Introduction to Zeolite Science and Practice*: H. van Bekkum, E.M. Flanigen, P.A. Jacobs and J.C. Jansen (Editors), Elsevier Science B.V., Amsterdam, The Netherlands, 2001
[30] R. M. Barrer, M. B. Makki, *Canadian Journal Chemistry*, **42**, (1964), 1481.
[31] R.M. Barrer, R. Papadopoulos and L.V.C. Rees, *J. Inorg. Nucl. Chem.*, **29**, (1967), 2047.
[32] P.Fletcher and R.P. Townsend, *Zeolites*, **3**, (1983), 129.
[33] B.K.G. Theng, *New Zealand Journal of Science* **14**, (1971), 1026.
[34] S.M. Csicsery, *Zeolites*, **4**, (1984), 202.
[35] Masakazu Anpo, Eds. *Photofunctional Zeolites: Synthesis, Characterization, Photocatalytic Reactions, Light Harvesting*, Nova Science Publishers, Huntington, New York, 2000, 7.
[36] Q. Huo, D.I. Margolese, G.D. Stucky, *Chem. Mater.* **8**, (1996), 1147.
[37] J.L. Blin, C. Otjaques, G. Herrier, and B.L. Su, *Langmuir,* **16**, (2000), 4229.
[38] C.F. Cheng, W. Zhou, D.H. Park, J. Klinowski, M. Hargreaves, L.F. Gladden, *J. Chem. Soc., Faraday Trans.* **93**, (1997), 359.
[39] J. Israelachvili, D. J. Mitchell, B. W. J. Ninham, *J. Chem. Soc., Faraday Trans.* 2, (1976), 72, 1525.
[40] R. Nagarajan, *Langmuir,* **18**, (2002), 31-38.
[41] Y. Liu, W. Zhang, T.J. Pinnavaia, *J. Am. Chem. Soc.* **122**, (2000), 8791.
[42] Y. Liu, Y.J. Pinnavaia, *J. Mater. Chem.,* **12**, (2002), 3179.
[43] T-O. Do, S. Kaliaguine, *Angew.Chem. Int. Ed.*, **40** (17), (2001), 3248, and references therein.
[44] T-O. Do, A. Nossov, M-A Springuel-Huet, C. Schneider, J.L. Bretherton, C.A. Fyfe, S. Kaliaguine, *J. Am. Chem. Soc.,* **126**, (2004), 14324.
[45] P. Kletnieks, *Alkylation of Isobutane with Light Olefins Using Mesoporous Superacidic Catalysis,* M. Sc Thesis, Concordia University, Montreal, Canada, 2002, 52.
[46] P. J. Stang, M.R. White, *Aldrichimica Acta*, **16** (1), (1983),15.
[47] R. Le Van Mao, S.T. Le, in: *Handbook of MTBE and other Gasoline oxygenates*, ed. By H. Hamind and M.A. Ali, Marcel Dekker, New York, 2004, 93-100.

[48] L. Fabes and T. Wilson Swaddle, *Canadian Journal of Chemistry*, **53** (20), (1975), 3053.

[49] R.Le Van Mao and L. Huang, in: *Novel Production Methods for Ethylene, Light Hydrocarbons, and Aramotics,* eds. L.F. Albright, B.L. Crynes and S. Nowak, Marcel Dekker, New York, 1992, 425.

[50] R. Le Van Mao and L. Dufresne, *Applied Catalysis*, **17**, (1989), 141.

[51] PERKIN ELMER, *Analytical Methods for Atomic Adsorption Spectrometry* (Part no. 0303-0152).

[52] J. Rocha, S.W. Carr, J. Klinowski, *Chem. Physics. Lett.*, **187**,(1991), 401.

[53] G.W. Skeel, D.W. Breck, Proc. 6th Int. Zeolite Conf., Reno (U.S.A.), ed. D. Olson and A. Bisio, Butterworths, Guilford, 1984, 87.

[54] Ngoc Truc-Chi Vo, *Preparation and Characterization of Mesoporous Aluminosilicates from CaA zeolite*, M. Sc thesis, Concordia University, Montreal, Quebec, Canada, 1992, 134.

[55] D.W. Breck, in *Zeolite Molecular Sieves*, J. Wiley & Sons, New York, 1974, 495

[56] J.B. Uytterhoeven, L.C. Christner, W.K. Hall, *Phys Chem* **69**, (1965), 2117.

[57] R.B. Borade and A. Clearfied, *Catal. Lett.* **31**, (1995), 267.

[58] M. Suzuki, in: *Adsorption Engineering*, Kodansha-Elsevier, Tokyo, 1990, 26.

[59] Felix Kollmer, Heike Hausmann, Wolfgang F. Hoelderich, *Journal of Catalysis* **227**, (2004), 408.

[60] G.Engelhardt, U. Lohse, E.Lippmaa, M.Tarmak, and M.Mägi, *Z.anorg.allg.Chem.* **482**, (1981), 49.

[61] Qun Zhao, Chemistry and Biochemistry Department, Concordia University, unpublished.

[62] J.A. Rabo and G.J. Gajda, *Catal. Rev. - Sci. Eng.* **31**(4), (1990), 385.

[63] J.F. Joly, in: *Conversion Processes*, Vol.**3**, P. Leprince (ed.), Editions Technip, Paris, 2001, 287-288.

[64] R. Le Van Mao, T.S. Le, in: *Handbook of MTBE and other Gasoline Oxygenates*, eds. H. Hamid and M.A. Ali, Marcel Dekker, New York, 2004, 93.

[65] G.A. Olah, G.K. Sueya Prakash, J. Sommer, in: *Superacids*, J.Wiley & Sons, New York, 1985, 36-37.

[66] C&EN, (Nov.8, 2004), 44.

[67] R. Le Van Mao, E. Rutinduka, C. Detellier, P. Gougay, V. Hascoet, S. Tavakoliyan, S.V. Hoa, T. Matsuura, *J. Mater. Chem.*, 9(3), (1999), 783.

[68] R.A. Sheldon, H. Van Bekkum, *Fine Chemicals through Heterogeneous Catalysis*, Weinheim ; New York : Wiley-VCH, 2001, 170.

[69] Abdualhafed Ali M. Mutasar, *Preparation, Characterization and Properties of Novel Mataerials in the $BaCl_2/SnF_2$ System*, Ph. D thesis, Concordia University, Montreal, Canada, 2002, 31.

Appendix A: XRD equipment used

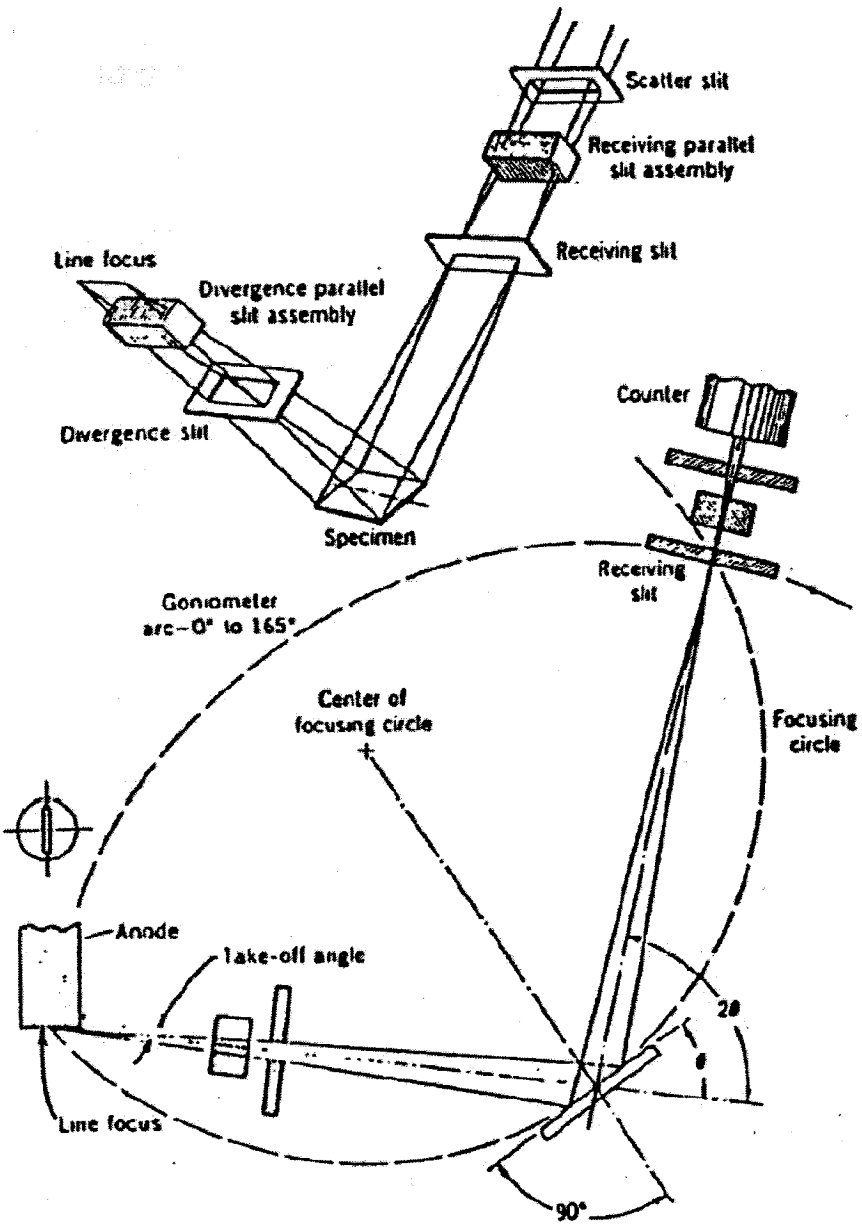

Figure A.1 A schematic arrangement of the line focusing X-ray powder diffractometer [69]

Appendix B: BET equipment used

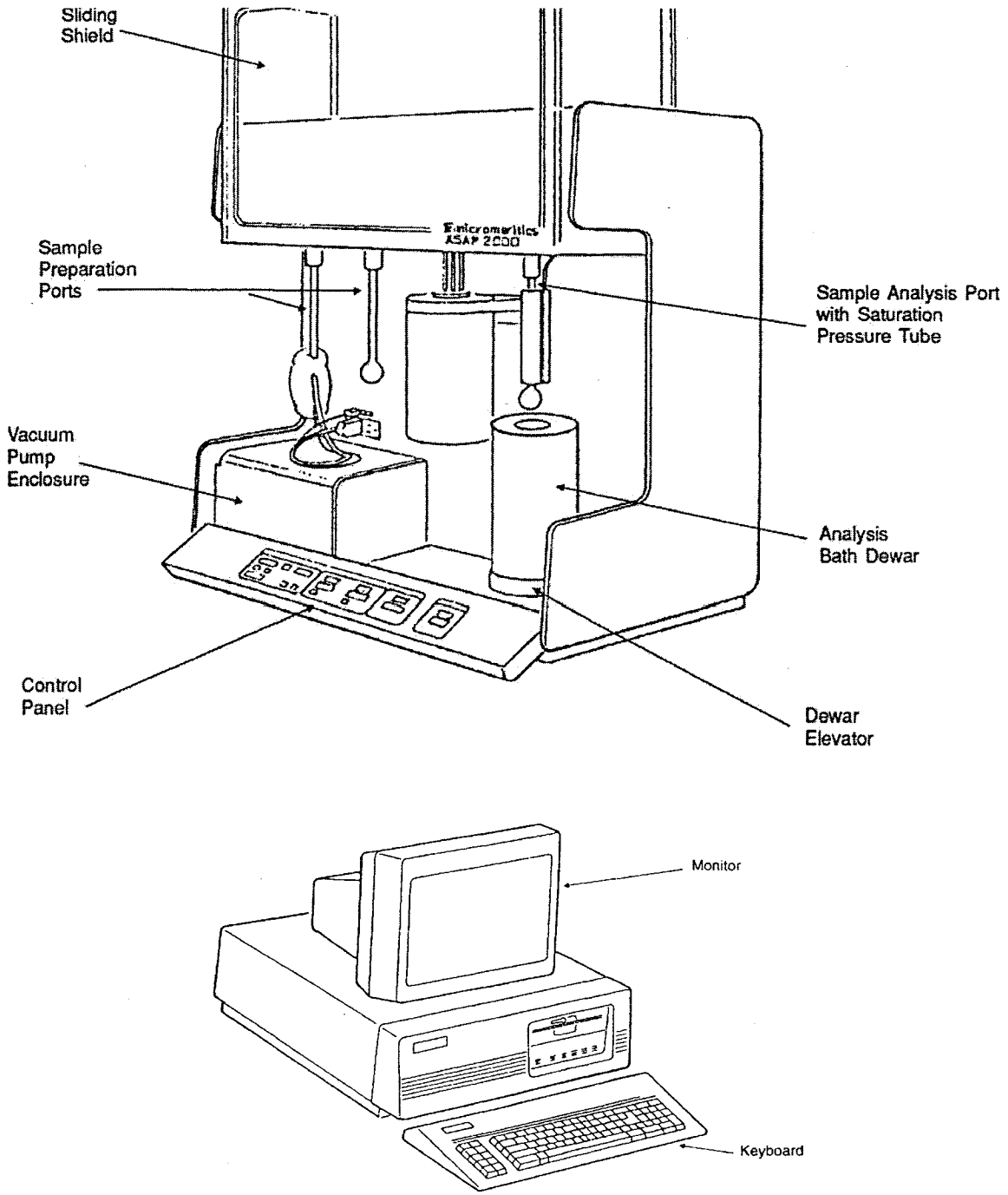

Figure B.1 ASAP 2000 System and Control Module

Appendix C: DTA/TGA equipment used

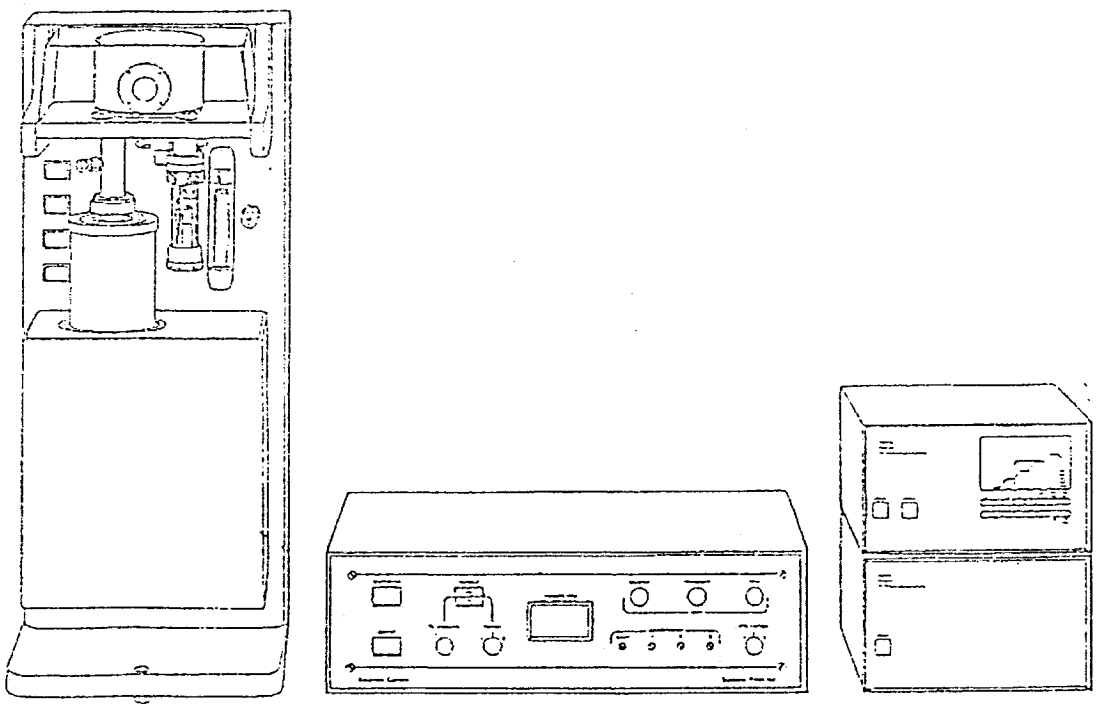

Figure C.1 STA 1000/1500 DTA/TGA instrument

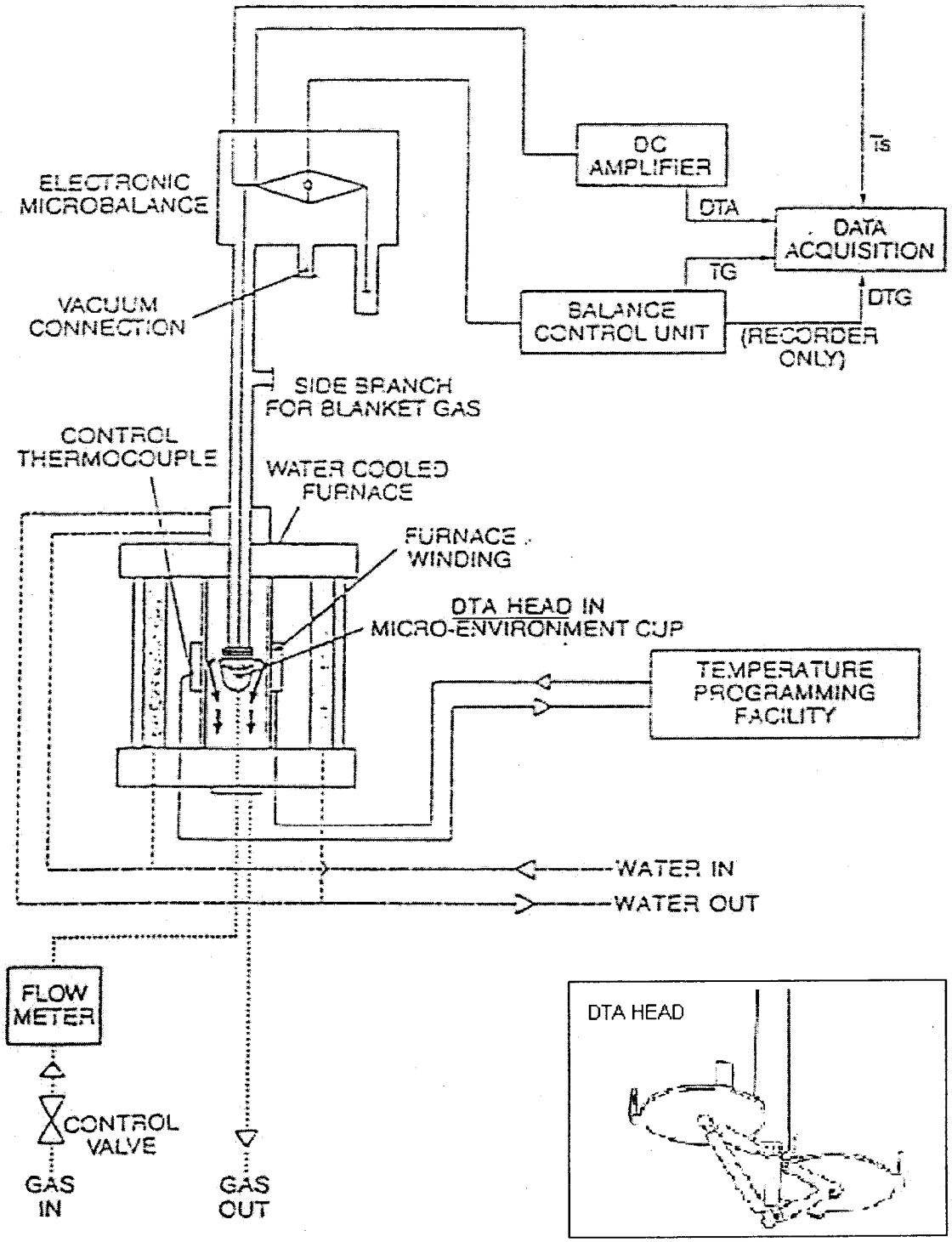

Figure C.2 STA 1000/1500 and DTA head– Schematic diagram

Appendix D: AAS equipment used

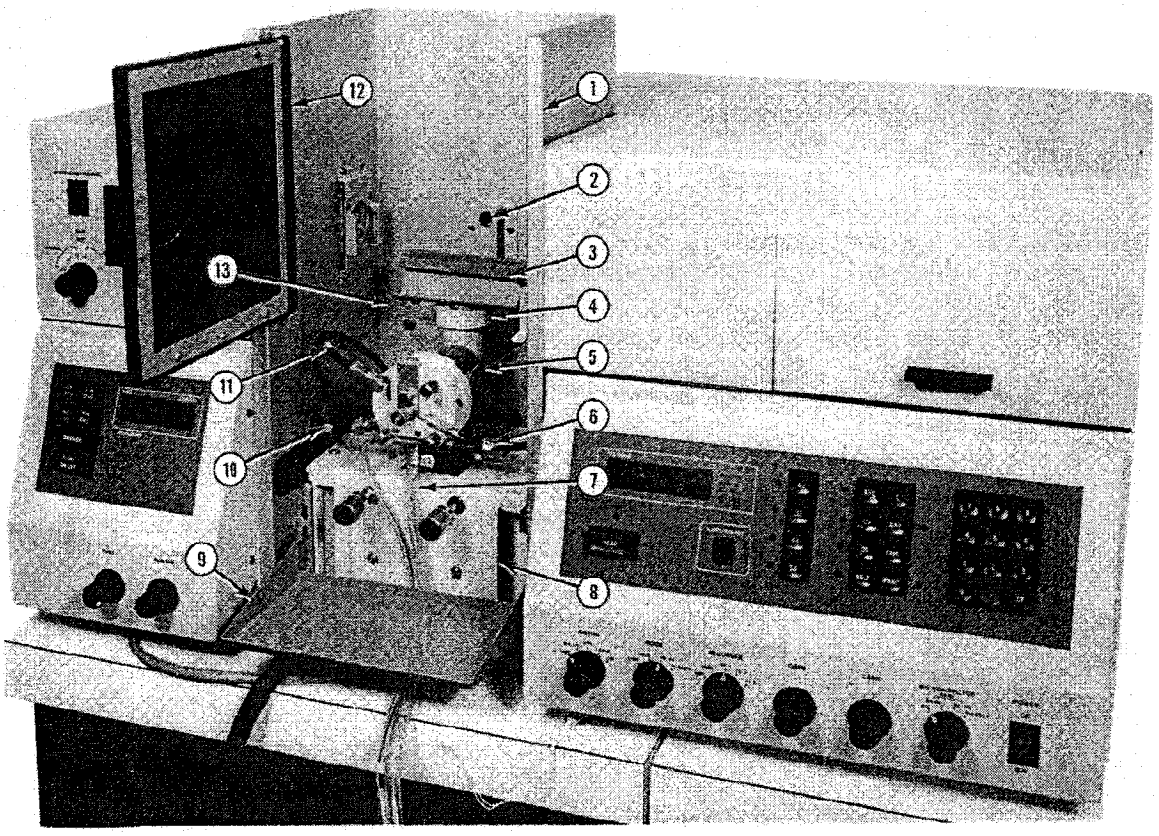

Figure D.1 A Perkin-Elmer model 2380 Instrument

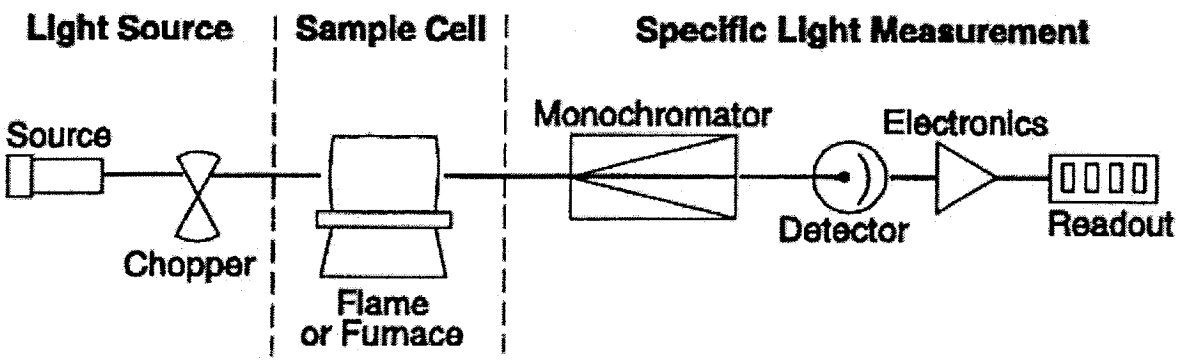

Figure D.2 Single-beam atomic absorption spectrometer